FEASIBILITY AND PARAMETRIC DESIGN STUDY OF THE APPLICATION OF A STATION-KEEPING SYSTEM TO PASSIVE COMMUNICATIONS SATELLITES

Phase IV - Final Report

January 1965

A Report Prepared Under Contract NAs 1-3131

for

THE NATIONAL AERONAUTICS AND SPACE ADMINISTRATION

by

WESTINGHOUSE DEFENSE AND SPACE CENTER
Aerospace Division
Baltimore, Maryland

1779C

FEASIBILITY AND PARAMETRIC DESIGN STUDY OF THE APPLICATION OF A STATION-KEEPING SYSTEM TO PASSIVE COMMUNICATIONS SATELLITES

Phase IV - Final Report

January 1965

A Report Prepared Under Contract NAs 1-3131

for

THE NATIONAL AERONAUTICS AND SPACE ADMINISTRATION

by

WESTINGHOUSE DEFENSE AND SPACE CENTER
Aerospace Division
Baltimore, Maryland

TABLE OF CONTENTS

LIST OF APPENDIXES

LIST OF ILLUSTRATIONS

1. INTRODUCTION

This report covers the fourth phase of a study to determine the feasibility of exploiting solar energy to provide a means of station-keeping or orbit position control to passive communications satellites.

Station-keeping or orbit position control by solar energy can be accomplished either by exploiting the direct solar pressure force of momentum transfer from the solar photon flux or by unsymmetrical reradiation of absorbed solar energy.

The basic principle used in obtaining orbit position control from solar radiation is to use this available energy to add or subtract, in a controlled manner, energy from the orbiting system. This results in a change in the orbital period or, in effect, the angular rate of the satellite in orbit. Satellites with large area-to-mass ratios or those capable of attaining it with the addition of sails are adaptable to this principle.

The use of direct solar pressure is best suited for sails or thin cross-section bodies.

Exploiting reradiation from the body is better suited to three-dimensional bodies that can absorb uniform amount of energy independently of its attitude with respect to the sun.

Specifically, this phase of the subject contract covers the study of feasibility of the application of these principles to a lenticular communications reflector stabilized to the correct attitude by the gravity gradient.

In part one of this study, two techniques for obtaining orbit position control were compared, and the most promising were selected for further analysis in part two. One technique employed the concept of attaining orbit position

control by varying the projected sail area with respect to the sun line to obtain a variation in solar force over the orbit. This concept required a yaw oscillatory period about a preferred yaw orientation, so that the plane of the sail would be mostly perpendicular to the velocity vector during half of the satellite's orbit when it approaches or recedes from the sun and mostly parallel during the opposite half of the satellite's orbit. The period of oscillation required is approximately twice the orbital period, and it was felt that this motion could be obtained by inertia forces due to mass distribution. Active control would only be used for initial displacement and the changing of modes from increasing to decreasing orbital energy.

The other technique employs the concept of utilizing a sail or the satellite's body with its two surfaces having different reflecting characteristics oriented normal to the satellite's orbital velocity vector and presenting opposite sides of the sail toward the sun during the receding and approaching halves of the satellite's orbit.

In evaluating the first technique, the amplitude of oscillation and orientation was computed to provide the equivalent mobility or angular rate of change to that of a sail with its surfaces having different reflecting characteristics. The resulting angular amplitude exceeded plus and minus 45 degrees. To implement this technique by mass distribution would form a compound pendulum of the body. The period of oscillation of a compound pendulum is inherently sensitive to the amplitude at large amplitudes. Continuous active control to implement this technique would provide little or no advantage over the other and considerably complicate the attitude control problem. Therefore, part two of the study was conducted with the second technique, which represented a body essentially at rest during its period of operation in one mode.

The initial satellite configuration consisted of a lenticular gravity-gradient-stabilized satellite whose yaw orientation was controlled by a set of three mutually perpendicular magnetic torque coils. The first task consisted of

estimating the size, weight, power, and control system needed for magnetic torquing of the satellite. After selecting a coil geometry, the forces produced by such a configuration were defined in terms of coil current to provide the basis for a structural analysis of the satellite booms and rim. Previous studies of torque coil design have shown that coils and their solar cell power supply can be optimized for minimum total weight. Techniques of coil optimization were applied to determine coil and power supply requirements. Estimates of the control electronics power requirements revealed that the weight of a solar cell power supply to furnish 50 watts for 5 years in the high intensity proton zone would represent a significant portion of the total satellite weight. For this reason, the efficiencies of various array configurations were compared to determine the optimum array for a gravity gradient satellite, thus reducing the array weight. This study resulted in the use of a flat plate array for low inclination orbits and a hemispherical array for all others. Combining this efficiency data with optimum radiation protection data previously developed allowed the calculation of minimum solar cell power supply weights at 2000 nautical miles and all inclinations. The properties of radioisotope power supplies were also investigated to allow an estimate of the weight saving resulting from their use. It was found that the use of a radioisotope thermoelectric generator would substantially reduce the weight of the required power supply. However, it was decided that for this feasibility study, the weight requirements of an np silicon solar cell array would be used for a conservative estimate of power supply weight.

Initially, it was felt that mass distribution to use the inertial forces of normal satellite rotation to provide yaw positioning would require more active peak power for control than the use of a continuous active control system because the total constraining torque required to limit the pointing errors are generally an order of magnitude larger than the disturbances.

However, because of the excessive power and weight penalties just described, this was reconsidered and the torque-boom concept was developed. In this concept, the mass distribution is achieved with thin booms and tip masses attached to the top of the satellite and connected through a means of torquing them against the body. With this technique, a mode change which consists of rotating the satellite body with respect to the velocity vector around the vertical axis can be accomplished at slow rates and low power by torquing the main body against the inertial constraint of the booms. This technique requires low power and lends itself ready to the Ames-type damper coupling by an additional pair of booms.

Since the torque-boom concept of attitude control and damping appeared to minimize both system weight and complexity, a study was conducted to determine the feasibility of its mechanization. The first consideration was that of the erectable boom structure. An estimate was made of the boom lengths and minimum tip mass requirements. Using these estimates, worst case boom loadings were found. An analysis of the deflections produced by both gravity gradient forces and thermal deflections showed that these effects would not produce significant satellite pointing error. In addition to producing rod deflections, thermal bending and gravity gradient forces were found to combine to apply a torsional moment to the booms. Since a split overlapped tube is inherently weak in torsional rigidity, this thermal windup problem became the design criterion for boom selection. The results of this structural study showed that booms of a reasonable size were capable of withstanding the loads of this application with an appropriate margin of safety. Various techniques for rotating the satellite with respect to the stabilized boom structure were also considered. A torque limited drive system was considered but was rejected on the basis of bearing friction and disturbance torques which could override drive system torques. A technique of relative velocity control was shown to be extremely feasible and required less than a watt of power. The

components required for this system were investigated to determine their performance characteristics in a space environment. The results of this investigation revealed that the required components have all had previous successful space application or had been successfully tested under similar environmental conditions.

Section II covers the development of this configuration and an analysis of its performance.

2. DESCRIPTION AND PERFORMANCE ANALYSIS OF FINAL CONFIGURATIONS

Two final configurations are presented in this section with the development and the analysis of performance. The means of attitude control and stabilization are the same, but one configuration is predicated on the use of an optically transparent, but RF reflective lens material; the other an optically opaque lens material. When the transparent lens is used, sails are added to provide orbit position control; when using the opaque lens, orbit position control is achieved by applying a pattern of different surface treatments or coatings to the lens material. Dimensionally the two configurations differ slightly to provide the gravity gradient constraining torques required to resist the different solar disturbance torques produced on each body. Essentially, the differences in performance, as shown in this section, are small.

Attitude Control

The attitude control system was specified by describing the functions which it must perform and the methods which could be used to obtain the performance. There are three required functions: earth pointing, initial orientation and damping, and yaw control. By earth pointing is meant the alignment of the axis of symmetry of the lens with the center of the earth, and this must be done within a few degrees so that the surface of the lens will be an effective reflector for communication between any two stations on the earth in view of the satellite. This earth pointing or vertical stabilization is to be done by making use of the gravity gradient with the elongated structure shown in figure 2-1. This placement of mass with inflatable tetrapod booms was originated in a previous study. The purpose is to obtain differences in the principal moments of inertia such that $I_x > I_z$ and $I_y > I_z$. This is necessary to obtain gravity gradient torques in the direction necessary to obtain vertical stabilization. Because the gravity gradient torques are bistabilizing

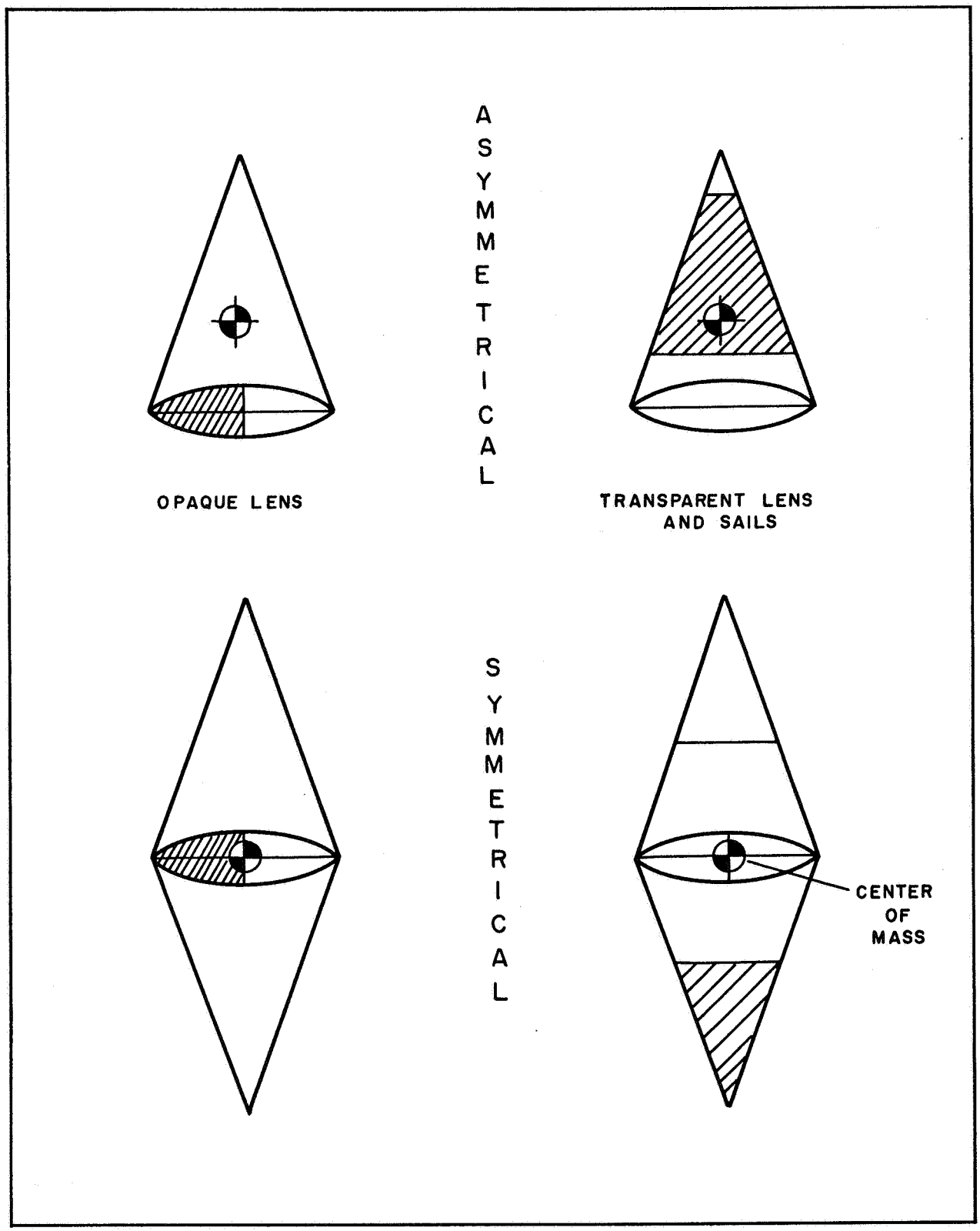

Figure 2-1. Basic Configuration

and conservative, means must be provided to ensure that the proper end of the satellite faces the earth and that librations due to initial errors and subsequent disturbances are damped to a low value in a reasonable amount of time. This is the second function of the attitude control system.

It might be possible to ensure the proper orientation of the satellite by controlling the attitude of the canister before the satellite is inflated. However, because of the complications resulting from a multiple launch and the uncertainties of the inflation process, other methods of initial orientation were considered which deal with the satellite after it is erected. To damp the satellite librations, the energy of this motion must be dissipated. Two methods of passive damping in which the satellite would be coupled to another inertial body by a dissipative device are mentioned in the contract amendment. These are the resonant spring and fluid damper proposed by Goodyear Aircraft (G.A.C.) and a rotary damper connecting the satellite and a rod of high inertia moment. In addition to these methods of passive damping, it was suggested that the active magnetic torque system being considered for yaw control might be used to produce the retarding torques necessary for damping.

The Euler angles relating orbital and satellite body coordinates are depicted in figure 2-2. Any damping method would be required to damp librations in pitch and roll, but depending on the required yaw control, damping of motion about the yaw axis might or might not be needed. This third function will be described next.

The yaw control of the satellite is necessary to obtain orbit position control impulse from solar radiation pressure. It necessarily involves active elements since the orbit position is to be controlled from the ground. Three types of yaw motion were hypothesized in order to obtain impulse from different surface configurations. A constant velocity pointing control would be necessary for a solar sail with opposite surfaces which produce different values of force when facing the sun. This constant yaw angle would also be necessary for impulse obtained by thermal reradiation from an opaque lens.

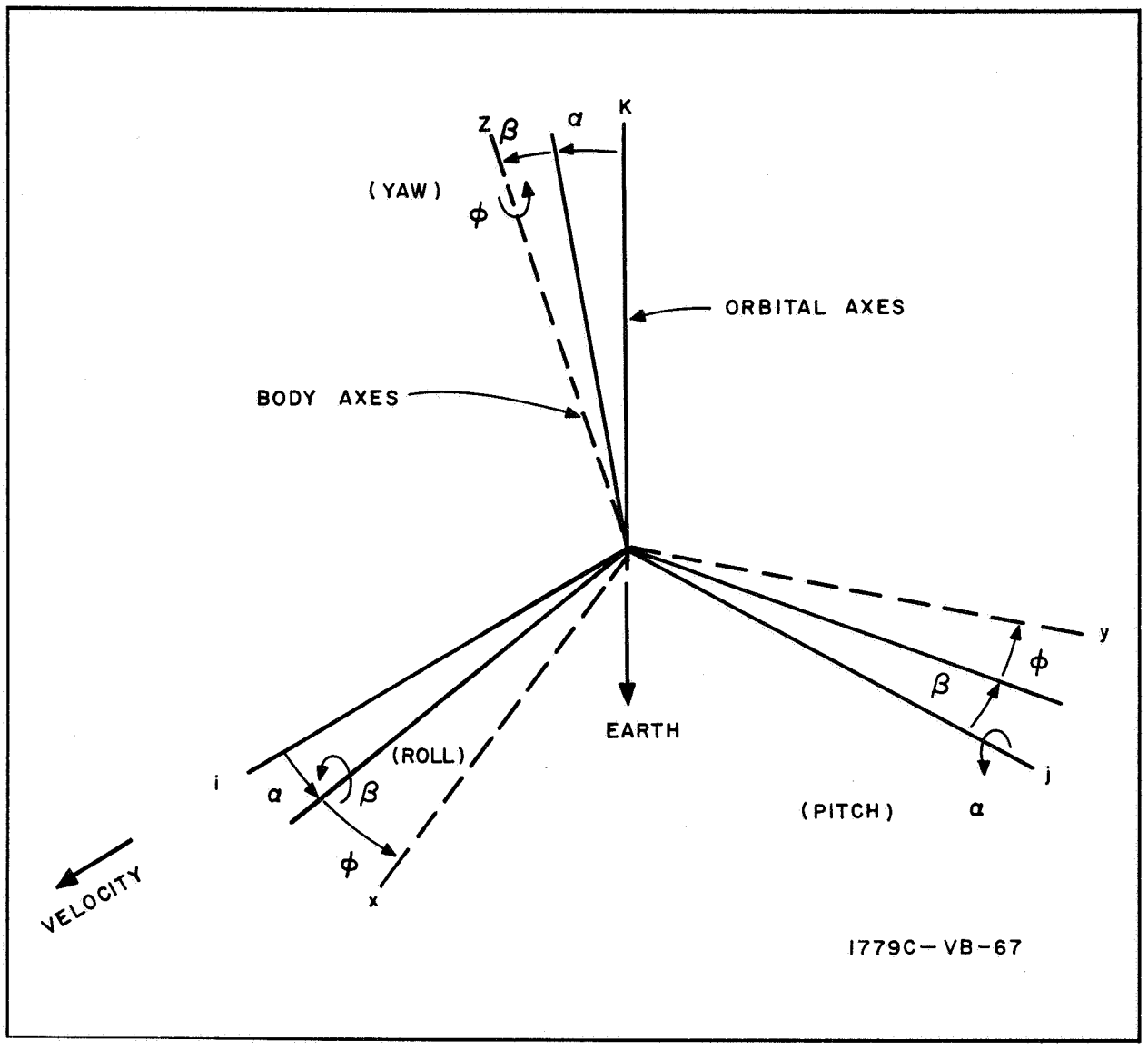

Figure 2-2. Rotation Angles Relating Body to Orbital Axes

Constant yaw stabilization can be obtained by having the satellite mass arranged such that $I_x < I_y$. The only active control needed in this case would be a rotation of the sail to change between an accelerating and decelerating force, and this could be done by forcing the satellite between the two stable yaw positions. OPC impulse could also be obtained from a sail with a single surface characteristic if the projected area to the sun is varied sinusoidally around the orbit. Two methods of yaw control have been suggested to do this.

One method requires the yaw oscillation of the sail at half the orbital frequency. The other requires a continuous yaw rotation at half the orbital rate. The yaw oscillation was suggested by the contractor because the required frequency is within the range of natural frequencies for yaw oscillation. These two yaw motions would require continuous active control to produce OPC. The active methods of yaw control considered initially were reaction wheels and magnetic torque coils, It was also suggested that the coils could be used to produce vertical controlling torques. These complete the requirements with which the study was begun.

The purpose of the preliminary survey was to examine briefly all of the applicable means of attitude control that could be thought of in order to select the most promising concepts and devices for a more thorough examination. This process was organized by considering the different aspects of the problem separately. It would have been possible to hypothesize many different satellite configurations consisting of a method of OPC, an active controller to produce the required yaw motion, and a damping device for attitude errors, and to analyze these configurations. However, it was apparent that the elements of the configurations were basically similar and could be studied with little concern about how they would be combined. For instance, a magnetic torque system would have about the same design whether used to produce a constant or varying yaw angle. The elements of the control system to be studied correspond to the functions mentioned previously. The three types of yaw motion were examined together to see if one was most desirable. The magnetic and reaction wheel active control systems were compared as they applied to the satellite with and without a passive yaw control. Libration damping methods were compared to select the preferred one. Since the structure for gravity gradient vertical stabilization was specified by the contract, this was not of concern in the survey. The comparisons which were made will be described next.

Some considerations which helped to establish a preferred type of yaw motion were the vertical error induced by the motion, the torques applied

to the structure in order to produce the motion, and whether active control would be required. A digital computer simulation was used to analyze the types of motion (Appendix XII). Because the reaction wheel and other control elements would be placed at the apex of the quadrapod, the torques they would produce were calculated because they might require a heavier structure. The weights of the control elements were estimated for comparison. The preferred configuration emerged as follows:

The constant yaw rotation was found to produce too large a vertical error unless done with a reaction wheel. The yaw oscillation would not produce too large an error, but either type of yaw motion would require continuous active control to produce OPC because the yaw motion must be synchronized with the orbital motion. The constant yaw angle, on the other hand, could be produced by the passive system formed by adding a horizontal boom to the apex of the quadrapod. The torque exerted on the quadrapod by this system would be high only during the yaw flip, in which case it would be comparable to the yaw oscillation. Thus, the constant yaw pointing was chosen as the best method of obtaining OPC insofar as the attitude control system was concerned.

The preliminary choice of a libration damper was based largely on previously made studies. In general, it would be hard to approach the reliability of a passive damper with an active system. The magnetic control system developed by Westinghouse in the previous contract has the added disadvantage for this application that it produces a fairly large limit cycle type of oscillation due to the variation of the earth's magnetic field variation around the orbit. It is an inherent feature of any damping method using the earth's magnetic field that a certain amount of oscillating disturbance torque results. Of the two types of passive dampers, the rotary damper appears to have the most advantages. According to the previous G.A.C., report, the lossy spring and fluid damper would weigh over 100 pounds,

whereas a rotary damper and rod would weigh less than 50 pounds. The rotary damper also has the advantages that it can be tested before launching and that it is effective in damping tumbling. These considerations lead to the choice of a rotary damper, and its use in an Ames-type configuration was decided upon because that configuration had been extensively studied and shown to have good three-axis damping. This is shown in figure 2-3.

When the magnetic and reaction wheel torque systems were compared, the differences were not too great. For continuous control, both would weigh about 200 pounds. Both would require the same attitude sensors and in place of part of the the electronic computing circuitry in the magnetic system, the wheel system would require a means of momentum damping, perhaps through use of gravity gradient torques. The principal difference between the two systems is that the magnetic system would produce forces along the quadrapod booms whereas the reaction wheel would produce a torque at the apex of the quadrapod. Both systems could be simplified if only a yaw flip should be required. The weight of the wheel system could be reduced to approximately 100 pounds, the lower of the two. However, even 100 pounds was considered to be an excessive weight for such a simple task. Furthermore, the relatively large torques which would be exerted by such a system would require heavier booms than would otherwise be required. For these reasons, a better means of yaw control was searched for.

Among the methods considered to reduce the yaw control system was one to suspend the solar sail within the quadrapod so that it could be controlled independently of the satellite. This idea was rejected, however, because of the resulting structural complexity. The idea finally adopted was conceived when it was observed that the only source of the passive yaw restoring torque of the system shown in figure 2-3 was the pair of horizontal rods. It was apparent that if a means could be found to rotate the rest of the satellite with respect to these rods, a simple yaw control system would result which would

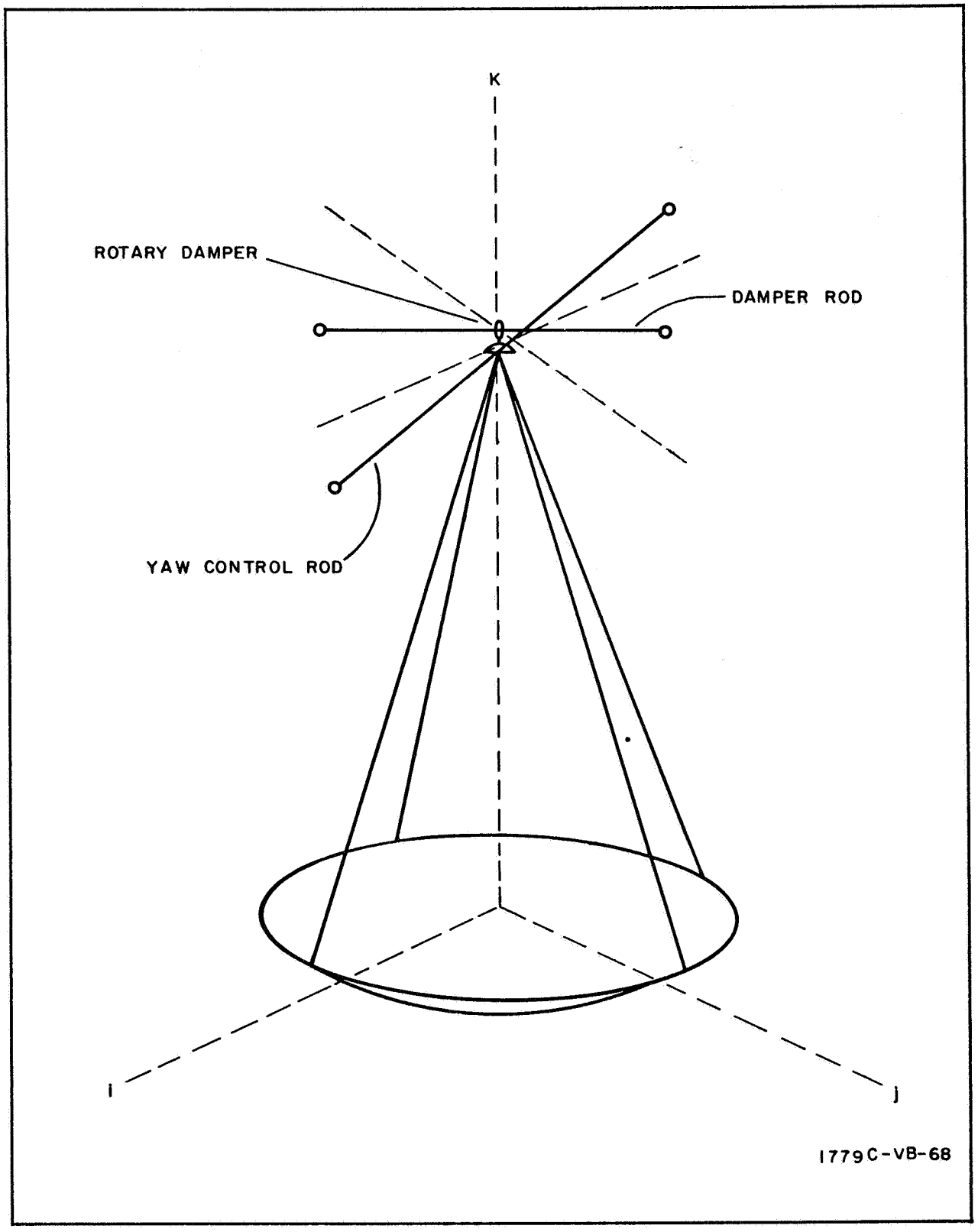

Figure 2-3. Satellite With Ames-Type Damping Configuration Shown in Equilibrium Position

exert negligible additional torque on the quadrapod booms. The rods would give a restoring torque somewhat less than 10^{-3} lb-ft per degree in yaw, and if the satellite were in perfect equilibrium, a torque of this value applied between the rods and the lens would deflect the rods slightly and accelerate the lens in the opposite direction. When the lens had completed half the required rotation, the torque could be reversed to decelerate the lens. Such devices as torque limiting springs and magnetic suspended bearings were considered for the yaw pivot in order to avoid a bearing exposed to the space environment. However, because a rigid coupling in pitch and roll was needed at all times, and because the steady-state oscillation of the satellite would result in unpredictable yaw-torques larger than the required accelerating torque, these devices were not satisfactory. Instead, a bearing designed for space application containing a dry lubricant was selected. A small motor, electronically controlled to produce a constant acceleration-deceleration rotation, would be hermetically sealed and coupled by a harmonic drive to the satellite. The whole assembly except for the command receivers would weigh only 14 pounds. The redundant receivers would be placed at the end of the yaw booms where the weight would be required in any case. This yaw control system offers the advantage of multiple yaw positioning which was found to be useful in obtaining OPC with a sail when the sun is out of the orbit plane. Thus, the system which was synthesized consists of the lens with quadrapod and rods attached in the form of the Ames gravity gradient configuration. The passive yaw control would be used to obtain OPC with changes in yaw angle made by a motor controlled pivot between the horizontal rods and quadrapod. The choice between a solar sail or an opaque lens for OPC, was not specified since no reason was found for a preference. Thus, two systems were retained for analysis of problem areas and expected performance. These were designated as symmetrical and unsymmetrical because of the location of the center of mass with respect to the lens.

The principal aspects of the two satellite configurations which were analyzed had to do with their construction and performance. Extensible rods of the type made by DeHavilland Aircraft, Ltd, were studied in order to determine the specifications necessary to obtain the necessary strength and straightness. The design of the motor yaw control was also considered in more detail. A suitable rotary damper was chosen for application on the satellites. Although the digital computer simulation of the satellite incorporated a linear (torque proportional to velocity) type damper, preliminary design calculations showed that a damper with a suitably high damping constant would weigh in excess of 30 pounds. On the other hand, a hysteresis damper operating on a different principal would provide adequate damping with a weight of only 4 pounds. This damper produces a nonlinear torque versus angle function in the form of hysteresis loops. This function was approximated in the computer program and the proper value of damper torque was chosen so that it would give as high a damping rate as possible with low steady-state errors. The simulated hysteresis damper was used in further computer analysis of satellite performance.

The performance criterion of greatest interest was the steady-state vertical pointing error. This is the deviation of the lens axis of symmetry from the earth center in both pitch and roll. For the given lens reflector, a limit of 3 degrees was set to allow unrestricted earth coverage. The two largest sources of steady-state error are orbit eccentricity and disturbance torques due to radiation pressure unbalance. The effect of eccentricity was already included in the computer program, but the disturbance torques had to be determined. To simplify the effort, the guideline was followed that if the effect of the torque was to produce errors much greater or less than the 3-degree limit, that the torque would only be roughly approximated. However, if the results were marginal, more effort would go into the calculation. Accordingly, the more detailed calculation was made for the symmetrical configuration. All simulated torques included the effect of the earth's shadow. As originally conceived the unsymmetrical configuration had

torques which were much too large because of the great displacement of the CM from the wire mesh lens. To balance the pressure on the lens, a sphere was chosen as the simplest shape to place about the quadrapod. The sphere would cancel the major part of the torque, leaving a third harmonic component due to the shape of the lens. With this small disturbance the satellite error would be acceptably low. The symmetrical satellite was found to have a fairly large torque due to the shape of the lens and to reradiation forces. It was also found to have a larger eccentricity. A computer evaluation of the disturbance torque was used in the simulation, and it was found that by adjusting the height of the quadrapod, large enough moments of inertia could be obtained to reduce the error to within limits, although consideration was given to making the lens angle included larger. The results of this comparison then are as follows: The worst case pointing errors for two configurations with 400-foot quadrapods, both weighing approximately 1300 pounds:

Configuration:	symmetrical	unsymmetrical with balancing sphere
Eccentricity:	0.030	0.015
Vertical error:	3.9 degrees	2.0 degrees
Yaw error:	7.5 degrees	2.5 degrees

Thus, it is seen that for similar weights the symmetrical case has a larger than specified error limit whereas the unsymmetrical case has less. At this point in the study it was decided at a coordination meeting that the unsymmetrical configuration would be dropped partly because of the complicated structure and erection procedure. In its place a second symmetrical configuration was substituted. The solar sails placed on opposite sides of a photolized wire mesh lens was suggested because it was believed that the structure on the earth side of the lens could be constructed so as not to interfere with the RF reflections. These two configurations were then studied for the remainder of the time.

Among the items examined in the final portion of the study were such details as the effect of the damper hitting its limiting stops and the effect of imperfections in the satellite structure. The damper was found to exert significant but not excessive impulse torques when the stops were struck during initial settling of the satellite. Structural imperfections which caused a shift in the CM increased the disturbance torques and even with a 450-foot quadrapod, the opaque lens satellite would have excessive error. This led to the decision to give preference to the solar sail satellite which would have small errors with a 300-foot quadrapod.

The remaining aspect of performance which was investigated was the initial behavior of the satellite. Because of the uncertainties of the unfolding and inflation processes, it is believed that the satellite would have large initial position errors and possibly large rate errors. These conditions were simulated by use of the digital computer to find the expected settling time. A moderate initial condition with the satellite starting at zero rate caused large librations which were damped to the steady-state level in about 3 days. More severe initial conditions with the satellite tumbling at three times orbital rate would require about 12 days to settle. Having shown that the satellite would settle even from conditions of tumbling, an investigation was made of a method of ensuring that the correct side of the satellite would face the earth. This method is the expedient of placing jets on the satellite which could be commanded from ground once the satellite had settled in the inverted position. The rockets could be sequenced by a timer so as to cause the satellite to rotate 180 degrees in pitch. However, a thrust in error of about 10 percent combined with the steady-state oscillation of the satellite resulted in unsuccessful flips. Thus, rockets with 5 percent accuracy would be required to avoid a more complicated system involving sensors. A more complete analysis of the satellite inversion is covered in Appendix V.

Mechanization of the Torque-Boom System

The torque-boom control and stabilization system consists of yaw and damper booms fixed with respect to one another but capable of being rotated relative to the satellite body. These booms are mounted on the upper canister half and are acted upon by the gravity gradient forces so as to align their combined axis of inertia along the satellite velocity vector. A small rotation drive allows the satellite, and thus the solar sailing surfaces, to be rotated beneath this stabilized boom structure. A dissipative damper mechanism located at the boom intersection point provides three-axis damping for the system. In this paragraph, the components required to mechanize this system are defined, and their properties investigated in order to verify the feasibility of the torque-boom system.

Booms and Tip Masses - The four booms of 200-foot length required for this system are considered to be the erectable, overlapped-tube type as manufactured by the DeHavilland Aircraft Company of Canada, Ltd. The ability of such booms to withstand the forces, torques, vibrations, and thermal deflections of this application is verified in Appendix XI. Although the booms may be considered self-erecting due to the inherent spring energy of the unreeling element, battery powered motors have been included in this application to increase system reliability and provide a controlled rate of erection. The reel, motor, and silver cadmium battery will be contained in a spherical tip mass, 14 inches in diameter. In addition to the above mentioned components, the two yaw boom tip masses will each contain two command receivers, a dipole antenna, and a receiver power supply. The latter consists of a N/P silicon solar cell array mounted on the surface of the 14-inch sphere and a 1 watt-hour Ag-Cd battery. The weights of the yaw and damper boom tips are 16 and 8 pounds respectively as tabulated below.

Yaw Tip Mass		Damper Tip Mass	
Reel and motor	5.00 lb	Reel and motor	5.00 lb
Receivers	2.50	Structure and ballast	3.00
Battery	0.10		

Yaw Tip Mass		Damper Tip Mass
Antenna	0.20 lb	
Solar Cells	6.20	
Structure and hardware	2.00	
	16.00 lb	8.00 lb

The solar cell and receiver weights include adequate protection for a 5-year life in the radiation environment of 2000 nautical miles. Electrical connection of the receivers to the rotation drive is provided by a flexible printed circuit tape contained within the yaw booms.

Rotation Drive - The rotation drive must be capable of applying small torques to the satellite so as to slowly rotate the satellite with respect to the stabilized boom structure. For the configurations considered, the torque is restricted to approximately 10^{-3} foot-pound to limit boom displacement from the velocity vector to several degrees. In order to rotate the satellite through an angle θ, in minimum time, maximum allowable torque should be applied to produce a constant acceleration for an angle of $\theta/2$, followed by constant deceleration to zero during the remaining angular distance of $\theta/2$. A torque-limited drive system would satisfy the above requirements; however, such a system becomes complicated by the presence of bearing friction and external disturbance torques. These torques are an order to magnitude higher than those of the drive system and could act to override the torque limited drive. In light of this situation, it became more practical to utilize a velocity control system which linearly increases and decreases the relative velocity of the satellite and boom structure so as to correspond to a constant acceleration followed by a constant deceleration.

A block diagram-schematic of the rotation system is shown in figure 2-4. The drive system consists of a stepper motor which is pulsed at a variable rate to produce the desired relative velocity. In order to obtain high reliability, the number of electrical and mechanical components has been minimized and digital rather than continuous control has been utilized. The linear velocity profile is obtained by the use of an astable or free-running multivibrator

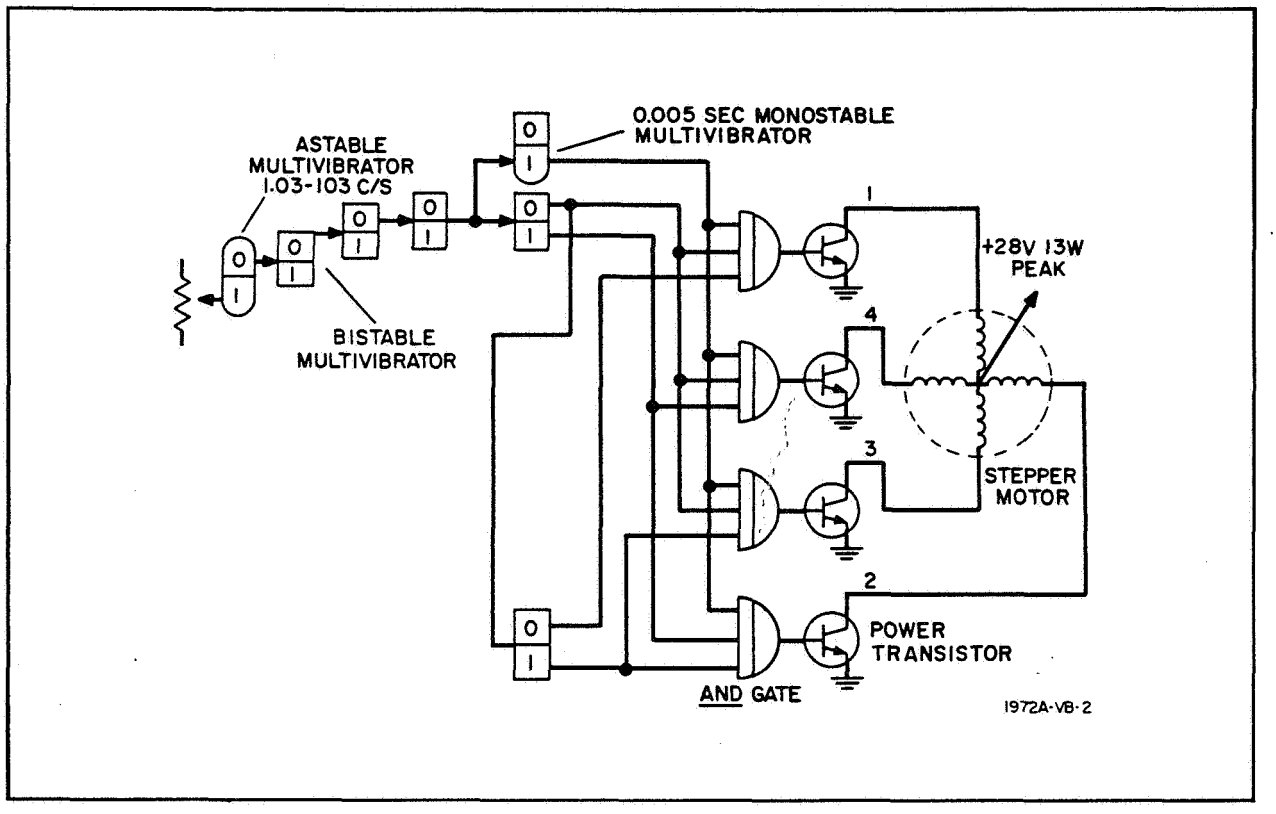

Figure 2-4. Control System Schematic

whose frequency is controlled by a variable resistor geared to the motor output shaft. The resistance is a function of angle of rotation δ such that the frequency and hence motor shaft speed follow the desired relationship $f = K\delta$, $O < \delta < \theta/2$. The remainder of the control circuitry consists of a frequency divider circuit, a counting circuit, and four power transistors to pulse the motor windings. A microswitch can be used to limit rotation.

The hardware required to mechanize the torque-boom system, figure 2-5, consists of a step-servo motor, a hermetically sealed harmonic drive, two alignment bearings, and a magnetic hysteresis damper. The harmonic drive unit manufactured by United Shoe Machinery is ideally suited for the torque-boom rotation drive in that it provides the ability to transfer positive rotary motion through a welded hermetic seal. The principle of this device is illustrated in figure 2-6. Rotation of the inner shaft turns an elliptoidal wave generator within a flexible hermetically sealed flexspline resulting in a

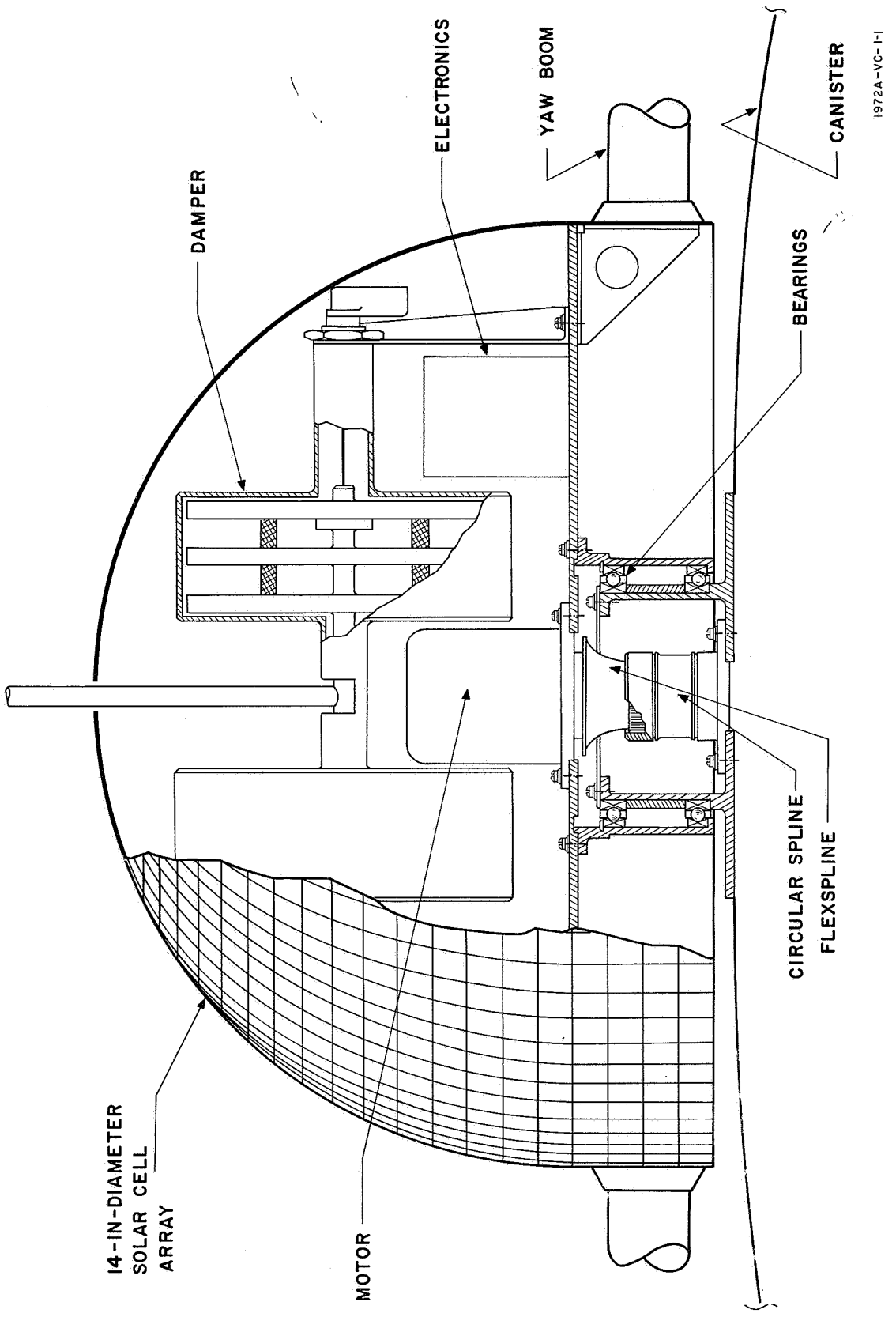

Figure 2-5. Canister Drive Layout

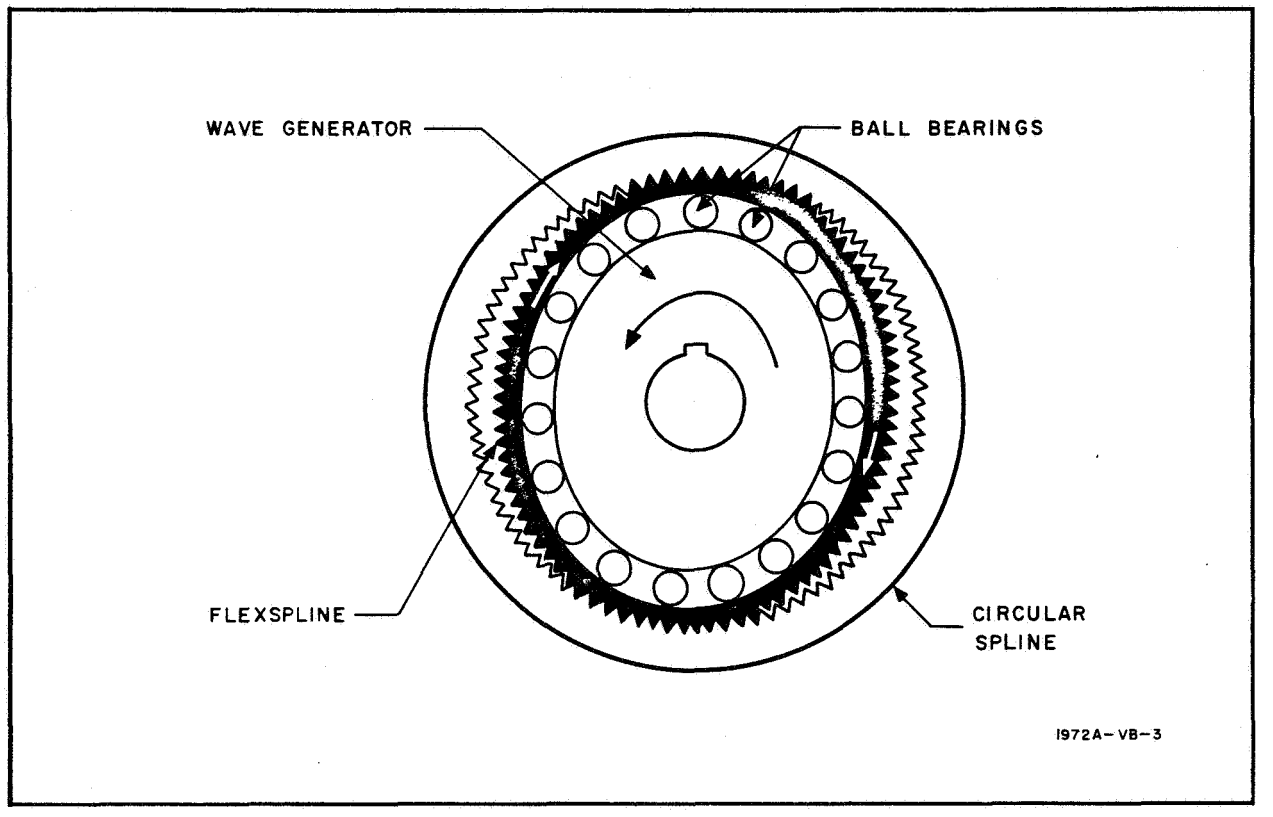

Figure 2-6. Harmonic Drive Principle

continuous and progressive engagement between the flexspline and the rigid circular spline. A difference in the number of teeth on these two splines causes the circular spline to turn with a positive but highly-reduced output motion. Such a technique allows the torque motor, variable resistor, and intermediate gearing to be housed in a sealed environment eliminating lubrication problems resulting from operation in a hard vacuum. This selection is supported by past experience which has shown that failure of a vacuum exposed drive system most commonly occurs in the first stage gearing. A size 11 step-servo motor has been selected to provide the input rotation. This unit is approximately 1 inch in diameter by 1.8 inches long, weighing 4.5 ounces. Previous space applications of harmonic drive units including satellite rotation drives and rocket servo-actuators have proven their ability to withstand the environmental extremes. In addition, a test program is underway at Goddard

Space Flight Center to determine the performance characteristics of harmonic drives in the space environment.

The only gearing exposed to space is the interface of the flexspline and the circular spline. A technique which has proven successful in prior space applications is the use of a low shear strength precious metal plating on the rigid circular spline. Additional lubrication is obtained through the use of a dry lubricant such as molybdenum disulfide. Because the slow speed rolling spline action of the harmonic drive involves essentially no surface sliding, there is negligible deterioration of the mating parts, and dry lubricants and platings remain in place and effective over prolonged periods. If, in addition to the low shear strength plating, the mating splines are fabricated from materials with low mutual solubility, the possibility of cold welding during periods of inactivity is eliminated.

A detailed investigation was conducted of the bearing requirements of this system in order to estimate their size, weight, and reliability. The two methods currently being considered for prolonged bearing life in space are:

- An enclosed bearing lubricated with a low vapor pressure grease
- An open bearing whose components are plated with or whose retainer is fabricated from a self-lubricating material.

While the long life requirements of this application prohibit the use of an enclosed bearing with a low vapor pressure lubricant, the low speed and low load characteristics are well suited to the use of a dry lubricant bearing. The bearings shown in the preliminary drive system layout are thin section, standard instrument bearings with a dry lubricant retainer replacing the conventional metal retainer. The retainer is an Ag-PTFE-WSe_2 matrix developed by the Westinghouse Research Laboratory for space and vacuum chamber applications. Each bearing has a bore diameter of 3.0625 inches with a 3.8750-inch O.D. and contains 36, 3/16-inch diameter balls. The weight per bearing is under 4 ounces. Conventional bearings using a Westinghouse retainer have been tested in ultrahigh vacuum at temperatures ranging from -320°F to +450°F for continuous operation in excess of 800 hours. The

performance was such as to justify a life prediction of over 10,000 hours continuous operation. Computation of the axial gravity gradient loads and radial bearing loads produced by roll and pitch moments allow the estimation of bearing friction at between 3×10^{-2} and 8×10^{-2} inch-pound. To assure a constant frictional torque during operational life, the bearings would be run in under relatively heavy load, disassembled, and cleaned, thus allowing a protective film of dry lubricant to be deposited on all bearing surfaces.

The power required for this system is approximately 1 watt and is provided by a solar cell-battery system. The 3.1-pound N/P silicon solar cell array mounted on the surface of the 14-inch diameter hemisphere includes sufficient shielding and initial excess capacity to assure a 5-year life in the 2000-nautical mile radiation region.

The functions of the dissipative damper mechanism for this application are:

- To constrain the damper rod to rotate about a particular axis
- To provide a damper rod rotational spring rate with a prescribed neutral point
- To provide a controlled dissipative torque which retards damper rod rotation.

The damper selected for this system is a magnetic hysteresis damper. The damper, as shown in figure 2-5, consists of two rotors mounted on a common shaft and suspended by a torsion wire. In figure 2-7, it can be seen that each rotor contains four Alnico permanent magnets which rotate within fixed permeable steel loss rings. The torsion wire suspension consists of wires held taut by flexed cantilever springs. The damper weight is estimated at 4 pounds and the rotor size is 5 inches in diameter by 2 inches thick. In addition to minimizing the weight and volume requirements the damper has the capability of being completely tested prior to launch. Figure 2-8 shows an experimental model of such a damper undergoing test at the Westinghouse Aerospace Division.

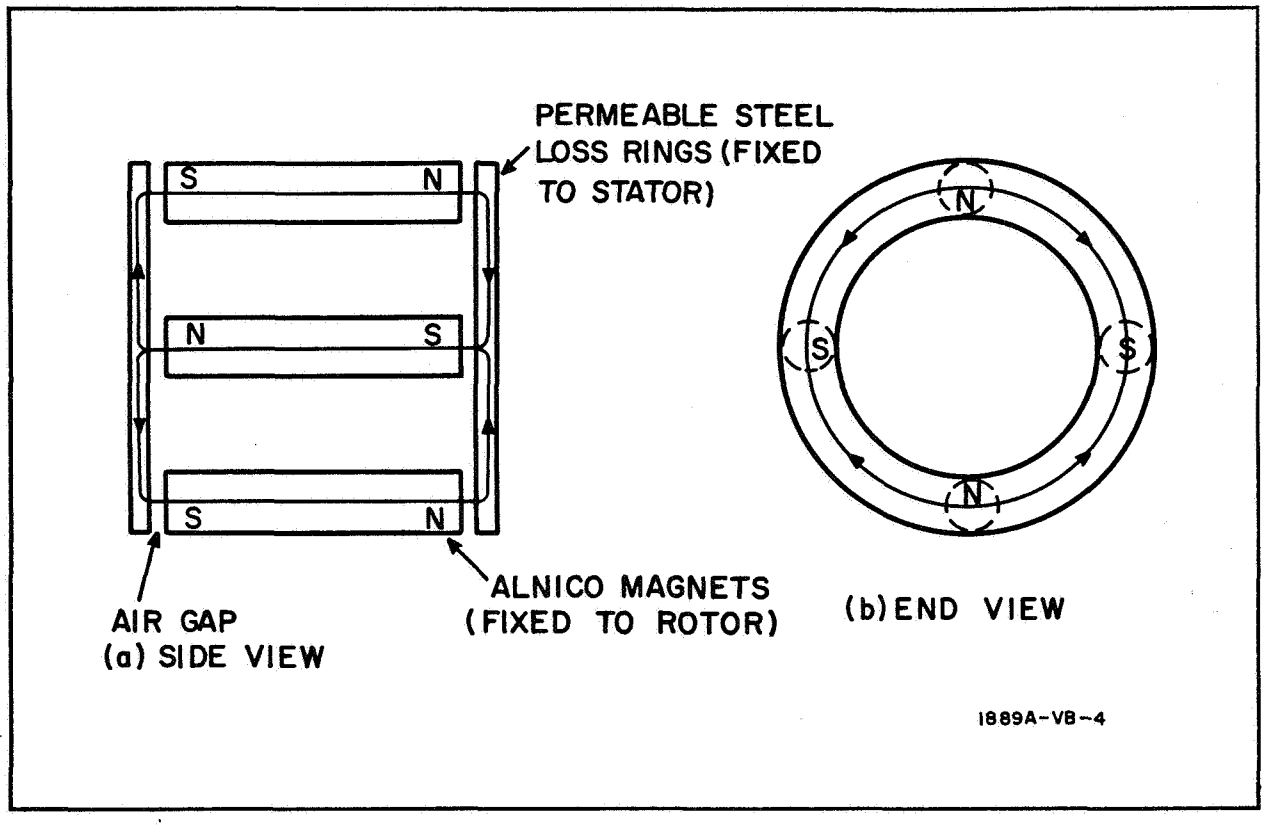

Figure 2-7. Rotor Schematic

Rotation Drive Weight Breakdown

Harmonic drive including motor	1.9 lb
Control electronics	0.5
Solar cell power supply and regulator	3.6
Damper	4.0
Structure including hardware, bearings, spline gear	7.0
	17.0 lb

Attitude Control System Weight Breakdown - A system weight breakdown is given below:

Rotation drive	17.0 lb
Yaw booms	38.4
Yaw tip masses	32.0
Damper booms	24.8
Damper tip masses	16.0
	128.2 lb

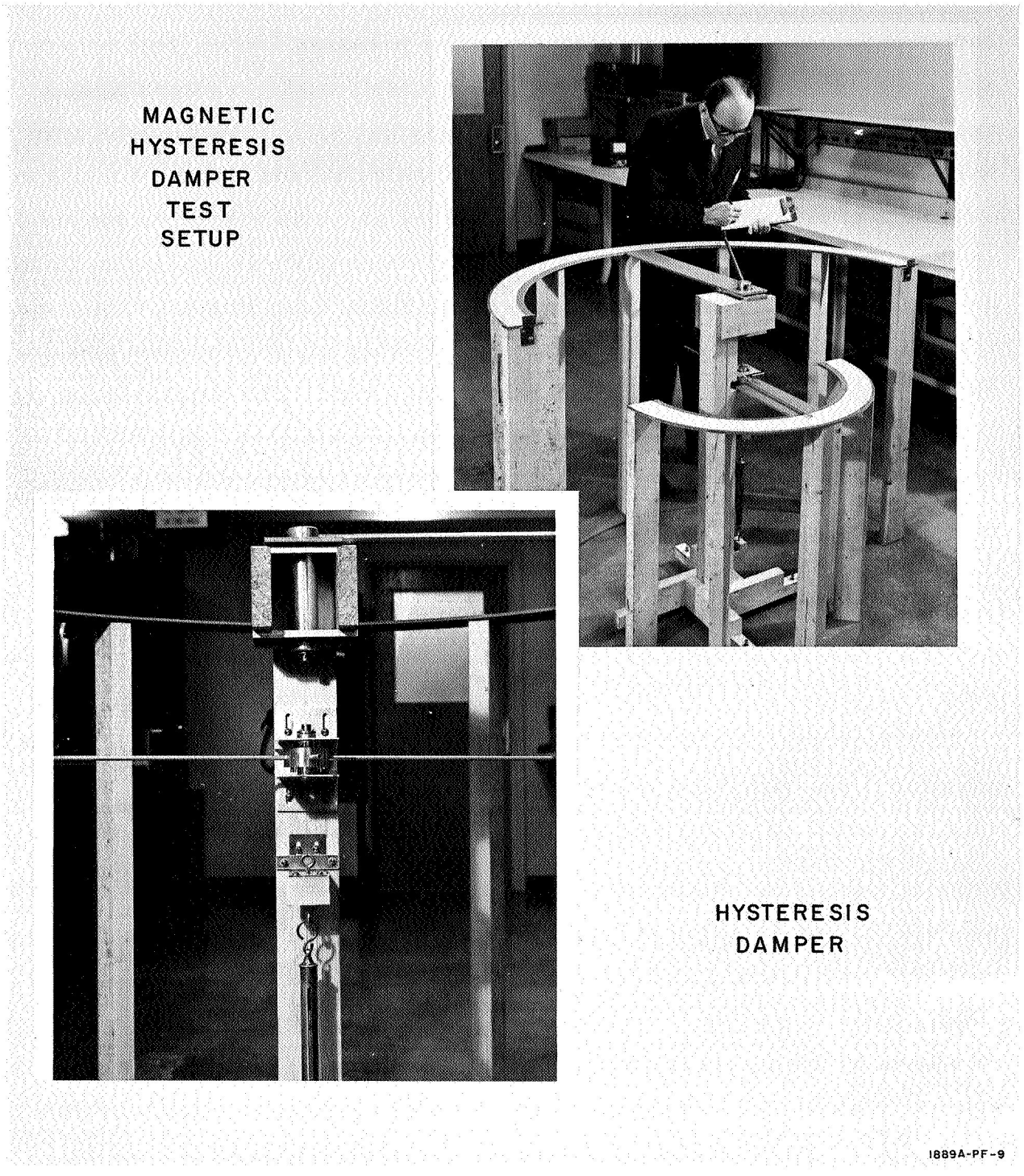

Figure 2-8. Damper Testing

Investigation of Relative Sail Mobilities - In previous studies of the control of communications satellites by means of solar pressure forces, both spherical- and lenticular-shaped structures have been considered. In extending this analysis to a class of vehicles controlled by solar sail, several steps have been taken. A digital computer program to calculate the forces on a sail as a function of the position and orientation of the sail with respect to the sun line has been developed. This program is based on an analysis similar to those described for the sphere and lenticule in the Phase I and Phase II final reports with the calculation of the reradiation forces being much simplified because of the elimination of the radiation exchange problem. The program is designed to output a force table which can subsequently be used in the mobility programs.

In order that the relative capabilities of various combinations of coating patterns on the sail could be studied without resorting to a large number of computer runs, an expression for the mobility of a sail under the influence of direct solar forces has been derived only for the situation where the sun line is in the plane of the orbit and the sail is maintained normal to the plane of the orbit.

This derivation is presented in detail in Appendix IV. It shows that for this situation the mobility is directly proportional to the expression:

$$\frac{a_2 \epsilon_1 - a_1 \epsilon_2}{\epsilon_1 + \epsilon_2}$$

where γ, ϵ, and α are the reflectivity, emissivity, and absorptivity of the sail material, respectively, and the subscripts 1 and 2 indicate the two sides of the sail.

As can be seen from this expression, as high as possible a reflectivity and emissivity on one side of the sail and as low as possible a reflectivity and emissivity on the other side will produce a maximum amount of mobility.

At an early coordination meeting, representatives of the Goodyear Aerospace Division indicated that any combination of reflectivities between 0.9 and 0.1 with emissivities between 0.7 and 0.1 (upper limit later raised to 0.8) could be achieved for the sail surface. Of the many possibilities offered by this wide range of thermal characteristics, the most efficient combination was to have the reflectivity and emissivity of one side 0.9 and 0.7, respectively, and to have both the reflectivity and emissivity of the opposite side equal to 0.1. For this reason, a coating pattern having those characteristics was used in many of the early studies.

Phillips Concept of Orbit Position Control - In previous studies of orbit position control for spherical- and lenticular-shaped satellites, the concept has been to apply differently coated surfaces to the satellite in a pattern symmetrical with respect to the roll axis and to maintain the yaw orientation such that different reflective and emissive surfaces are exposed to the sun during the receding and approaching halves of the orbit.

However, in the case of a satellite having a solar sail, an entirely different technique of orbit position control is possible. In a concept proposed by Mr. W.H. Phillips of the NASA Langley Research Center, an orbit-positioning control force can be obtained by varying the projected area of the sail with respect to the sun line vector. This technique requires that a yaw oscillation of twice the orbital period be induced on the satellite such that the plane of the sail would be mostly perpendicular to the solar force vector during half the satellite's orbit when it recedes or approaches the sun and mostly parallel during the opposite half of the satellite's orbit.

Appendix I describes a study made of the basic Phillip's concept, which involves a sinusoidal yaw of twice the orbital period, and of two modifications to the techniques which are designed to increase the orbit position control capabilities of the system. The first modification called the rotational Phillip's concept involves imposing a constant rotation about the radius vector of twice the orbital period on the sail. The second modification involves

keeping the sail halfway between the sun line and the plane of the orbit and damping the oscillation for higher sun line inclinations in an effort to increase the capabilities in the region of high sun line inclinations.

The basic conclusions which can be drawn from this study of the Phillips concept of orbit position control are:

- The basic Phillips technique using an oscillation of up to 50 degrees does not produce as much mobility in any region of sun line inclination as does the yaw-stabilized technique using an optimum coating pattern.
- The rotational Phillips technique, while producing a slightly better mobility when the sun line is in the plane of the orbit, drops off much more rapidly with increasing sun line inclination than does the yaw-stabilized technique.
- The solar-oriented Phillips technique, while extending the region of control to higher sun line inclinations by a redefinition of the opposite modes of operation, does not produce as much mobility at the low sun line inclinations as does a similar mating of the yaw-stabilized technique with the solar-oriented technique.
- All three Phillips methods require continuous active attitude control systems.

In general then, because of the somewhat lower mobility and because of the requirement for a continuous active control system, the Phillips techniques are not considered to be practical for obtaining orbit position control.

Orbital Eccentricity Study - The nature and causes of several different types of orbital eccentricity are described in both the Phase I and Phase II final reports. A further study has been made in this area to determine the maximum eccentricity of the two configuration satellites at the orbital altitude being considered. The details of this study are shown in Appendix V.

In general, it is shown that posigrade orbits have a significant advantage over retrograde orbits with respect to eccentricity in the region of the best communication orbits. Specifically, the maximum eccentricities reached at three inclinations of interests are:

Configuration \ Inclination	45 Degrees	60 Degrees	75 Degrees
A	0.048	0.030	0.047
B	0.015	0.010	0.015

There is a small region of resonance in this area between the inclinations of 47 and 55 degrees into which it is not practical to place a long-lifetime satellite. In general, the eccentricities of the configuration B satellite are shown to be approximately a factor of three less than the configuration A satellite. This phenomenon occurs even though the weight of the configuration B satellite is considerably less than that of the configuration A satellite since the average projected area of the configuration B satellite is almost a factor of five less than that of the configuration A satellite.

The eccentricity information obtained in this study, in addition to being used to avoid regions of resonance, has also been used as a design criteria in the development of the attitude control system (see that portion of the text entitled Attitude Control System), since that system is sensitive to the magnitude of the orbital eccentricity.

Skin Temperature, Mobility Tradeoff Study - In order to determine a set of surface coatings which would produce both feasible skin temperatures and sufficient mobility for both the opaque lenticule and the sail, a study has been made to determine the trends of both of these quantities as functions of the coating pattern. The details of this study are described in Appendixes VI and VII.

The final coating configurations chosen for the two satellites and the associated skin temperatures at selected points of the orbit are shown in figures 2-9 and 2-10. The choices were made on the basis of the configurations which would produce the largest amount of mobility, while still maintaining the surface temperatures under the 250° F maximum temperature limit specified by Goodyear representatives.

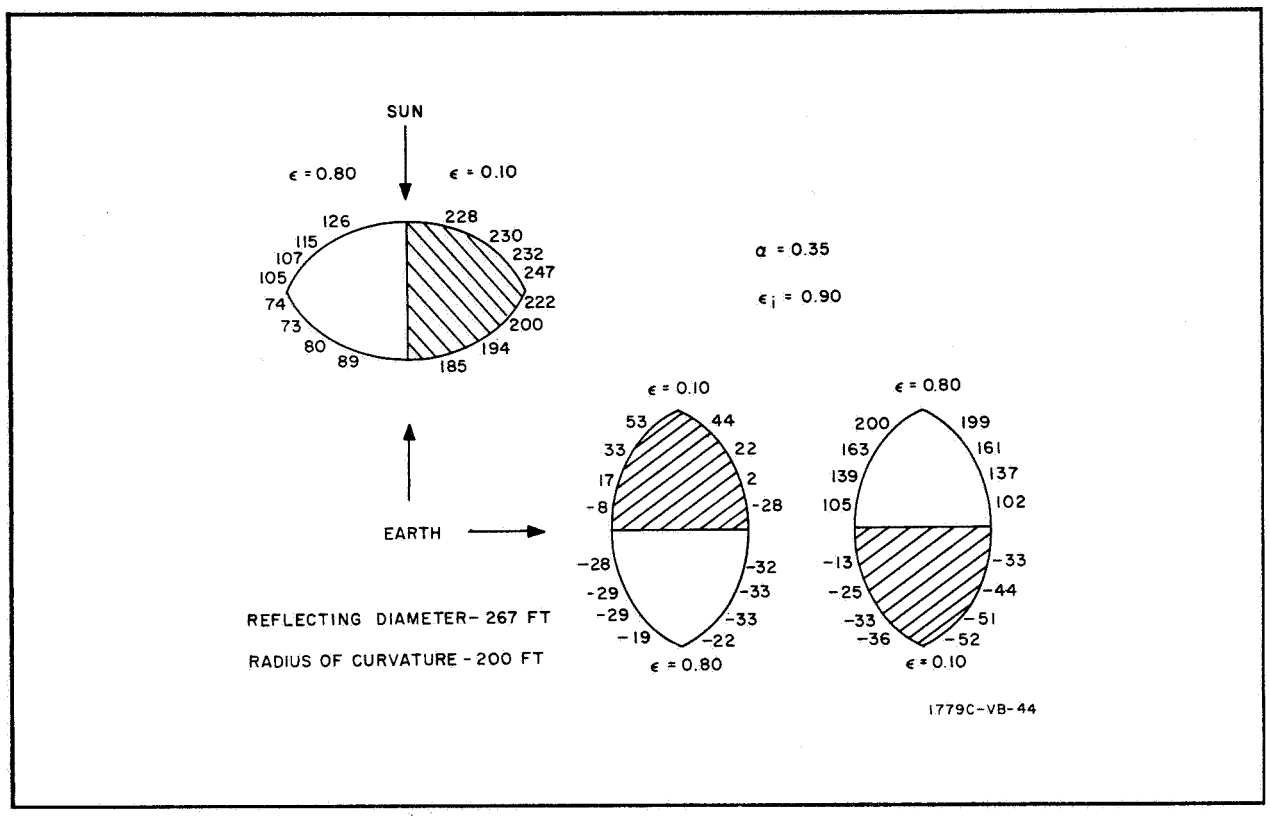

Figure 2-9. Final Lenticule Coating Configuration and Temperatures

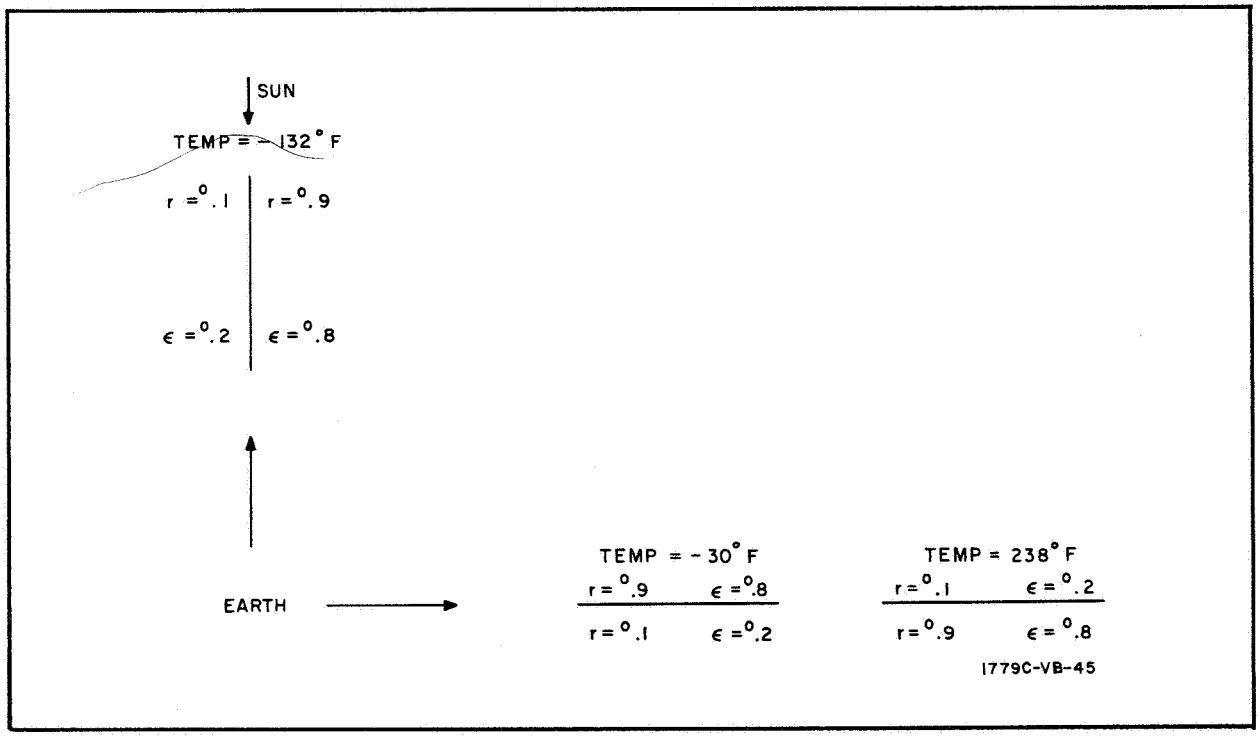

Figure 2-10. Final Sail Coating Configuration and Temperatures

As can be seen from figure 2-9, the skin temperatures on the lenticule range between a minimum of -52°F and a maximum of 247°F. The mobility of this configuration was estimated to be approximately 101 degrees per month at a weight of 1200 pounds. Similarly, the temperature on the sail is seen to vary between -132°F and 238°F. The minimum temperature shown for the sail is probably somewhat pessimistic since it was calculated at the point where the sun line vector lies in the plane of the sail, and thus, the solar incident radiation was assumed to be 0.

Sail and Lenticule Mobility Study - The two different configuration satellites being studied in this project use different means of achieving both communications and orbit position control capabilities. The configuration A satellite uses an opaque lens both as the reflecting medium for communications and as the means of achieving orbit position control. The configuration B satellite uses a photolyzable wire mesh lens as the reflecting medium and a plane sail material as the means of achieving orbit position control.

In order to achieve orbit position control with the opaque lens, a symmetric coating pattern is applied to the satellite with the axis of symmetry lying in the plane of the rim. Orbit position control is then achieved by aligning the axis of symmetry in opposite directions along the velocity vector of the satellite.

However, in the case of a plane sail, several other control techniques become possible and, in fact, produce greater mobility than a method similar to the lenticular control which for the sail will henceforth be called the uncompensated control technique. This method which aligns the sail normal vector in opposite directions along the velocity vector, can be shown (Appendix VIII) to be optimum only when the sun line vector lies in the plane of the orbit.

It is shown in Appendix VIII that as the sun line moves out of the plane of the orbit, other yaw angles will produce more mobility than does the nominal 0 yaw angle (sail normal to velocity vector). Furthermore, it is shown that the optimum yaw angle will vary between 0 and 45 degrees (and symmetrical equivalents) throughout the full range of sun line inclinations. This suggests two other control schemes taking better advantage of the available mobility throughout, the full range of sun line inclinations.

The first of these, henceforth called continuous compensation control, would involve a continuous adjustment of the satellite yaw angle to compensate for the varying sun line inclination. At any particular value of sun line inclination, the yaw angle would be set to the angle which produces the greatest amount of mobility. This control technique would thus produce an optimum mobility, but would also require the ability of stabilizing the yaw angle at any desired value.

The other method, henceforth called fixed compensation control, would involve the selection of a fixed yaw angle which would produce a balanced mobility curve throughout the full range of sun line inclination. The fixed yaw angle required to produce a balanced curve is shown to be 22.5 degrees (and symmetrical equivalents in Appendix VIII). While this does not produce an optimum mobility, it does simplify the attitude control requirements in that stabilization is necessary at only four discrete yaw angles (plus two additional angles to provide neutral mode capabilities).

The relative mobilities of the lenticule and the three different sail control techniques are shown in Appendix VIII. Average mobilities based upon calculated distributions of sun line inclinations are also shown.

Based upon these figures, the sail area required to match the mobility of the opaque lens is shown in figure 2-11. These areas have been calculated using the average mobilities of the final coating configurations as shown in Appendix VIII along with the actual weights of 1152 pounds for the lenticule and 777 pounds for the sail. As can be seen, the fixed compensation and continuous

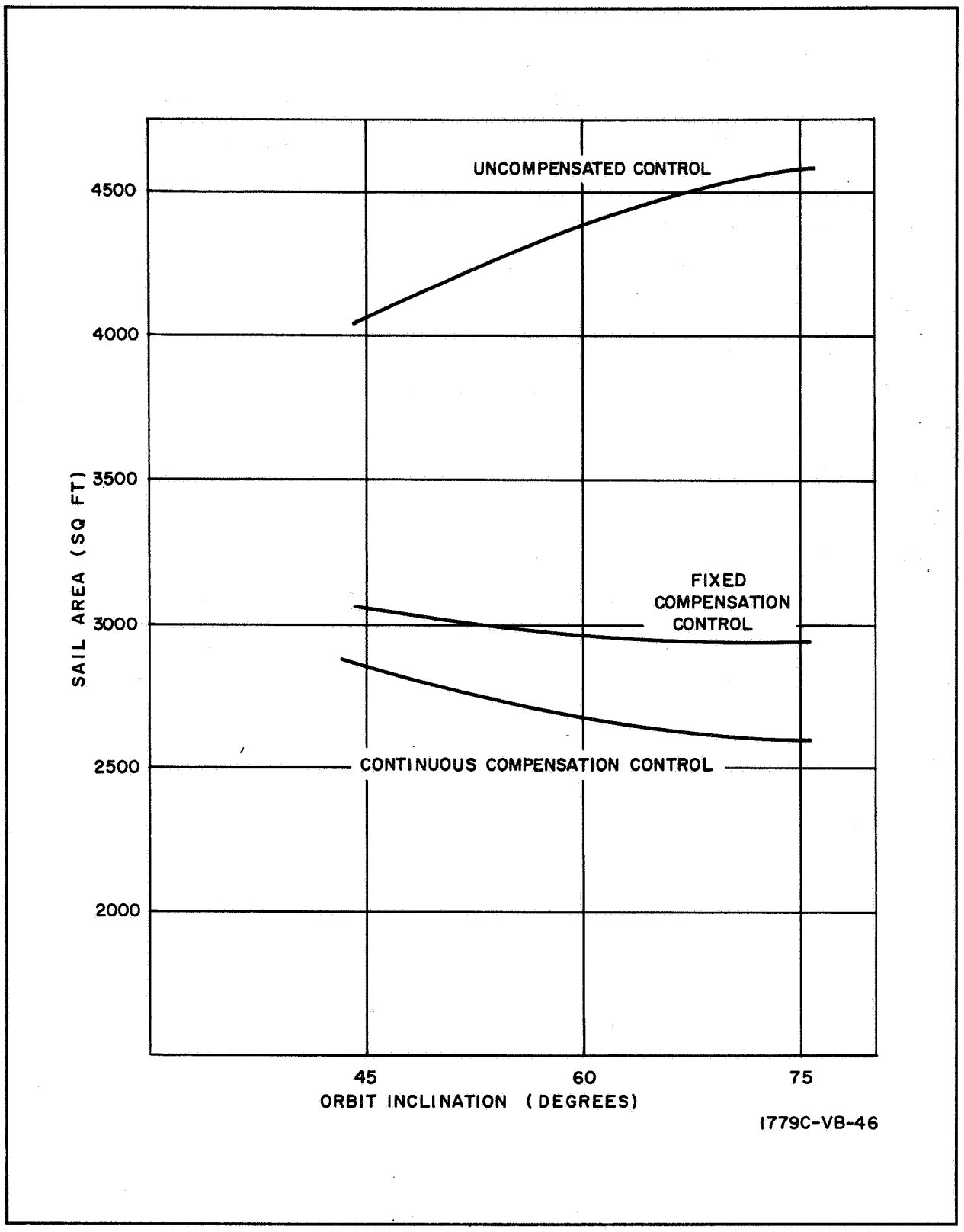

Figure 2-11. Required Sail Areas

compensation control schemes require considerably less sail area than does the uncompensated control technique. However, it does not appear that the continuous compensation scheme offers a nearly large enough improvement over the fixed compensation scheme to warrant the required complications in the attitude control system. For this reason, the fixed compensation scheme has been chosen for use in the remaining studies.

Figure 2-12 shows the average mobility of the two configurations (matched), along with the maximum and minimum mobilities of both the opaque lens and the sail under the fixed compensation control technique. As can be seen, the average mobility is approximately 130 degrees per 30 days. The maximum and minimum mobilities of the sail are more balanced with respect to the average because in this case (see figure VIII-4) the minimum mobility can occur at either 0- or 90-degree sun line inclinations, while for the lenticule the minimum (see figure VIII-6) occurs when the sun line is perpendicular to the orbital plane which in itself will rarely occur. The point of maximum change in semi-major axis per orbit for the lenticule is also seen to occur near the average value for that curve, thus explaining the relative proximity of the maximum and average mobility curves for the lenticule.

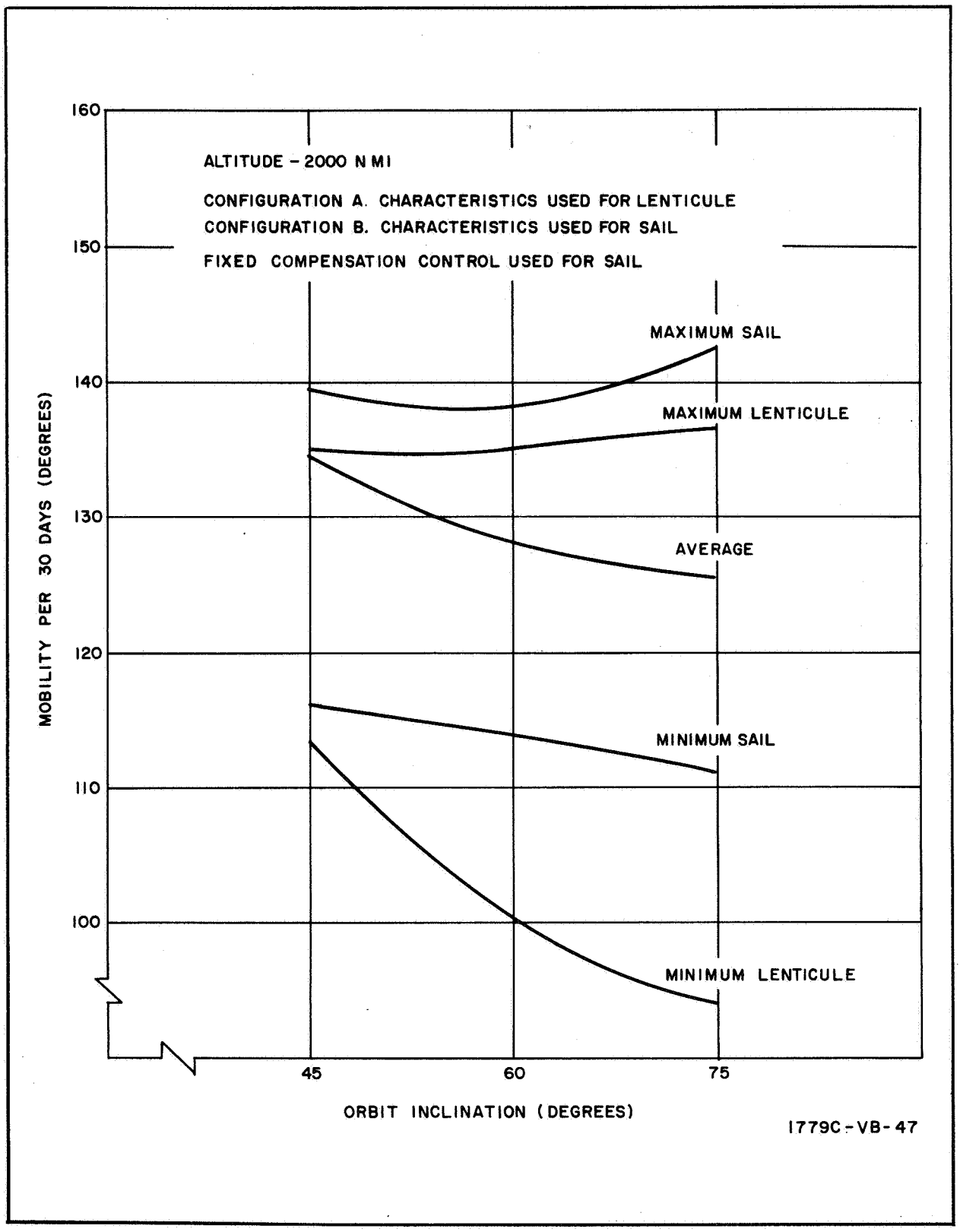

Figure 2-12. Maximum, Minimum, and Average Mobilities

Scaling Criteria - The satellite size and weight may be scaled according to a number of criteria as altitude varies. Refering to figure 2-13 for definition of the parameters involved, the criteria used in the scaling were as follows.

As the altitude of the satellite orbit was assumed to vary from a nominal altitude of 2000 nmi, the required coverage (β) was maintained constant until the altitude change was sufficient that the number of satellites in the orbit could be increased or decreased by one; at that time, the required coverage was changed in accordance with the changed satellite number. For example, if four equally spaced satellites are assumed, each must have a ground coverage of $2\beta = 90$ degrees. For a minimum elevation angle, α, of 5 degrees, this requires an altitude of at least 1840 nmi. For five satellites, an altitude of at least 970 nmi is required to provide a ground coverage of $2\beta = 72$ degrees. Table 2-1 below lists the number of satellites and the ground coverage angle for various altitude ranges, where a minimum elevation angle of $\alpha = 5$ degrees was assumed:

TABLE 2-1

NUMBER OF SATELLITES AND GROUND COVERAGE ANGLE FOR VARIOUS ALTITUDE RANGES

Altitude Range (nmi)	2β (degrees)	No. of Satellites
970 - 1840	72	5
1840 - 4680	90	4
Greater than 4680	120	3

The radius of curvature of the satellite is assumed to vary with altitude in such a way that the received signal strength of the edge of the region of ground coverage is constant. Since the signal strength varies in proportion to effective cross section (which is proportional to the square of the radius of curvature) and as the reciprocal of the fourth power of range, this is equivalent to requiring that ρ^2/R_{max}^4 be maintained constant.

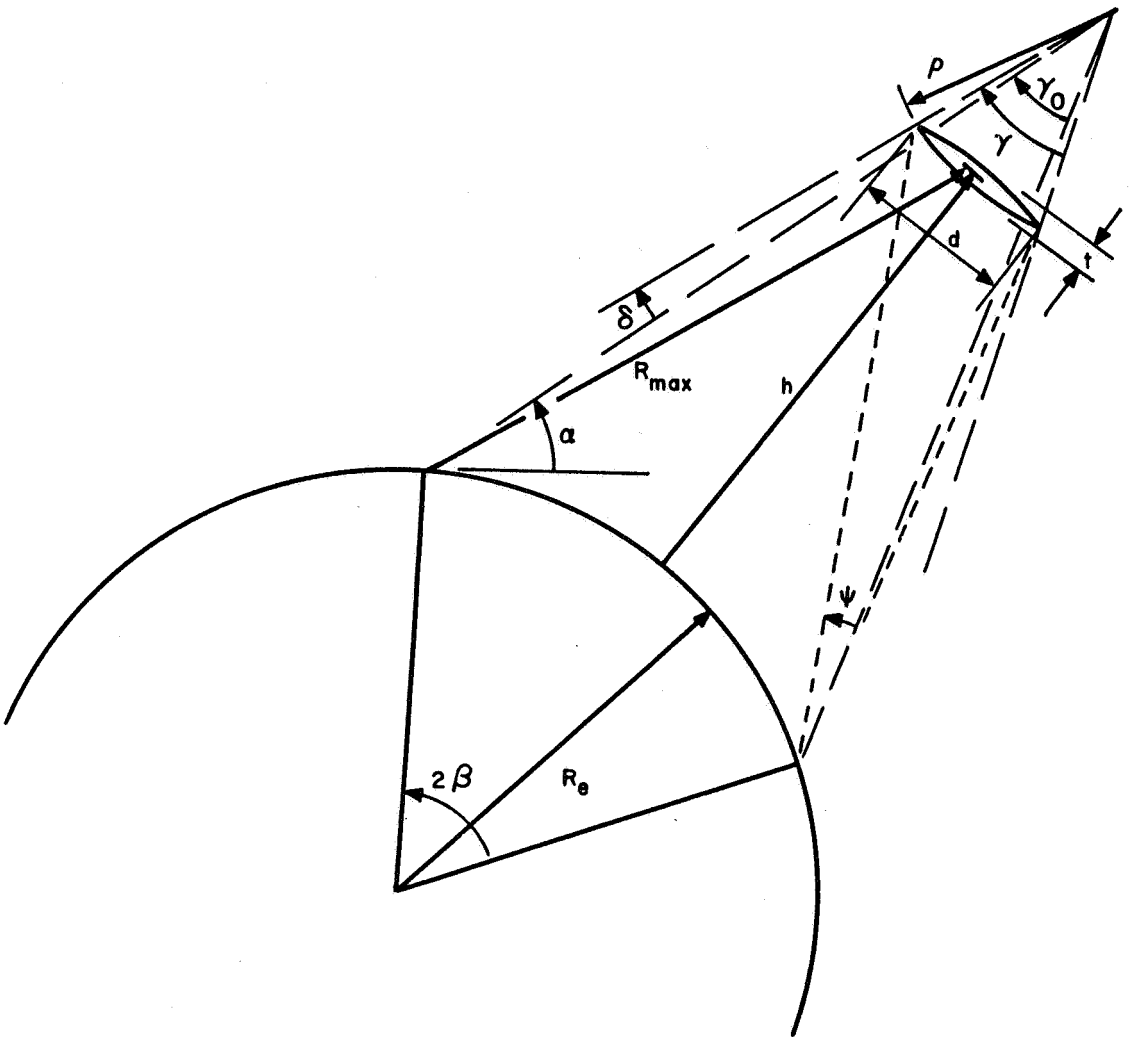

R_e = EARTH RADIUS

h = SATELLITE ALTITUDE

ρ = SATELLITE RADIUS OF CURVATURE

γ_0 = REQUIRED COVERAGE (VIEWED FROM SATELLITE)

d = LENS DIAMETER (FEET)

t = LENS THICKNESS

2β = REQUIRED COVERAGE (VIEWED FROM EARTH CENTER)

γ = LENS DIAMETER (DEGREES)

δ = ATTITUDE ERROR

α = MINIMUM ELEVATION ANGLE

ψ = INTERCEPTED HORIZON BEAM ANGLE

R_{max} = MAXIMUM SATELLITE RANGE

1779C-VB-48

Figure 2-13. Satellite Scaling Parameters

The attitude error was assumed to be constant.

Scaling Rules - The equations used to scale the various satellite dimensions and weights are:

- Determine the required lens diameter in degrees:

$$R_{max} = (R_e^2 + (R_e + h)^2 - 2 R_e (R_e + h) \cos \beta)^{1/2}$$

$$\gamma_o = 2 \sin^{-1} \frac{R_e \sin \beta}{R_{max}}$$

$$\gamma = \gamma_o + 2 \delta$$

- Determine radius of curvature ρ by scaling in proportion to R_{max}^{-2}.
- Determine the lens area, diameter, and thickness:

$$d = 2 \rho \sin \frac{\gamma}{2}$$

$$A = 4\pi \rho^2 (1 - \cos \frac{\gamma}{2})$$

$$t = 2 \rho (1 - \cos \frac{\gamma}{2})$$

- Scale lens weight in proportion to lens area.
- Scale torus and rim weight by the 1.68^{th} power of lens diameter.*
- Scale inflation system weight by the 1.57^{th} power of lens diameter.*
- Scale boom weight by the 4/3 power of diameter (based on maintaining a constant torsional spring constant for the booms, and assuming a cylindrical boom with constant thickness walls and with length proportional to the lens diameter).
- Assume 64-lb fixed weight in the yaw-control equipment.

Using these rules, figure 2-14 shows the various scaled parameters as a function of altitude, for the satellite configuration employing an opaque, nonphotolyzable lens and a photolyzable torus. Results for the satellite configuration employing the wire grid lens are similar if the weights are interpreted as launch weights.

---

* These factors were obtained by comparing weights of the 50-ft test satellite and the 267-ft full scale satellite, GAC Report GER-11502, 1 June 1964.

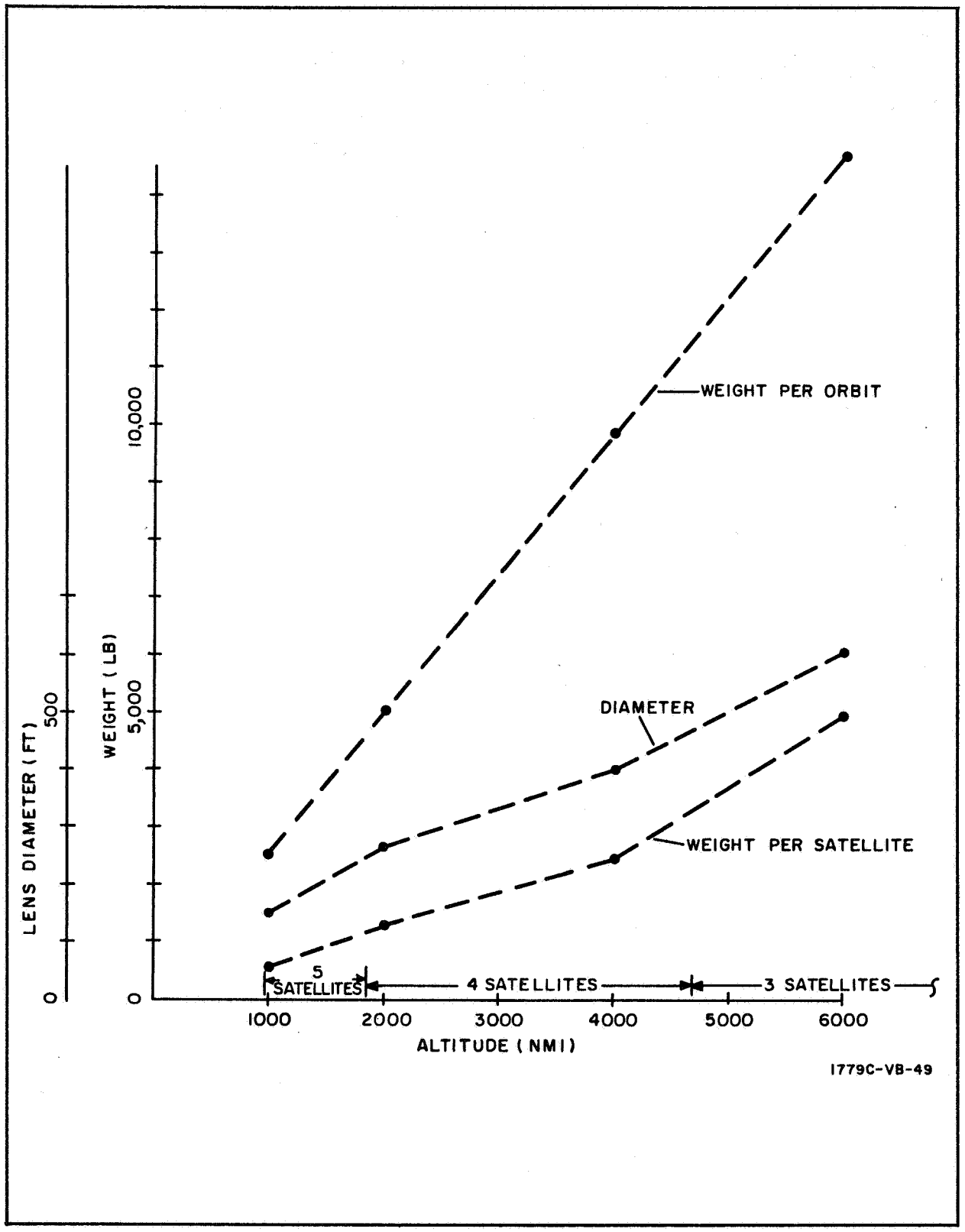

Figure 2-14. Satellite Weight and Lens Diameter vs Altitude

Inertia and Length Considerations - If the proportions of the satellite remained unchanged during scaling, the inertia ratios would remain unchanged and the response to disturbances which occur at a rate constant with respect to orbital rate would remain unchanged except by a scale factor. For example, the small angle equations in pitch, for a circular orbit, are

$$\ddot{\theta}\ I_p + 3\omega_o^2\ (I_r - I_y)\ \theta = M(t)$$

where

θ is the pitch angle

I_p, I_r, I_y are the inertias about the pitch, roll, and yaw axes

ω_o is the orbital rate

M (t) is an external applied torque.

In the s plane,

$$\theta(s) = \frac{M(s)}{s^2 I_p + 3\omega_o^2 (I_r - I_y)}$$

If a similar satellite ($I_p' = k_2 I_p$, $I_r' = k_2 I_r$, $I_y' = k_2 I_y$) were placed in a different orbit ($\omega_o' = k\omega_o$), then the applied torque will differ by a scale factor in amplitude and time, for torques (such as solar torque) which occur at a rate depending upon the orbital rate. Thus

$$M'(t) = k_1 M(kt)$$

$$M'(s) = \int_o^\infty k_1, M'(kt)\, e^{-st}\, dt$$

$$= \frac{k_1}{k} M\left(\frac{s}{K}\right)$$

Then the resulting response is

$$\theta'(s) = \frac{M'(s)}{s^2 I_p' + 3\omega_o'^2 (I_r' - I_y')}$$

$$= \frac{\frac{k_1}{k} M\left(\frac{s}{K}\right)}{\frac{s}{K}^2 k^2 k_2 I_p + 3k^2 \omega_o^2 (k_2 I_r - k_2 I_y)}$$

$$\theta'(s) = \frac{k_1}{k^2 k_2} \left(\frac{1}{k} \frac{M\left(\frac{s}{K}\right)}{(s/K)^2 I_p + 3\omega_o^2 (I_r - I_y)} \right)$$

$$\theta'(t) = \left(\frac{k_1}{k^2 k_2} \right) \theta(kt)$$

The response thus varies by a scale factor in time (k) and a scale factor in amplitude.

The scale factor in amplitude is

$$\left(\frac{k_1}{k^2 k_2} \right) = \left(\frac{M'}{M} \right) \left(\frac{\omega_o}{\omega_{o'}} \right)^2 \frac{I_p}{I_p}$$

where

(M'/M) is the ratio of torque amplitudes

(ω_o/ω_o') is the ratio of orbital rates

(I_p/I_p') is the ratio of pitch inertia

If the attitude errors resulting from disturbance torques are to remain constant, the scale factor should be one. This is not necessarily consistent with the scaling rules adopted in scaling the satellite size and weight with altitude.

Table 2-2 shows values of scale factor amplitude versus altitude for the scaled satellites, (opaque lens configuration) where the pitch inertia of the lens and rim have been assumed negligible and the torque amplitudes have been assumed to vary in proportion to lens diameter. (If the lens shape remained unchanged, solar torque could be expected to vary with the cube of lens diameter. Since the lens actually is flattened somewhat as the diameter increases, the actual variation would be somewhat less. Calculation of solar torque for several lens diameters indicates that variation in direct proportion to lens diameter is a reasonable assumption in this case.)

TABLE 2-2

VALUES OF SCALE FACTOR AMPLITUDE VERSUS ALTITUDE

Altitude (nmi)	Satellite Length (ft)	Scale Factor
1000	500	1.22
2000	720	1.0
3000	990	1.28
4000	1430	1.02

It may be seen that these variations are small.

Another factor to be considered is the variation in pitch, roll, and yaw natural frequencies due to the fact that under the chosen scaling laws, the inertia ratios of the scaled satellites do not remain constant as assumed above. Table 2-3 illustrates the variation of these factors for the opaque lens configuration, with the pitch, roll, and yaw inertias for 2000-nmi altitude taken to be 18.2×10^5, 17.6×10^5, and 3.2×10^5 slug ft^2, respectively.

TABLE 2-3

VARIATION OF FACTORS FOR OPAQUE LENS CONFIGURATION

		Natural frequency / ω_o	
h (nmi)	Yaw	Pitch	Roll
1000	0.7	1.64	1.98
2000	0.42	1.59	1.88
4000	0.39	1.52	1.84
6000	0.35	1.46	1.81

Note that at 1000-nmi altitude, the roll natural frequency is nearly twice orbital frequency. Since solar torque disturbances in roll occur at a basic frequency of ω_o, this change in natural frequency should not be significant. However, more complete analyses, including the effects of other disturbing torques, should be made to confirm this supposition. If desired, the natural frequencies may be adjusted by varying the satellite length and thus the inertia ratios. This would also effect the magnitude of the response scale factor,

and again a more detailed analysis would be required to determine these effects quantitatively. These changes would be expected to have only minor effect on the satellite weights illustrated in figure 2-14.

3. CONCLUSIONS AND RECOMMENDATIONS

Conclusions

The results of this study demonstrate the technical feasibility of employing orbit position by solar radiation to a gravity-gradient-stabilized passive communications satellite.

The study was conducted specifically at an altitude of 2000 nautical miles, but reasonable extrapolations have shown feasibility from 1000 to 6000 nautical miles.

The results can be summarized as follows:

- A satellite comprising a lens 267 ft in diameter, consisting of two 84-degree spherical segments of a 200-ft-radius sphere would weigh less than 1500 lb.
- A mobility or separation of two satellites in opposite modes would be greater than 100-degrees per month.
- Configurations with optically transparent lens material and planar sails are feasible with either a symmetrical or asymmetrical gravity-gradient structure.
- Configurations with an opaque lens material are feasible with a symmetrical gravity-gradient structure.
- All moving or active systems required can be prelaunch-tested if required.

Further Study Recommendations

Three study areas are suggested to aid in the evaluation of this satellite as a communications system element and to aid in optimization.

- A rigorous extrapolation of significant parameters from 6000 nautical miles to synchronous altitude.
- Analysis and measurement of realizable materials with regard to the forces and torques from solar pressure on surfaces which have reflection characteristics that are between the specular and diffuse limits.

- Derivations and evaluation of new configurations and techniques predicated on the development of significantly lighter reflective and structural materials to aid in establishing the value of further effort to develop these materials.

APPENDIX I
PHILLIPS CONCEPT OF ORBIT POSITION CONTROL

This appendix describes a study made of the basic Phillips concept, which involves imposing a sinusoidal yaw oscillation of twice the orbital period on the sail in order to obtain a differential area over the orbit, and of two modifications to the technique which are designed to increase the orbit position control capability of the system. A comparison of results with those obtained from studies of the yaw-stabilized technique is given and shows the Phillips concept to be somewhat inferior to the yaw-stabilized technique.

Basic Phillips Concept

In the basic Phillips concept, a sinusoidal yaw oscillation of twice the orbital period is imposed on the satellite. The oscillation must be referenced to the sun line in such a manner that there is a net difference in projected area of the sail to the sun line in approaching the receding halves of the orbit. The manner in which this referencing has been accomplished is illustrated in figure I-1 where $\overline{N}$ is a unit vector normal to the plane of the orbit such that the satellite motion about it is clockwise and $\overline{r}_s$ is the sun line vector. Then the projection of the sun line into the orbital plane is defined by:

$$\overline{r}_{sp} = (\overline{N} \underline{X} \overline{r}_s) \underline{X} \overline{N}$$

and the perigee vector $\overline{r}_p$ can be defined from the orbital elements by:

$$\overline{r}_p = \begin{bmatrix} \cos \Omega \cos \omega - \sin \Omega \cos \text{in} \sin \omega \\ \sin \Omega \cos \omega \cos \Omega \cos i \sin \omega \\ \sin i \sin \omega \end{bmatrix}$$

Where i, Ω , and ω are the inclination, right ascension, and argument of perigee of the orbit. Then the angle between the perigee vector and the projected sun line vector defined as positive in the direction of motion is:

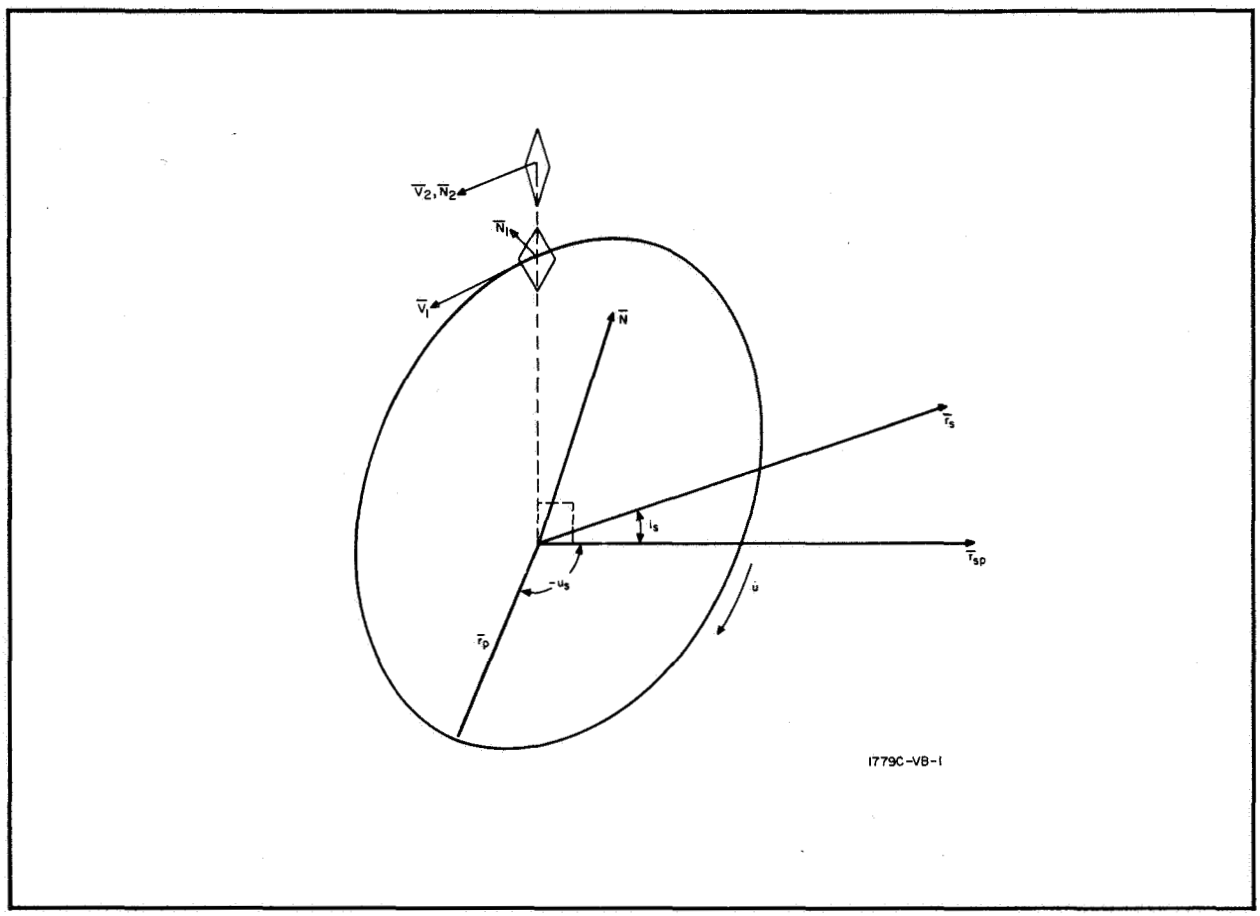

Figure I-1. Reference Orientation of Satellite

$$u_s = \tan^{-1}\left[\frac{-(\bar{r}_p \times \bar{r}_{sp}) \cdot \bar{N}}{\bar{r}_p \cdot \bar{r}_{sp}}\right]$$

This angle will then correspond to the true anomaly of the satellite when it lies on the projected sun line vector. Then, at a point 90 degrees from the projected sun line vector, the plane of the sail should be parallel to the velocity vector if in a decreasing energy mode and, conversely, should have maximum deviation from the velocity vector if in an increasing energy mode. Thus, the angle between the plane of the sail and the velocity vector for the two modes of operation can be expressed as:

$$\psi_I = \psi_A \cos \left\{ \frac{\left[t(u) - t\left(u_s + \frac{\pi}{2}\right) \right]}{P} \right\}$$

$$\psi_D = \psi_A \sin \left\{ \frac{\left[t(u) - t\left(u_s + \frac{\pi}{2}\right) \right]}{P} \right\}$$

where ψ_A is the amplitude of the sinusodial oscillation, P is the orbital period, and t (u) is the time from perigee and is given by:

$$t(u) = \frac{\sqrt{1 - e^2}}{2\pi} \left\{ \frac{-e \sin u}{1 + e \cos u} + \frac{2}{\sqrt{1 - e^2}} \tan^{-1} \left[\frac{(1 - e) \tan\left(\frac{u}{2}\right)}{\sqrt{1 - e^2}} \right] \right\}$$

The simplified mobility program has been run with two satellites in opposite modes of operation having sail orientations as described above. The change in semi-major axis of each satellite per orbit is shown for several different amplitudes in figure I-2. As can be seen, the change in semi-major axis decreases rapidly as the inclination of the sun line to the orbital plane increases, and virtually no control can be achieved for high sun line inclinations.

It is interesting to note that the curves level off at the point where ψ_A is equal to i_s. At this point, the oscillation of the sail angle is no longer large enough to enable the side facing the velocity vector to intercept the solar rays during the position of the orbit where the sail plane is tilted out of the plane of the orbit in the direction of the sun.

The sail coating configuration used for all the Phillips studies is shown in figure I-2. Since the Phillips concept does not depend on different forces due to different surface coatings, the reflectivity of the surface was chosen high to give a maximum force.

As a basis of comparison, similar curves are shown in figure I-3 for two different coating configurations employing the yaw-stabilized technique. The

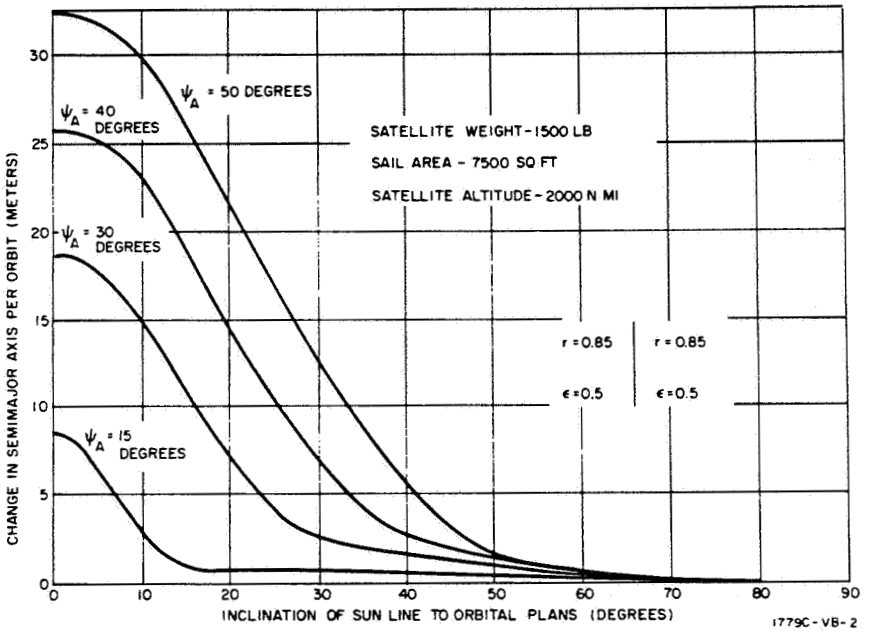

Figure I-2. Basic Phillips Technique

coating configuration chosen for number one is the combination of the achievable characteristics as given by the Goodyear Aerospace Division which produce maximum mobility. As can be seen, configuration two produces somewhat less mobility.

In general, the yaw-stabilized method is seen to produce more mobility than even the 50-degree oscillation on the basic Phillips method. The response of the yaw-stabilized method is seen to be much better at higher sun line inclinations. For these reasons and also because the basic Phillips technique requires continuous active attitude control, the basic Phillips technique is believed to be of no practical value.

Rotational Phillips Concept

In the rotational Phillips concept, a constant rotation about the radius vector of twice the orbital period is imposed on the satellite. Thus, at the

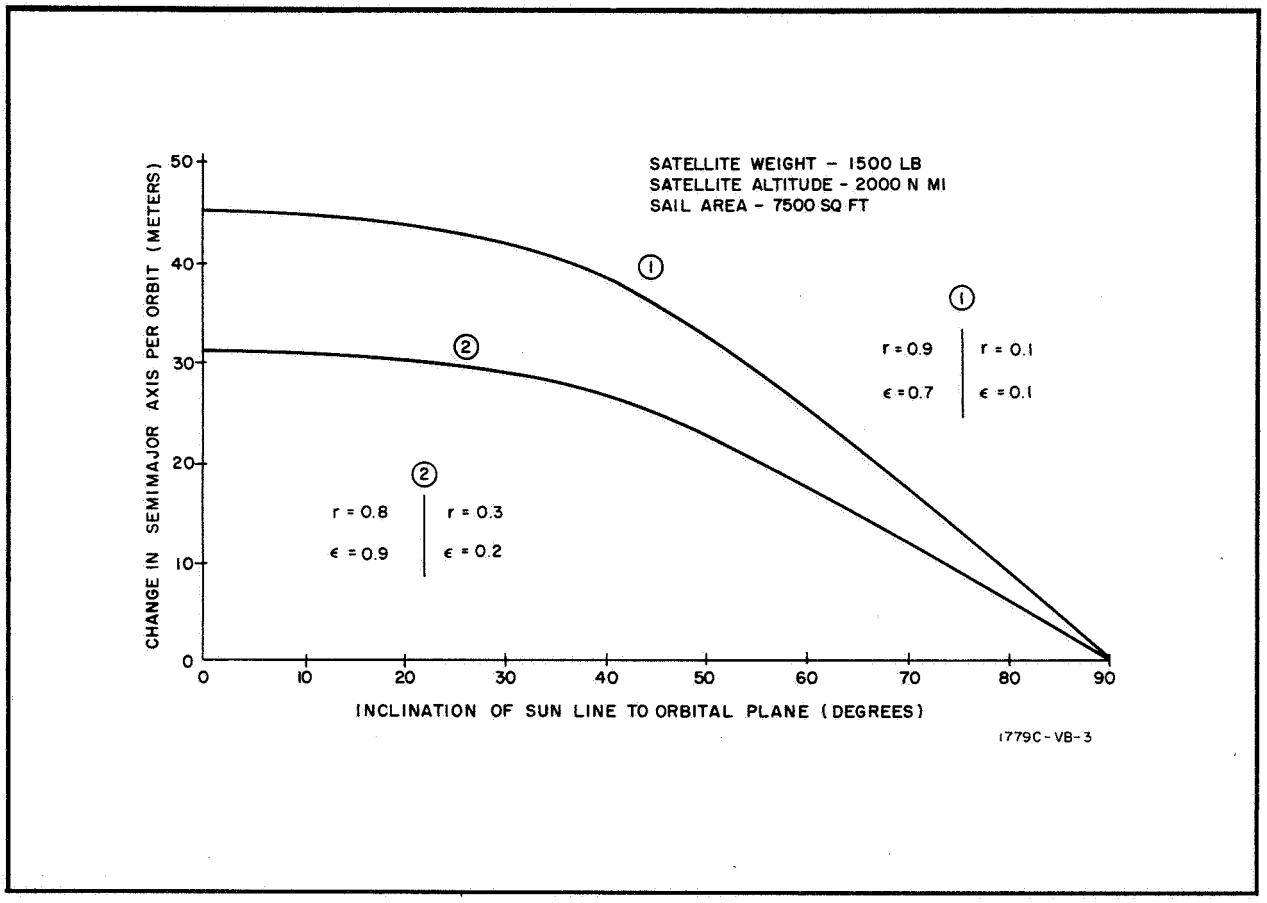

Figure I-3. Yaw-Stabilized Technique

two points in the orbit at 90 degrees to the projected sun line vector, the plane of the sail will be alternately normal and parallel to the velocity vector. For this condition, the angle between the plane of the sail and the velocity vector for the two modes of operation is defined by:

$$\psi_I = \pi\left[\frac{t\,(u) - t\,(u_s + \frac{\pi}{2})}{P}\right]$$

$$\psi_D = \pi\,\frac{1}{2} + \frac{t\,(u) - t\,(u_s + \frac{\pi}{2})}{P}$$

The results of several computer runs showing the change in semi-major axis per orbit as a function of the inclination of the sun line to the plane of the orbit are given in figure I-4. A positive sun line inclination in this case is defined as a clockwise motion of the satellite about the sun line. As can

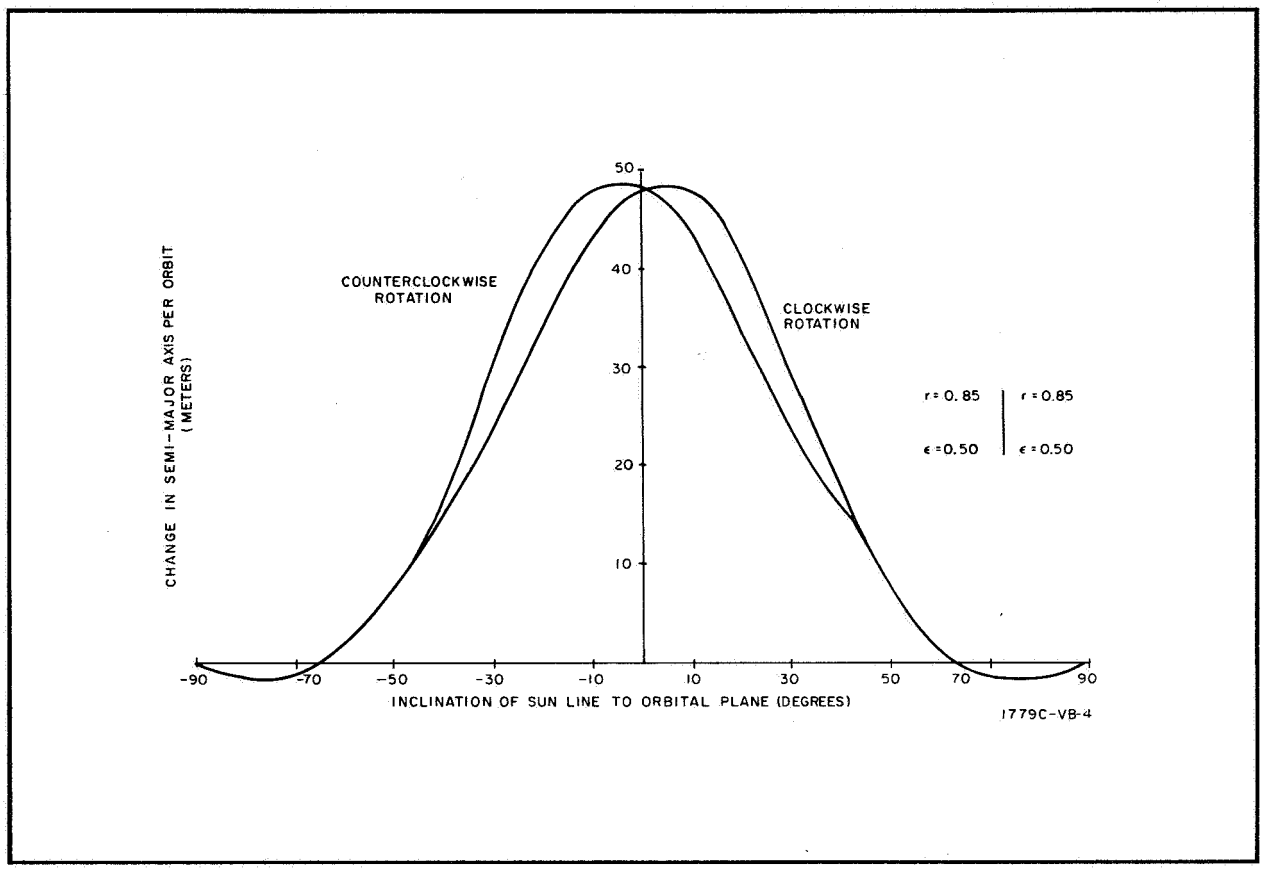

Figure I-4. Rotational Phillips Technique

be seen, the curves are somewhat offset for clockwise and counterclockwise rotations of the satellite about the radius vector. This effect is due to the fact that for the two opposite rotations, the earth's shadow occults different relative regions of the derivative curve, thus producing a net difference in the integral. As can be seen, the two delta a curves merge at approximately 40-degree sun line inclination where the orbit emerges completely from the earth's shadow.

While the mobility for this technique is slightly higher than the maximum yaw-stabilized case shown in figure I-3, when the sun line is near the plane of the orbit, it is seen to decrease rapidly with increasing sun line inclination. This technique again requires continuous active attitude control. Thus, since the yaw-stabilized technique produces a better response over the entire range of operation, the rotational Phillips technique is not considered to be practical.

Solar-Oriented Phillips Technique

In an effort to obtain better orbit position control capability at the higher sun line inclinations, a third technique making use of the Phillips concept has been studied. It can be shown that when the sun line is perpendicular to the orbital plane, a maximum amount of mobility can be obtained by maintaining the sail angle at 45 degrees to the velocity vector. Furthermore, for these conditions, an oscillatory motion of the sail such as used in the Phillips technique will reduce the amount of mobility.

However, when the sun line is in the plane of the orbit, it can be shown that the basic Phillips concept of orbit position control will produce a large amount of mobility and that a shift in the mean sail angle from zero would only result in a reduction of the mobility. In an effort to combine these two useful effects, a system has been implemented whereby the basic Phillips concept is used when the sun line is in the plane of the orbit and, as the sun line inclination increases, the mean sail angle is adjusted to equal half the sun line inclination and the magnitude of the oscillation is damped to 0 at a 90-degree sun line inclination. For these conditions, the angle between the plane of the sail and the velocity vector for the two modes of operation is defined by:

$$\psi_I = \frac{\psi_A\,(\pi - 2|i_s|)}{\pi} \cos\left\{\frac{\left[t\,(u) - t\,(u_s + \frac{\pi}{2})\right]}{P}\right\} + \frac{i_s}{2}$$

$$\psi_D = \frac{\psi_A\,(\pi - 2|i_s|)}{\pi} \sin\left\{\frac{\left[t\,(u) - t\,(u_s + \frac{\pi}{2})\right]}{P}\right\} + \frac{i_s}{2}$$

This technique of control has also been implemented in the simplified mobility program, and the results of several runs are shown in figure I-5. The sail tilting clockwise cases are obtained by changing the sign of the $i_s/2$ term in the relationships ψ_I and ψ_D.

As can be seen from figure I-5, this scheme does not allow control of the satellite by choosing two modes of operation 180 degrees apart since both

modes give the same value of semi-major axis change at the higher values of sun line inclination. A much better method of control would allow the two modes of operation to follow the two nonzero crossing curves of figure I-5. This would require that the two modes be adjusted so that their mean sail angles to the velocity vector would be $i_s/2$ and $\pi - i_s/2$.

This system is seen to produce very much better control at the higher sun line inclinations, and in particular producing even better control at 90-degree than at 0-degree sun line inclination. However, it can be shown that combining the yaw-stabilized technique with the solar orientation technique will produce even greater control at the lower sun line inclinations. Hence, for this reason, and again because this system requires a continuous active attitude control system, it is not considered to be practical for obtaining orbit position control.

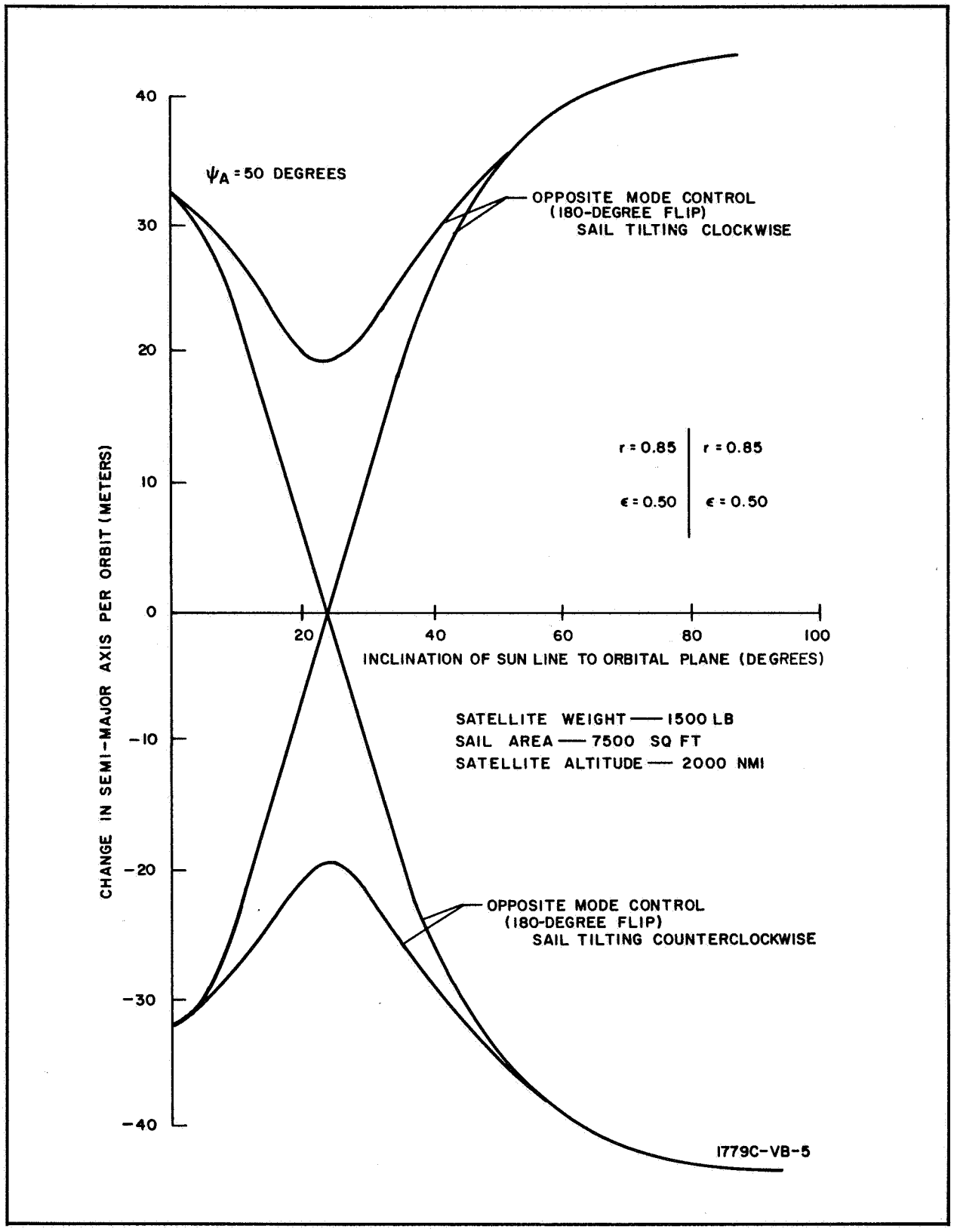

Figure I-5. Solar-Oriented Phillips Technique

APPENDIX II

MAGNETIC TORQUE COIL SYSTEM

One concept of satellite attitude control utilizes magnetic coils which can be reacted with the earth's magnetic field to produce the required torques. In order to provide the desired control, three orthogonal torque coils are necessary. The lenticular satellite geometry lends itself to the use of triangular torque coils for the roll and pitch axes and a circular coil for the yaw axis. The forces applied to the satellite structure by the use of these coils are derived in order to determine the structural requirements. In addition, the parameters of torque coil design are examined to obtain an optimum combination of torque coil and torque coil power supply which minimizes total system weight.

Coil Force Equations

In order to provide a basis for the calculation of satellite structural requirements, the forces produced by three orthogonal magnetic torque coils have been defined in terms of a generalized coil geometry, coil current, and magnetic field vector.

The coil configuration considered in this study is shown in figure II-1 consisting of two triangular coils and one circular coil. To facilitate the description of coil forces, the coil-oriented coordinate system X-Y-Z has been established. An arbitrary field vector, $\overline{B}$, is specified by the angle ϕ which it makes with the X-Y plane and the angle θ made with Y-Z plane. Figure II-2 illustrates the general $\overline{B}$ vector, and gives the expression for B_x, B_y, and B_z, the components of B parallel to the X, Y, and Z axis, respectively. The forces on each coil produced by the components B_x, B_y, and B_z are given in figures II-3 through II-11 for coil currents I_A, I_B, and I_C corresponding to the respective coils A, B, and C. Absolute values of force

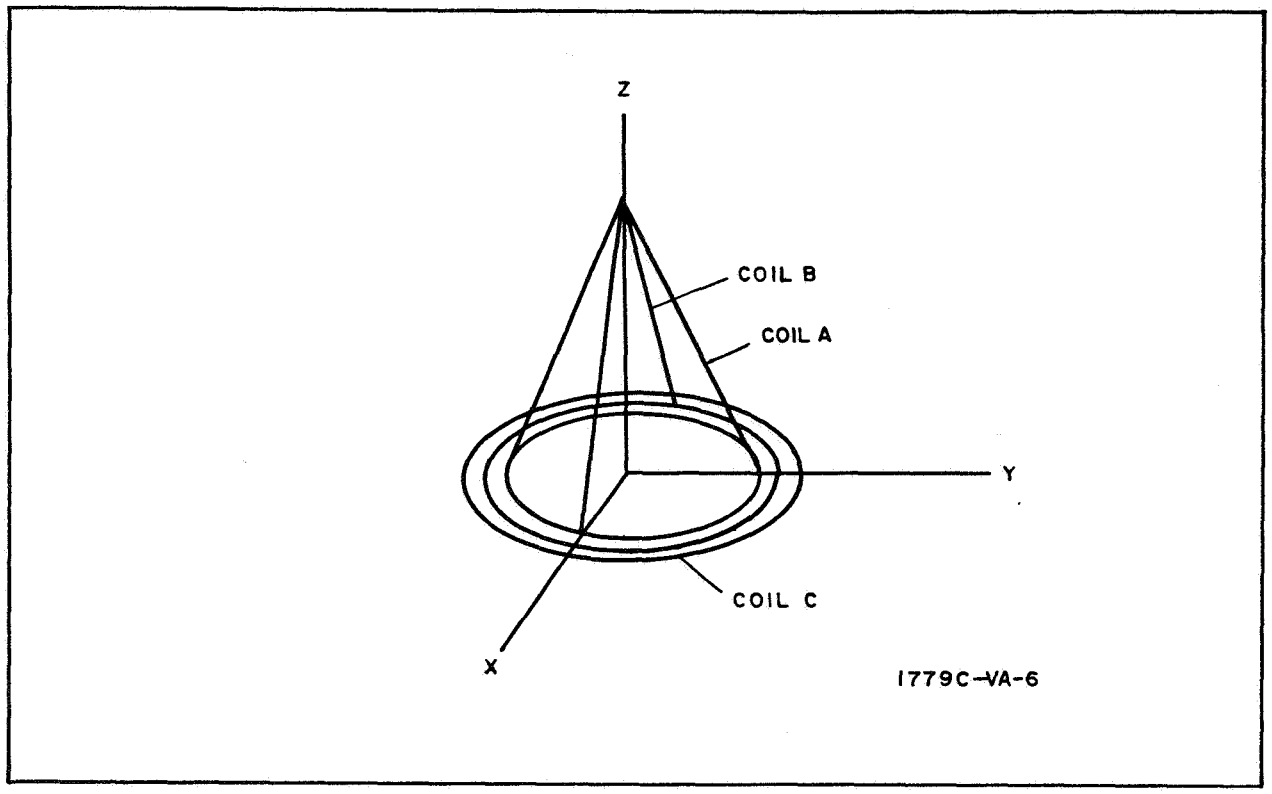

Figure II-1. Schematic Coil Configuration

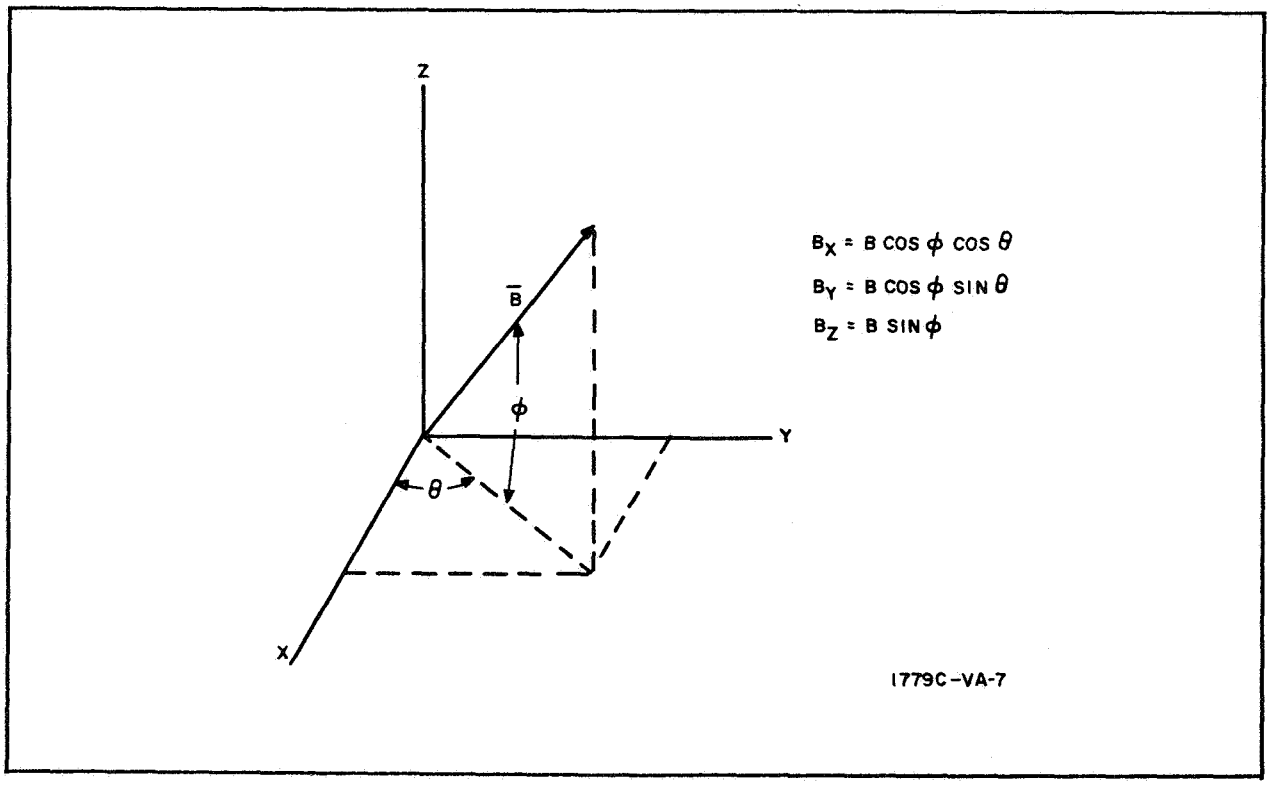

Figure II-2. Generalized B Vector

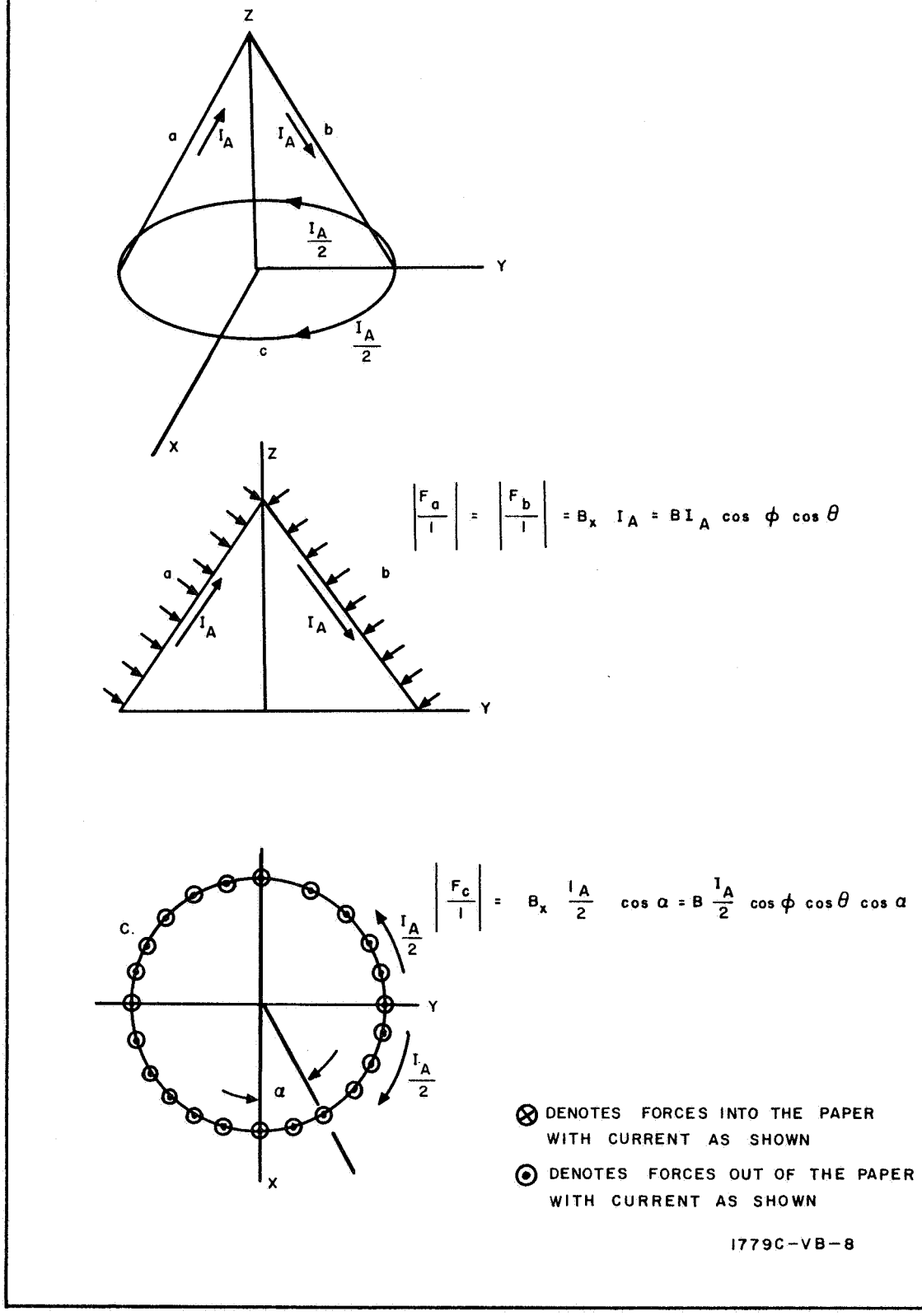

Figure II-3. Forces in Coil A Produced by B_x

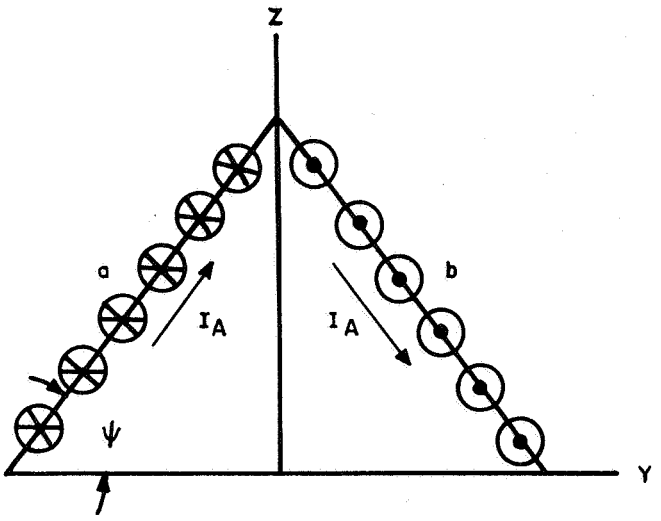

$$\left|\frac{F_a}{l}\right| = \left|\frac{F_b}{l}\right| = B_Y I_A \sin\psi = B I_A \cos\theta \sin\theta \sin\psi$$

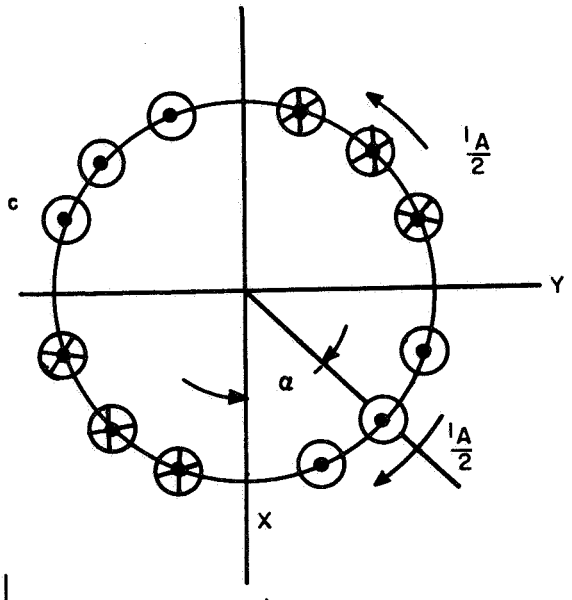

$$\left|\frac{F_C}{l}\right| = B_Y \frac{I_A}{2} \sin\alpha = B \frac{I_A}{2} \cos\phi \sin\theta \sin\alpha$$

1779C-VB-9

Figure II-4. Forces in Coil A Produced by B_y

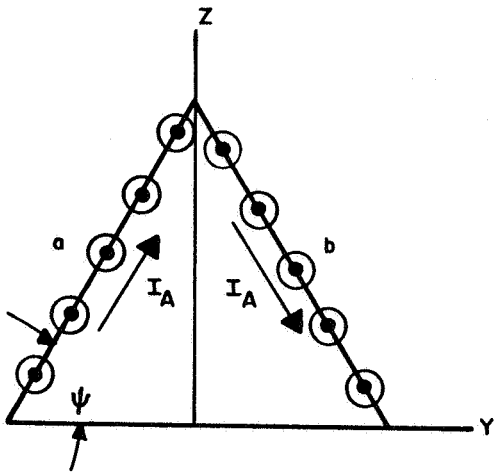

$$\left|\frac{F_A}{l}\right| = \left|\frac{F_b}{l}\right|$$

$$= B_Z I_A \cos \psi$$

$$= B I_A \sin \phi \cos \psi$$

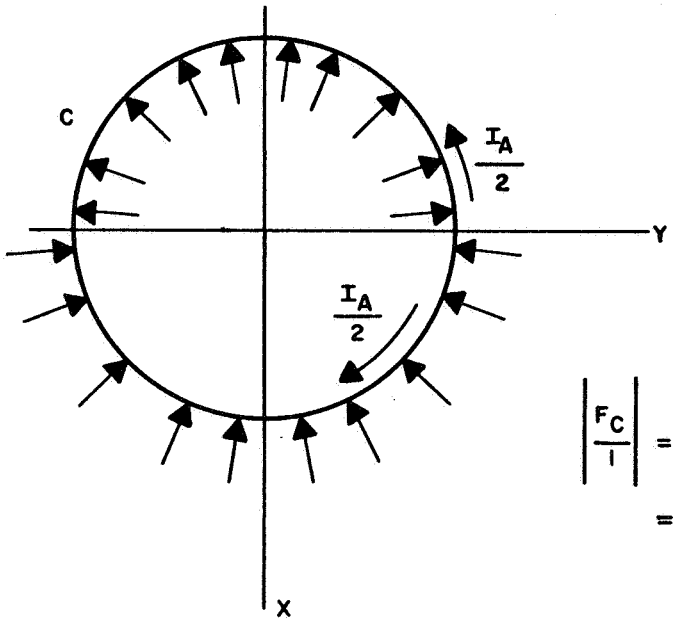

$$\left|\frac{F_C}{l}\right| = B_Z \frac{I_A}{2}$$

$$= B \sin \phi \frac{I_A}{2}$$

1779C-VB-10

Figure II-5. Forces in Coil A Produced by B_z

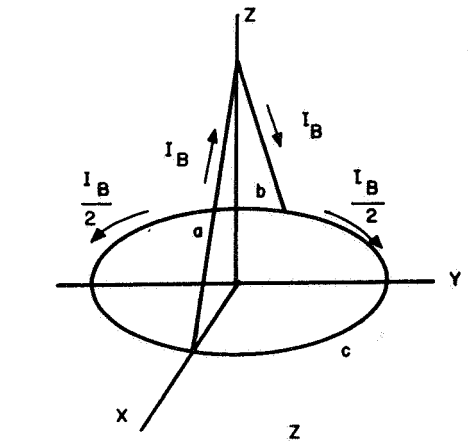

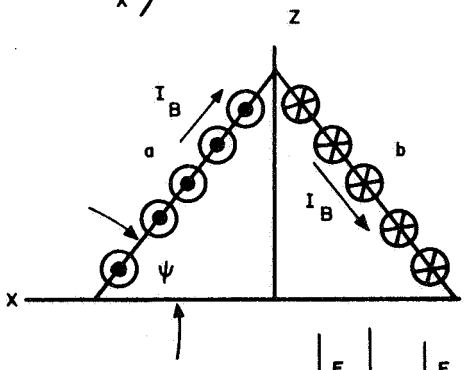

$$\left|\frac{F_a}{l}\right| = \left|\frac{F_b}{l}\right|$$

$$= B_X I_B \sin\psi$$

$$= B I_B \cos\phi \cos\theta \sin\psi$$

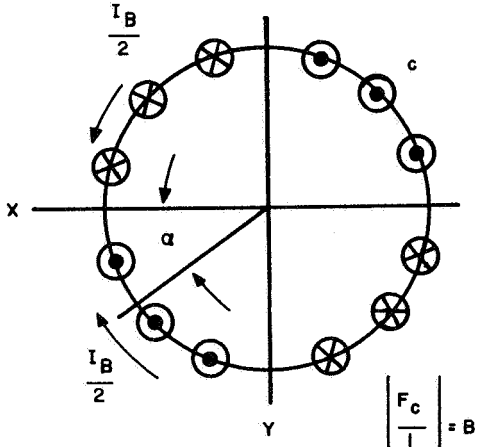

$$\left|\frac{F_c}{l}\right| = B_X \frac{I_B}{2} \cos\alpha$$

$$= B \frac{I_B}{2} \cos\phi \cos\theta \cos\alpha$$

1779C-VB-11

Figure II-6. Forces in Coil B Produced by B_x

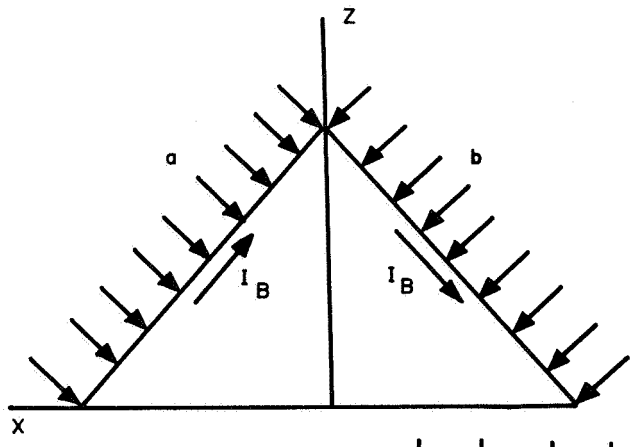

$$\left|\frac{F_a}{l}\right| = \left|\frac{F_b}{l}\right|$$

$$= B_y I_B$$

$$= B I_B \cos\phi \sin\theta$$

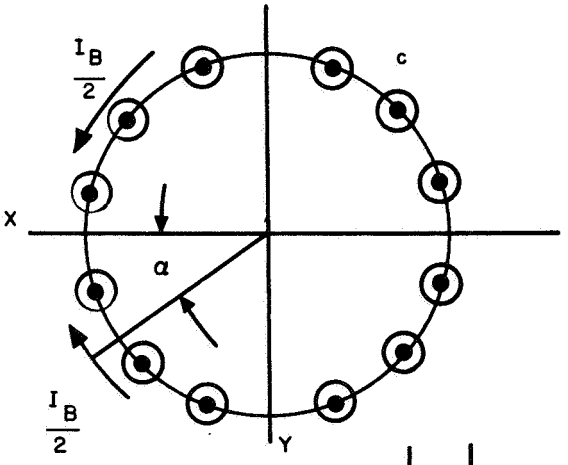

$$\left|\frac{F_c}{l}\right| = B_y \frac{I_B}{2} \sin\alpha$$

$$= B \frac{I_B}{2} \cos\phi \sin\theta \sin\alpha$$

1779C-VB-12

Figure II-7. Forces in Coil B Produced by B_y

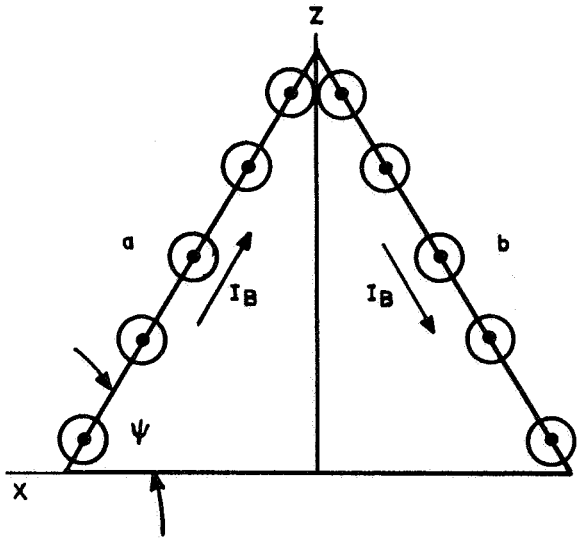

$$\left|\frac{F_a}{l}\right| = \left|\frac{F_B}{l}\right|$$

$$= B_Z \, I_B \cos \psi$$

$$= B I_B \sin \phi \cos \psi$$

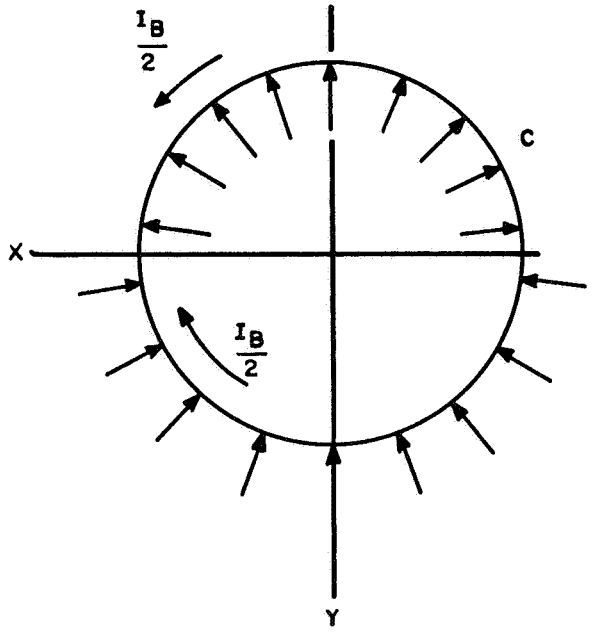

$$\left|\frac{F_C}{l}\right| = B_Z \frac{I_B}{2}$$

$$= B \frac{I_B}{2} \sin \phi$$

1779C-VB-13

Figure II-8. Forces in Coil B Produced by B_z

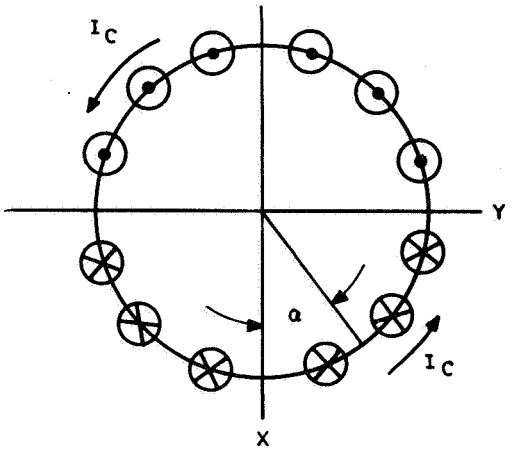

$$\left|\frac{F}{l}\right| = B_X I_C \cos\alpha$$
$$= B\, I_C \cos\phi \cos\theta \cos\alpha$$

1779C-VA-14

Figure II-9. Forces in Coil C Produced by B_x

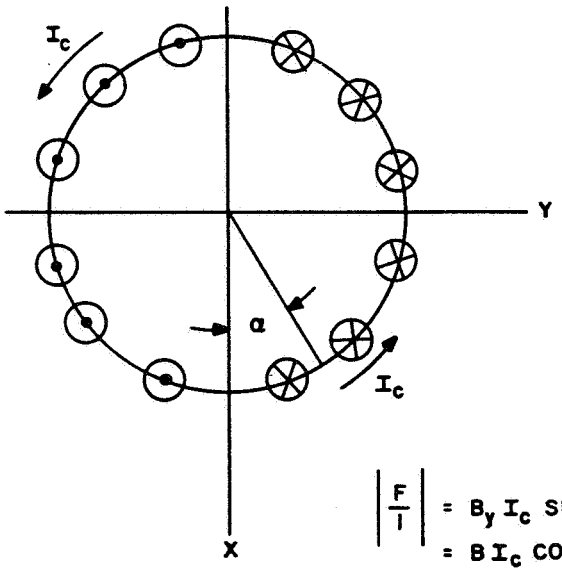

$$\left|\frac{F}{l}\right| = B_y I_c \sin\alpha$$
$$= B I_c \cos\phi \sin\theta \sin\alpha$$

1779C-VA-15

Figure II-10. Forces in Coil C Produced by B_y

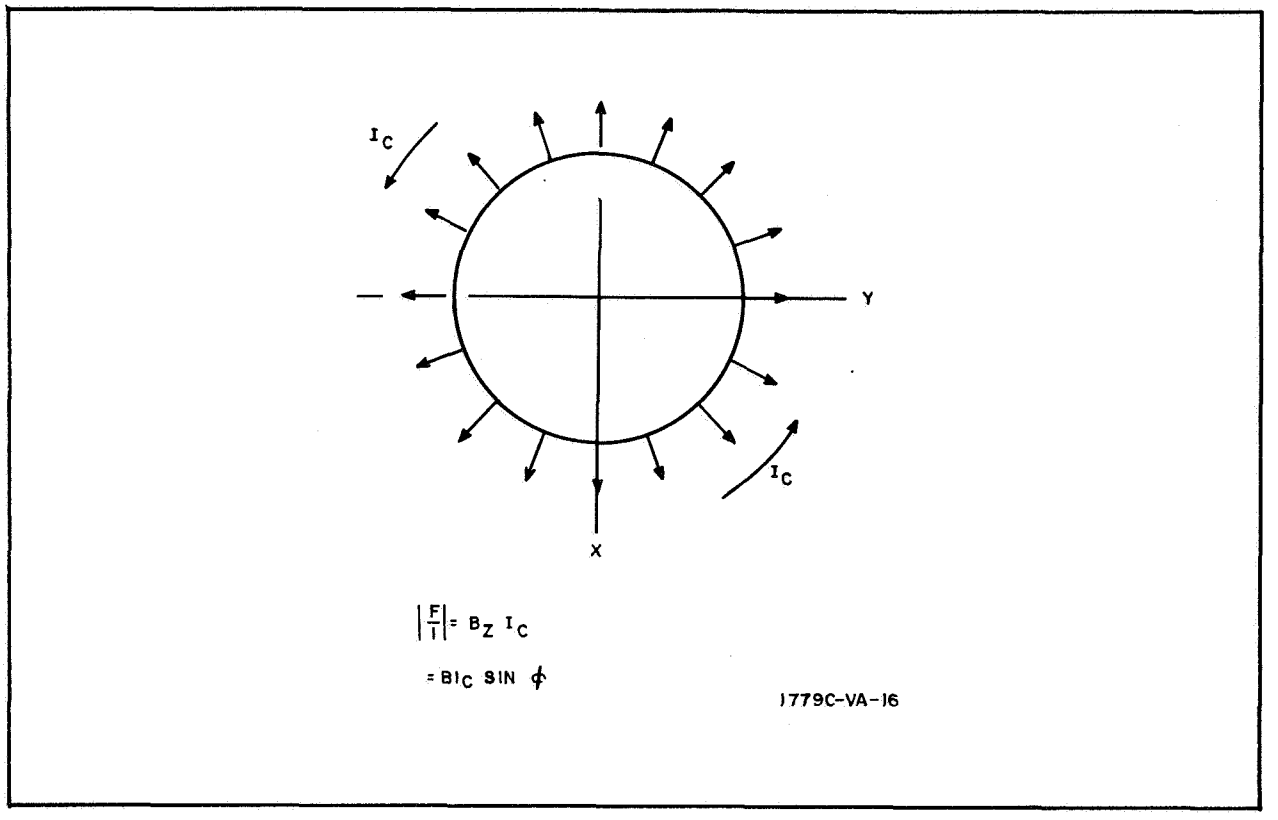

Figure II-11. Forces in Coil C Produced by B_z

are given in the equations accompanying these figures and the direction of the force vector indicated in the diagram. Reversal of either the magnetic field component or the coil current will of course reverse the direction of the resultant forces.

The total resultant force in any section of the coil structure may be found by superimposing the forces caused by the various components of the magnetic field on each coil. In order to perform the above calculations, both the maximum value of current in each coil and the variation of coil current with satellite orientation must be known. Maximum current requirements as well as current variation are dependent upon the type of control system finally selected. However, to allow an investigation of the structural problems arising from the application of magnetic torques, typical coil currents and operating characteristics are presented based on best estimates of control system requirements.

The torque required per gauss of magnetic field is assumed to be 0.8 ft-lb per gauss for each coil. This torque requirement is used to determine the maximum coil current. The equation relating torque to current is:

$T = \gamma BNIA$

where

T = torque, ft-lb

B = magnetic field, gauss

NI = total coil current, amperes

A = enclosed area of coil, ft^2

$\gamma = 0.685 \times 10^{-5}$ lb amp^{-1} ft^{-1} per gauss

Using an area of 55,990 ft^2 for a 267-ft diameter circular coil and 47,530 ft^2 for a triangular coil 356 ft high and with a 267-ft base the currents required to produce 0.8 ft-lb per gauss are:

Circular coil, $I = 2.09$ amps

$= I_c$ (max)

Triangular coil, $I = 2.46$ amps

$= I_A$ (max)

$= I_B$ (max)

It is further assumed that the current in a particular coil can equal this maximum value only when the magnetic field vector is parallel to the coil, and that the current decreases sinusoidally to zero as the coil rotates to a position perpendicular to the field. This programming of the coil currents is performed by the satellite control electronics through a comparison of the earth's magnetic field vector with an error signal generated by the satellite sensor system. The current is computed by the control system as the cross-product of the error signal and the magnetic field vector. Thus, the maximum current vector (defined as the resultant vector formed by components I_A, I_B, and I_C) can occur whenever the error vector lies in a plane orthogonal to the B field. The forces in a particular section of coil can be calculated by finding the position of B and I producing maximum force, with the assumption that the error vector can always lie in a direction orthogonal to B and I.

Several combinations of B and I which appear to result in maximum forces under present control concepts are considered in the following examples.

Case A - Maximum Normal Force - Triangular Coil Leg. - This situation can arise when the $\bar{B}$ vector lies in the plane of a coil and is perpendicular to one leg of the coil. The error vector is assumed to be orthogonal to the coil current and $\bar{B}$ such that maximum current is required. Stating this condition in terms of coil A:

$\bar{B}$ is in the Y-Z plane, perpendicular to side a; therefore, $B_x = 0$, $B_y = B \cos (90 - \psi) \sin 90$, and $B_z = B \sin (90 - \psi)$. $I_A = I_A$ max

$$\left|\frac{F}{l} a\right| = B_y I_A \sin \psi + B_z I_A \cos \psi$$

$$= BI_A (\max) \cos (90 - \psi) \sin \psi + BI_A (\max) \sin (90 - \psi) \cos \psi$$

$$= BI_A (\max) \sin^2 \psi + BI_A (\max) \cos^2 \psi$$

$$\left|\frac{F}{l} a\right| = BI_A (\max)$$

Substituting for B = 0.15 gauss and I_A (max) = 2.46 amps:

$$\left|\frac{F}{l} a\right| = 0.15 \text{ gauss} \times \frac{0.685 \times 10^{-5} \text{ lb}}{\text{amp-ft-gauss}} \times 2.46 \text{ amp} = 1.68 \times 10^{-6} \frac{\text{lb}}{\text{ft}}$$

Case B - Maximum Inward Collapsing Load - Triangular Coil Leg. - The inward collapsing loads on a coil are caused by the component of $\bar{B}$ which is perpendicular to the plane of the coil. Considering coil A, the inward collapsing force is proportional to I_A and B_X and is given by the equation:

$$\left|\frac{F_a}{l}\right| = B_X I_A$$

$$= BI_A \cos \phi \cos \theta$$

For maximum force, $\bar{B}$ lies in the X-Y plane, thus $\cos \phi = 1$. Current in coil A varies as $\sin \theta$; thus, the equation may be written as:

$$\left|\frac{F_a}{l}\right| = BI_A (\max) \sin \theta \cos \theta$$

Evaluated at it's maximum where $\theta = 45°$, it becomes:

$$\left|\frac{F_a}{l}\right| = BI_A \text{ (max) } \sin 45 \cos 45$$

$$\left|\frac{F_a}{l}\right| = \frac{1}{2} BI_A \text{ (max)} = 0.84 \times 10^{-6} \frac{\text{lb}}{\text{ft}}$$

Case C - Maximum Collapsing Force in a Quadrant of the Rim. - Maximum collapsing force in the rim is dependent upon the effects of all three coils operating simultaneously. Examination of figures II-5, II-8, and II-11 reveals that a quadrant exists in which the tensile or outward loads due to all three coil currents are additive. By reversal of either the $\overline{B}$ vector or coil current, a quadrant exists having inward force components caused by all three coils. An equation combining the coil forces may be written as:

$$\left|\frac{F_c}{l}\right| = B_z \left(\frac{I_A}{2} + \frac{I_B}{2} + I_C\right)$$

$$= B \sin \phi \left(\frac{I_A}{2} + \frac{I_B}{2} + I_C\right)$$

In maximizing this equation, the direction of $\overline{B}$ and $\overline{I}$, the composite coil current vector must be determined. Since the composite $\overline{I}$ vector must be perpendicular to the $\overline{B}$ vector, expressions for B_z, I_A, I_B, and I_C may be written in terms of ϕ and θ, and the resulting force equation differentiated obtaining the following values for maximum force:

$$B_z = B \sin \phi$$
$$= B \sin 62.5°$$
$$I_A = \cos \theta \sin \phi \, I_A \text{ (max)}$$
$$= \cos 45° \sin 62.5° \, I_A \text{ (max)}$$
$$I_B = \sin \theta \sin \phi \, I_B \text{ (max)}$$
$$= \sin 45° \sin 62.5° \, I_B \text{ (max)}$$
$$I_C = \cos \phi \, I_C \text{ (max)}$$
$$= \cos 62.5° \, I_C \text{ (max)}$$

Substituting into the force equation:

$$B_z = 0.15 \text{ gauss} \times \frac{0.685 \times 10^{-5} \text{ lb}}{\text{amp - ft - gauss}} \times \sin 62.5°$$

$$= 9.12 \times 10^{-7} \frac{\text{lb}}{\text{amp - ft}}$$

$$I_B = I_A$$

$$= \sin 45° \sin 62.5° \times 2.46 \text{ amps}$$

$$= 1.54 \text{ amps}$$

$$I_C = \cos 62.5° \times 2.09 \text{ amps}$$

$$= 0.965 \text{ amps}$$

$$\left|\frac{F_c}{l}\right| = B_z \left(\frac{I_A}{2} + \frac{I_B}{2} + I_C\right)$$

$$= \left|\frac{F_c}{l}\right|$$

$$= 2.29 \times 10^{-6} \frac{\text{lb}}{\text{ft}}$$

Optimum Coil Design

With respect to the design of a magnetic torquing system, it can be seen that a weight tradeoff exists between the torque coils and their solar cell power supplies. The power supply requirements may be reduced by increasing coil area, and, conversely, a reduction in coil area, increasing the coil resistance, must be compensated for by the addition of solar cells. In the following derivation, it will be shown that the optimum combination of coil and power supply is achieved when their weights are equal, and that the power requirement is a function of the coil perimeter to area ratio.

The torque produced by a single coil can be expressed as:

$$T = NIAB \qquad \text{(II-1)}$$

where

N = number of turns

I = coil current

A = area enclosed by coil

B = the earth's magnetic field

The coil resistance, R, is a function of it's resistivity, r, cross-sectional area, a, and perimeter, p, such that:

$$R = \frac{Npr}{a} \tag{II-2}$$

The power dissipated in the coil would then be

$$P = I^2R \tag{II-3}$$

$$= \frac{NI^2pr}{a}$$

Power supply weight, W_{ps}, can be expressed as

$$W_{ps} = KP \tag{II-4}$$

$$= \frac{KNI^2pr}{a}$$

where K is the solar cell power supply factor in pounds per watt.

The weight of the torque coil, W_c, can be written as,

$$W_c = Nadp \tag{II-5}$$

where d is the coil density.

The total weight of the coil-power supply system is

$$W_t = \frac{KNI^2pr}{a} + Nadp \tag{II-6}$$

Solving equation II-1 for N and substituting into the above equation yields

$$W_t = \left(\frac{T}{B}\right)\left(\frac{p}{A}\right)\left(\frac{KrI}{a} + \frac{ad}{I}\right) \tag{II-7}$$

If the above equation is differentiated with respect to I and set equal to 0, the optimum total weight of the system is obtained:

$$W_{tmin} = 2\left(\frac{T}{B}\right)\left(\frac{p}{A}\right)\sqrt{Krd} \tag{II-8}$$

The power dissipation for optimum coil design is:

$$P = \left(\frac{T}{B}\right) \left(\frac{p}{A}\right) \sqrt{\frac{rd}{K}} \qquad \text{(II-9)}$$

So that the required power supply weight is:

$$W_{ps} = KP \qquad \text{(II-10)}$$

$$= \left(\frac{T}{B}\right) \left(\frac{p}{A}\right) \sqrt{Krd}$$

$$= \frac{1}{2} W_{tmin}$$

Thus, for minimum total weight, the coil weight equals the torque system power supply weight:

$$W_{ps} = W_c \qquad \text{(II-11)}$$

$$= \left(\frac{T}{B}\right) \left(\frac{p}{A}\right) \sqrt{Krd}$$

As previously mentioned in the coil force equation section, the estimated value of (T/B) about each axis of the satellite is 0.8 ft-lb per gauss. The perimeter-to-area ratio for triangular coils with a height of 356.5 feet and a base corresponding to the circumference of a 267-foot diameter circle is 0.025. For the circular coil, p/A = 4/D or 0.015. The value of K, pounds per watt furnished by the solar cell array is a function of orbit altitude and inclination. The product of resistivity and density is a function of the specific materials from which the coils are fabricated and will be considered to be aluminum conductors with mylar insulation such that $rd = 31.0 \times 10^{-6}$ lb-ohm-ft^{-2}.

$$W_c = \left(0.8 \frac{\text{ft-lb}}{\text{gauss}} \times 1.46 \times 10^5 \frac{\text{amp-ft-gauss}}{\text{lb}}\right) \times \frac{P}{A} \text{ ft}^{-1}$$

$$\left(K \frac{\text{lb}}{\text{amp}^2\text{-ohm}} \times 31.0 \times 10^{-6} \frac{\text{lb-ohm}}{\text{ft}^2}\right)^{1/2}$$

$$W_c = \left(1.17 \times 10^5 \frac{p}{A} \text{ ft-amp}\right)\left(5.55 \times 10^{-3}\sqrt{K} \frac{\text{lb}}{\text{amp-ft}}\right)$$

$$W_c = 650 \frac{p}{A}\sqrt{K} \text{ lb} \qquad \text{(II-12)}$$

$$= W_{ps}$$

The weights of coil and power supply as a function of inclination are as follows:

- Circular Coil $p/A = 0.015 \text{ ft}^{-1}$

Inclination (degrees)	Coil Weight (lb)	Power Supply Weight (lb)
0	16.5	16.5
30	15.0	15.0
60	13.5	13.5
90	13.0	13.0

- Triangular Coil $p/A = 0.025 \text{ ft}^{-1}$

Inclination (degrees)	Coil Weight (lb)	Power Supply Weight (lb)
0	27.6	27.6
30	26.2	26.2
60	22.8	22.8
90	22.0	22.0

Total Weight

The total coil weight equals the circular coil weight plus twice the triangular coil weight. Since the control system requires a maximum torquing power which can never exceed twice the power of the largest coil, the power supply for the smallest coil may be omitted from the torque system weight.

Inclination (degrees)	Total Coil Weight (lb)	Total Power Supply Weight (lb)
0	71.5	55.2
30	67.4	52.4
60	59.1	45.6
90	57.0	44.0

Magnetic Control System Electronics

The magnetic torque system requires control electronics consisting of the following major components:

- Command receiver and decoder
- Memory and associated driver circuits
- Transmitter
- Logic circuitry
- Power amplifiers
- Sensors and magnetometers

On the basis of the work performed during a feasibility study of orbit position control techniques, the following electronics requirements have been estimated:

Volume	1.5 cu ft
Unshielded electronics weight	55 lb
Radiation shielding	20 lb
Electronics power	43 watts

APPENDIX III
RADIOISOTOPE POWER SUPPLIES

Orbit Position Control

Power supply studies for the satellite revealed that the shielding and initial excess capacity requirements of solar cell power supplies result in a significant weight penalty for a 5-year life at orbit altitudes corresponding to the proton region of the Van Allen zone. In an effort to reduce power supply weight, the properties of several radioisotope power generators have been investigated. The two basic types of radioisotope power conversion currently considered for space application are: direct thermoelectric conversion, in which heat is converted to electrical energy by an assembly of thermocouples, and Rankine or Brayton cycle dynamic generation. For power requirements of less than 1 or 2 kilowatts, the direct thermoelectric conversion systems are most desirable from the standpoint of cost, reliability, and weight. The advantages of a radioisotope-thermoelectric generator (RTG) for this particular satellite application include long life, high reliability, low weight requirements, unaffected by space radiation, minimal volume requirements, and unaffected by day-night orbits. Despite these apparently overwhelming advantages, the problems of fuel availability, cost, shielding requirements, and launch safety must be considered to realistically evaluate the practicality of an RTG.

By comparison of the isotope half-life, specific power, and availability, the field of candidate isotopes for use in a space application can presently be narrowed down to four elements: Plutonium - 238, Curium - 244, Strontium - 90, and Promethium - 147. A comparison of the properties of these isotopes is given in table III-1. The requirements of a 50-watt power supply with a 5-year life are given in table III- 2 for the four candidate isotopes. It can be

TABLE III-1

CHARACTERISTICS OF RADIOISOTOPES

	Strontium -90	Cesium -137	Promethium -147	Thorium -228	Uranium -232	Plutonium -238	Curium -244
Specific Power, watts/gr	0.95	0.42	0.33	170	4.4	0.56	2.8
Half Life, years	28	30	2.7	1.9	74	89	18.4
Compound Form	$SrTiO_3$	Glass	Pm_2O_3	ThO_2	UO_2	PuO_2	CmO_2
Compound Density g/cc	4.6	3.2	6.6	9	10	10	11.75
Power Density watts/cc	1.05	0.215	1.8	1270	33	3.9	27
Volume for 2 KW Heat: cc	1840	9300	1120	1.58	61	513	74
Decay Product	Beta	Beta-Gamma	Beta	Beta	Beta	Alpha	Alpha Neutron
Shielding Req	Heavy	Heavy	Minor	Heavy	Heavy	Minor	Heavy
Est. Cost, $/watt (thermal)	19	21	91	40	350	894	357
Production Capability (thermal KW)							
1963	19	5	0.01	-	-	1.5	-
1967	67	48	11.0	-	-	11.0	41
1970	157	110	25	-	-	25.8	129
1980	693	458	111	-	-	73.0	134

TABLE III-2

COMPARISON OF SATELLITE POWER SUPPLY CHARACTERISTICS

	Pm-147	Pu-238	Cm-244	Sr-90	Solar Cells
Fuel Wt (lb)	28.5	5.8	1.1	10.6	180 - 122
Generator Wt	3.1	3.1	3.1	3.1	-
Radiator Wt	20.5	6.8	7.7	7.4	-
Shielding Wt*	12.1	3.5	16.0	16.6	-
Total Wt (lb)	64.2	19.2	27.9	37.6	180 - 122
Fuel Cost	$271,000	$915,000	$511,000	$21,000	$700,000 - 500,000

* Assumes the use of a shadow shield sufficient to reduce the integrated 5-year gamma and fast neutron dosage at the electronics packages to 10^7 and 10^4 rad, respectively. Shield weight does not include the prelaunch biological shielding required by the curium -244 and Sr-90 systems.

seen in table III-2 that the fuel weight varies greatly between isotopes due to the variation in power density and isotope half-life. Shielding required to protect satellite electronic equipment also varies significantly due to the type and energy of the emitted radiation. Strontium -90, a high energy β-emitter, and Curium -244 with its high neutron flux, require heavier shielding than do the low energy β-emitter Promethium -147 or the α-emitter Pu-238. The cost and availability of isotopes are closely related and are of course subject to actual demand for the isotope. Since Sr-90 and Pm-147 are fission products and exist in relatively large quantities in waste from nuclear reactor fuel processing, their availability and therefore cost, are very favorable. The remaining two isotopes Cm-244 and Pu-238 are produced by neutron irradiation of special target materials and thus are higher in cost and more limited in availability.

The potential danger to the earth's population must always be included in the consideration of a nuclear power supply. Assuming a successful launch and orbit injection, no significant radiation hazard will result if the orbital lifetime is at least five times the isotope half-life. If, however, the vehicle

should fail to attain orbit or if the orbit should be short lived, the method used to contain the radioactive fuel becomes extremely important. Fuel capsules must be designed to survive launch-pad accidents, withstand the forces of explosion and high speed impact, and burn up and disintegrate into minute particles upon atmospheric reentry from a short-lived orbit. Tests conducted by producers of RTG units in cooperation with the US Air Force and the Atomic Energy Commission demonstrated the feasibility of a fuel capsule meeting these requirements. Despite this fact, the political impact of launching certain of the biologically hazardous isotopes must be fully considered.

In summary, table III-2 shows that the use of an RTG would substantially reduce the weight of the required 50-watt power supply at 2000 nautical miles. It should be noted that while the weight saving will decrease for lower radiation orbits, the effect of increasing satellite life requirements beyond 5 years would be to greatly increase the desirability of a radioisotope power supply. The cost comparison based on present estimates of isotope availability shows that an RTG system fission products such as Pm-147 or Sr-90 could greatly reduce the power supply costs as compared to an equivalent solar cell system.

Bibliography

1. Davis, H. L., "Nucleonics," Isotopes Costs and Availability, p. 63, March 1963.
2. "Radiation Characteristics and Shielding Requirements of Isotopic Power Sources for Space Missions," ORNL-TM-591 (Rev.).
3. "Radioisotopic Heat Sources," Atomic Energy Commission Research and Development Report, HW-76323, Rev. 1
4. "Radioisotopic Heat Sources, Supplementary Data," Atomic Energy Commission Research and Development Report, HW-78180.
5. Stivers, G., "Radioisotope Thermoelectric Space Power Supplies," IEEE Transactions on Aerospace, Vol. 2, No. 2, pp 650-60, April 1964

6. "Shielding Requirements for Promethium Sources," HW-77375

7. "The Hanford Isotope Production Plant," HW-77770

APPROXIMATE EXPRESSION FOR SAIL MOBILITY

In order to determine the relative capabilities of various combinations of sail surface coatings without resorting to an extensive study of the various combinations by means of the mobility program, an approximate expression for determining the mobility of a sail has been devised for the case where the sun line is in the plane of the orbit and the plane of the sail is perpendicular to the plane of the orbit.

Under these restrictions the geometry of the situation is reduced to the two-dimensional model shown in figure IV-1. As can be seen, side 1 of the satellite faces the sun during the receding half of the orbit, while side 2 faces the sun during the approaching half.

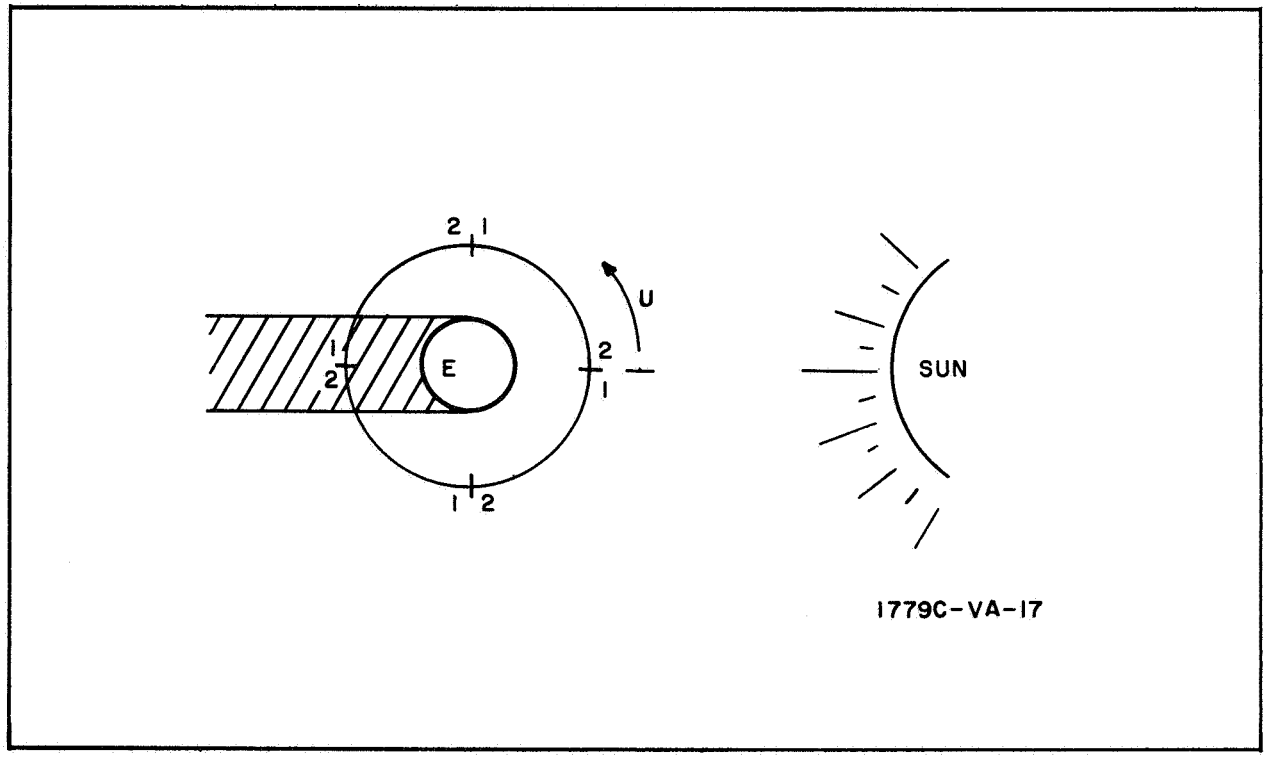

Figure IV-1. Orbit Geometry

For a circular orbit, the rate of change of the semi-major axis can be expressed as:

$$\frac{da}{dt} = \frac{2}{n} S \qquad \text{(IV-1)}$$

where n is the mean angular motion of the satellite and S is the perturbing acceleration in the tangential direction. The incident and diffusely reflected direct solar force component in the tangential direction can be expressed as:

$$F_s = \frac{S_c}{C}\left[\pm \sin U + \frac{2}{3} r\right] A \sin U \qquad \text{(IV-2)}$$

where S_c is the solar constant (440 Btu/hr ft^2), C is the speed of light, A is the area of the sail, r is the reflectivity of the sail surface facing the sun, and the plus or minus sign option is chosen plus if the satellite is receding from the sun and vice versa. The component of the reradiation force in the tangential direction can be expressed as:

$$F_R = \pm \frac{S_c}{C} \alpha \frac{2}{3} \quad \frac{\epsilon_1 - \epsilon_2}{\epsilon_1 + \epsilon_2} \quad A \sin U \qquad \text{(IV-3)}$$

where α is the solar absorptivity of the surface facing the sun, ϵ_1 and ϵ_2 are the emissivities of sides 1 and 2, respectively, and again the plus or minus sign option is chosen plus if the satellite is receding from the sun and vice versa.

In integrating the perturbing forces over the orbit, the portion of the orbit occulted by the earth's shadow must be considered to have 0 perturbing forces. The shadow half angle is defined as:

$$\psi = \sin^{-1}\left(\frac{R_e}{a}\right) \qquad \text{(IV-4)}$$

where R_e is the radius of the earth. Thus the change in semi-major axis per orbit (Δ a) can be expressed as:

$$\Delta a = \frac{2}{n^2} \frac{S_c}{C} \frac{A}{M} \left[\int_0^{\pi - 4} \left(\sin^2 U + \frac{2}{3} \gamma_1 \sin U + \frac{2}{3} \frac{\epsilon_1 - \epsilon_2}{\epsilon_1 + \epsilon_2} \alpha_1 \sin U \right) dU \right.$$

$$\left. + \int_{\pi + 4}^{2\pi} \left(-\sin^2 U + \frac{2}{3} \gamma_2 \sin U - \frac{2}{3} \frac{\epsilon_1 - \epsilon_2}{\epsilon_1 + \epsilon_2} \alpha_2 \sin U \right) dU \right] \quad \text{(IV-5)}$$

where m is the mass of the satellite. When the integration is performed, the term representing the incident radiation cancels out as would be expected from the geometry of the situation. This leaves the final expression as:

$$\Delta a = \frac{2}{n^2} \frac{S_c}{C} \frac{A}{M} (1 + \cos \psi) \frac{2}{3} \left[(\gamma_1 - \gamma_2) + \frac{(\epsilon_1 - \epsilon_2)(\alpha_1 + \alpha_2)}{\epsilon_1 + \epsilon_2} \right] \text{(IV-6)}$$

The mobility is thus proportional to the quantity within the brackets of equation IV-6 which can be reduced to:

$$\frac{2 (\alpha_2 \epsilon_1 - \alpha_1 \epsilon_2)}{\epsilon_1 + \epsilon_2}$$

From this expression, it can be seen that the optimum coating pattern would be to have γ_1 and ϵ_1 both equal to one while γ_2 and ϵ_2 are both equal to 0. This situation is not physically realizable, of course, but should be approached as nearly as possible to obtain maximum efficiency from the sail.

The relationships derived in this appendix have been checked with the results calculated by the mobility program. Among the particular cases checked are those shown in figure I-3 of Appendix I. The checks agreed very closely in all cases.

APPENDIX V

CONFIGURATIONS A AND B ECCENTRICITY STUDY

It is well known that the solar pressure forces cause significant variations in the orbital eccentricity of high area-to-mass ratio satellites and, in fact, cause the orbit to become resonant at certain critical inclinations. Since the attitude control errors also vary significantly as a function of the eccentricity of the orbit, an effort has been made to determine the maximum eccentricity as a function of inclination for the two configurations being studied.

In order to calculate the eccentricity variation, an average projected area was estimated for each configuration and used in conjunction with the estimated orbit weight to determine an average area-to-mass ratio for each satellite. These area-to-mass ratios were then used with the Lifetime 18 program to calculate the eccentricity as a function of time.

For the purpose of estimating the average projected area of the solid lenticule (configuration A), consider the orbital geometry shown in figure V-1 where the sun line is in the plane of the orbit. Then the projected area will vary between a maximum at γ equal to 0 where the satellite lies on the sun line to a minimum at γ equal to 90 degrees. The projected area for these two cases is:

A_A ($\gamma = 0$) = 56,000 sq ft

A_A ($\gamma = 90$) = 18,920 sq ft

If it is now assumed that the projected area varies sinusoidally between these limits then the average projected area over the orbit is simply the average of these two values or:

$\overline{A}_A$ ($i_s = 0$) = 37,460 sq ft

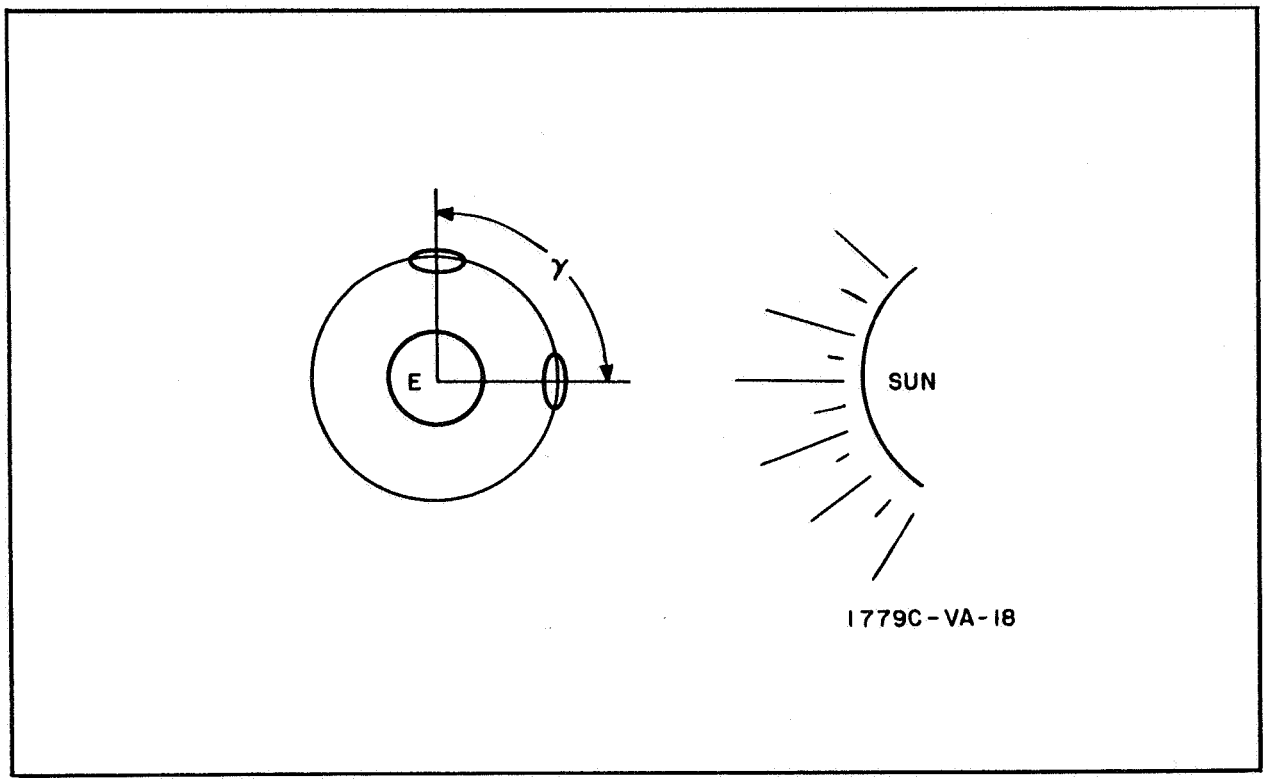

Figure V-1. Orbital Geometry

Consider now the case where the sun line is perpendicular to the plane of the orbit ($i_s = 90$). In this case, the edge of the lenticule always faces the sun so that:

$\overline{A}_A\ (i_s = 90) = 18,920$ sq ft

Again assuming that the average projected area varies sinusoidally between these limits as a function of the inclination of the sun line to the orbital plane, the area is:

$\overline{A}_A\ (i_s) = 28,190 + 9270 \cos 2\ i_s$

and is shown in figure V-2.

For the wire mesh lenticule of configuration B, it is assumed that one cap of the wire mesh structure covers 5 percent of the total area when in the orientation defined by γ equal to 0 in figure V-1. Furthermore, it is assumed that the percentage of radiation intercepted by the side facing away from the sun will be equal to:

$x\ (1 - x)$

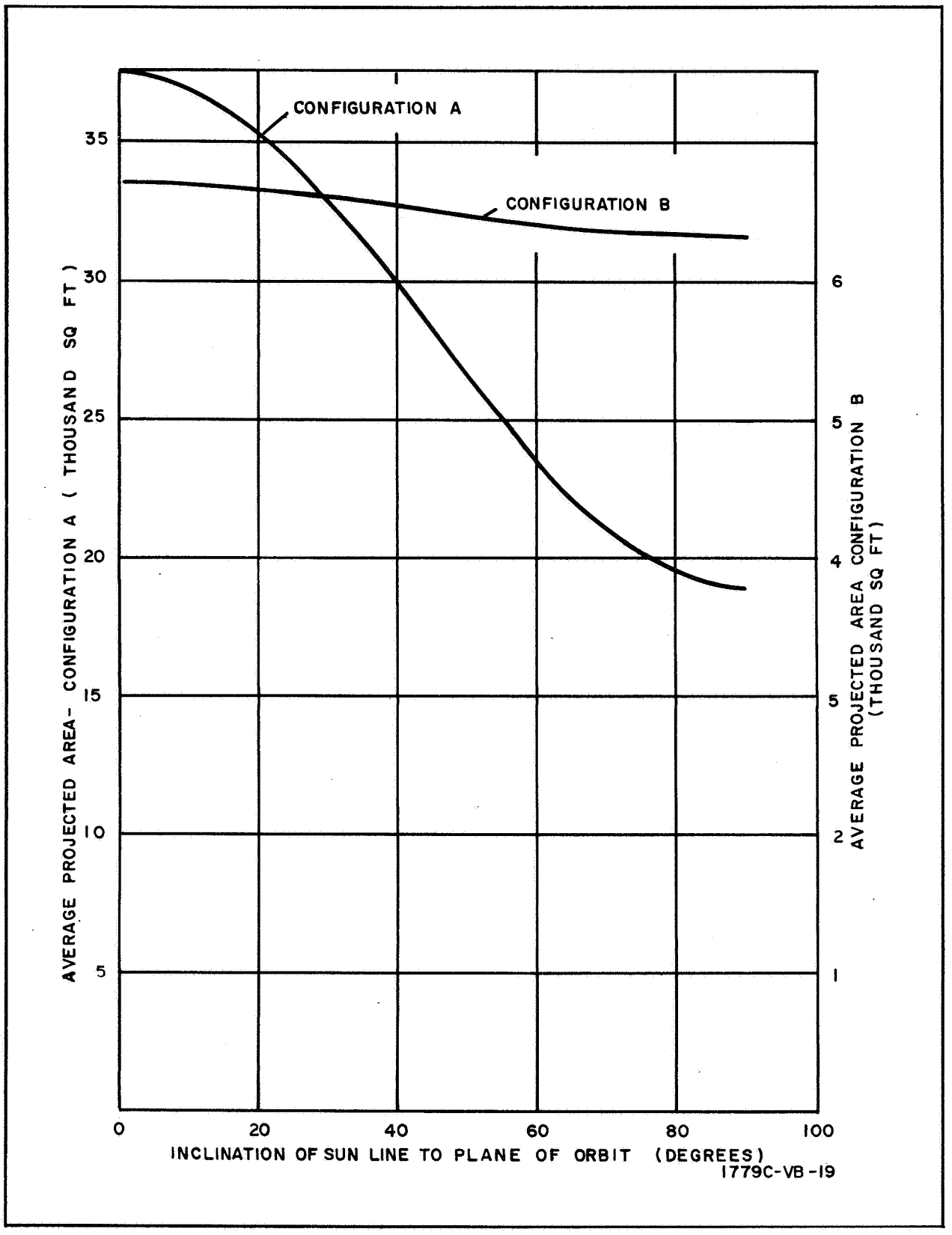

Figure V-2. Average Projected Area Over Orbit

where x is the percentage intercepted by the side facing the sun. At the γ equal to 90-degree position of figure V-1, the side facing the sun must have the same effective area as a γ equal to 0. Then the percentage of radiation intercepted by this side is:

$$x_{\gamma=90} = \frac{(0.05)(56,000)}{18,920}$$
$$= 0.148$$

and thus the effective area of the wire mesh lenticule at these two points is:

$$A_{Bl}(\gamma = 0) = 5460$$
$$A_{Bl}(\gamma = 90) = 5190$$

Assuming that the sail area is 3000 sq ft and that the fixed compensation (22-1/2-degree sail angle) control scheme is used the sail area at these two points will be:

$$A_{Bs}(\gamma = 0) = 0$$
$$A_{Bs}(\gamma = 90) = 2780$$

Thus, following the same procedure as for configuration A, the average for i_s equal to 0 and 90 degrees is:

$$\overline{A}_B(i_s = 0) = 6715$$
$$\overline{A}_B(i_s = 90) = 5190 + 1150$$
$$= 6340$$

and the same average projected area can be expressed as:

$$\overline{A}_B(i_s) = 6527 + 187 \cos 2 i_s$$

This area as a function of the inclination of the sun line to the orbital plane is also shown in figure V-2. If the distribution of i_s as shown in figure VIII-7 of Appendix VIII is applied to the area curve of figure V-2, the following values are obtained for the average projected area.

Configuration	$\bar{A}_i$ = 45 degrees (ft^2)	$\bar{A}_i$ = 60 degrees (ft^2)	$\bar{A}_i$ = 75 degrees (ft^2)	Average Area (ft^2)	Weight (lb)	Area/Mass (ft^2/lb)
A	32,310	30,200	29,100	30,540	1,152	26.5
B	6,605	6,565	6,544	6,571	777	8.55

Since the average projected area at the three inclinations did not vary more than 10 percent, the average of the three has been used as a constant in determining the area-to-mass ratios of the two configurations for purposes of calculating the eccentricity variations.

Shown in figures V-3 and V-4 are the maximum eccentricities which can be expected as a function of inclination for posigrade and retrograde orbits, respectively. The region of best communications orbits is shown to be between the inclinations of 45 and 75 degrees as was indicated by the Phase I study. The retrograde equivalent of this range is of course between 105 and 135 degrees. As can be seen, the eccentricities for the posigrade orbits in this range are much more tolerable. Only one small resonance is seen to occur in the posigrade region, making the inclinations between 47 and 55 degrees impractical, while much of the retrograde region is resonant or near-resonant. For these reasons and from a launch efficiency viewpoint, then the posigrade orbits have a significant advantage over the retrograde orbits at the 2000-nautical-mile altitude considered.

Within the posigrade region, the point of lowest eccentricity is seen to occur near 60-degree inclination. At that point, the maximum eccentricity of the configuration A satellite is seen to reach a value of 0.029, while the configuration B satellite does not exceed 0.01 eccentricity.

Figure V-5 shows a typical variation of the eccentricity as a function of time from launch. The case shown is for a 45-degree orbit with a satellite having an area-to-mass ratio of 8.9 sq ft per pound. For use with other

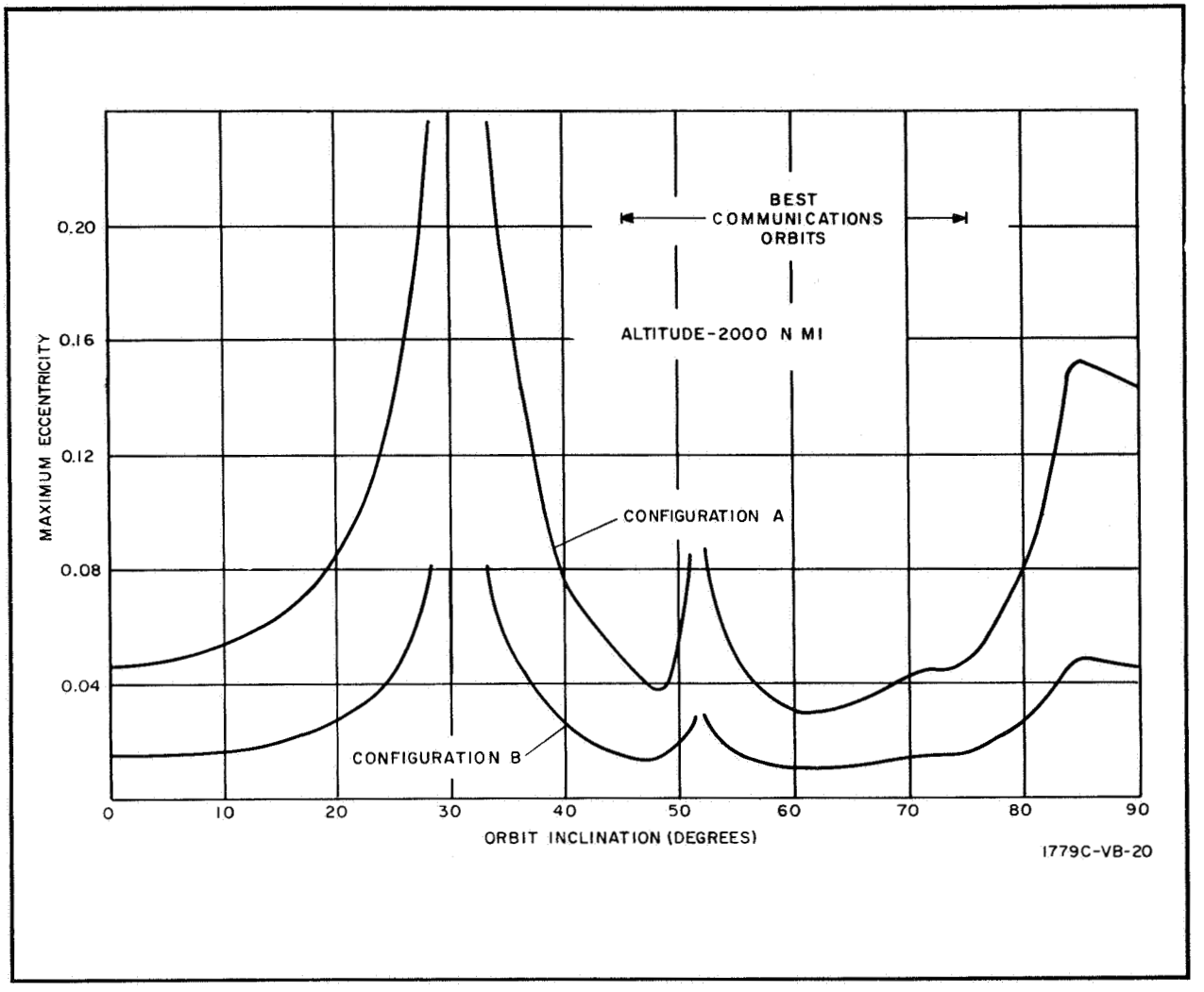

Figure V-3. Maximum Eccentricity vs Inclination (Posigrade Orbits)

area-to-mass ratio satellites, the eccentricity can be assumed to be a linear function of the area-to-mass ratio.

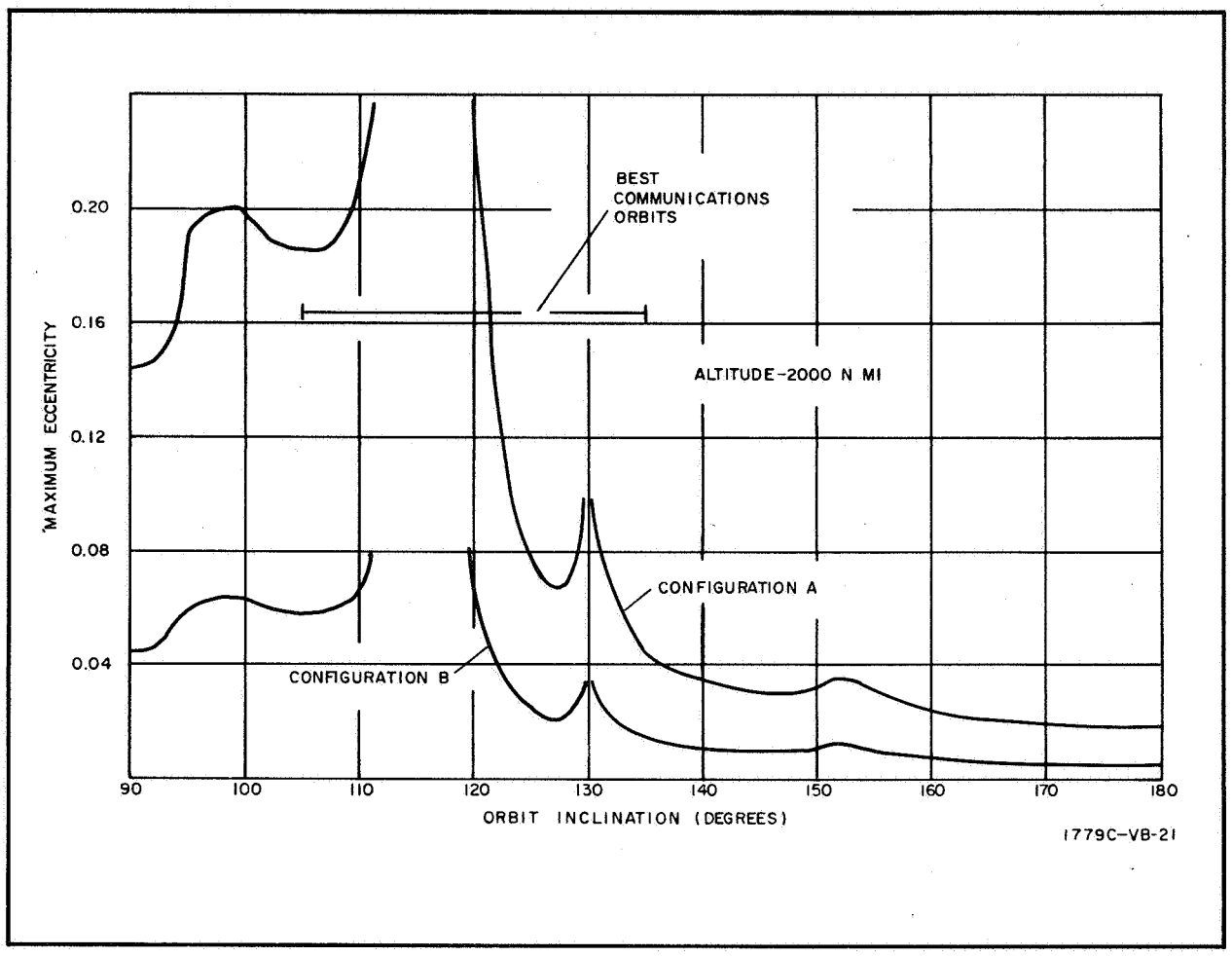

Figure V-4. Maximum Eccentricity vs Inclination (Retrograde Orbits)

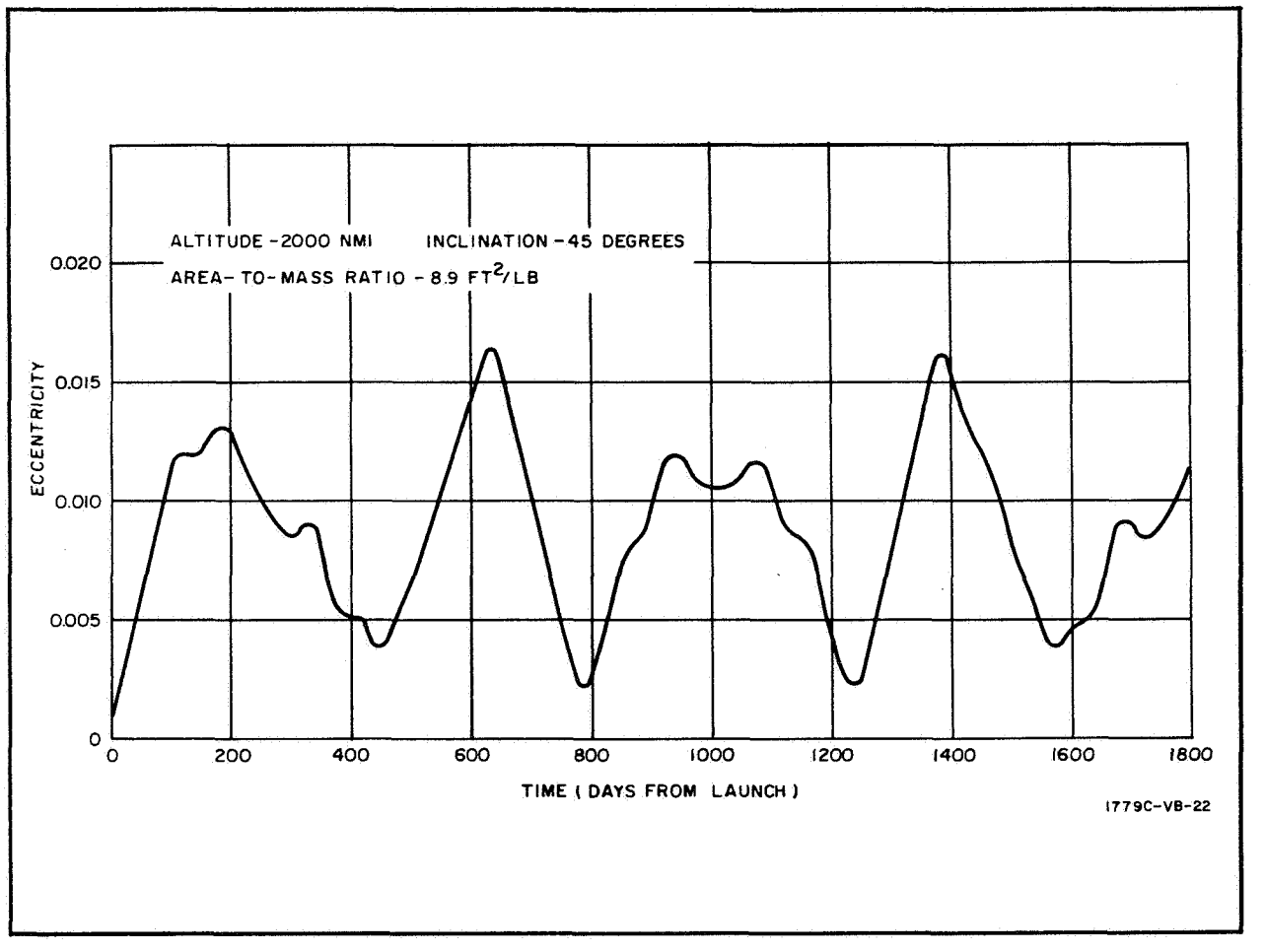

Figure V-5. Eccentricity as a Function of Time

APPENDIX VI

SKIN TEMPERATURE, MOBILITY TRADEOFF SKIN FOR OPAQUE LENS

In order to determine a set of surface coatings for the opaque lens which would produce both feasible skin temperatures and a sufficient amount of mobility, a study has been made to determine the trends of both these quantities as functions of the coating pattern.

As a common starting point for the study, the coating configuration used in the Phase II study was examined. This configuration for a satellite weighing approximately 1200 pounds is known to be capable of producing about 125 degrees per month of mobility. Since previous studies have shown that mobility does not vary significantly as a function of the internal emissivity, an initial study was made to determine the optimum internal emissivity with respect to the skin temperatures on the lenticule.

The results of this study are shown in figure VI-1. The temperatures were calculated by means of a digital computer program based on a method described in Appendix C of the Phase II final report. In these initial investigations the effects of earth radiation on the satellite are neglected. The skin temperatures at various positions on the surface of the lenticule are given for the various configurations studied. The constant temperature surfaces are divided by planes intersecting the lenticular surface at equal distances from the plane of the rim.

As expected, the maximum temperature point occurs in the quadrant facing the sun with the lowest external emissivity. When the internal emissivity of that quadrant is low the maximum temperature is seen to occur in the top segment of this quadrant, while when the internal emissivity is high the maximum temperature is seen to occur in the rim segment.

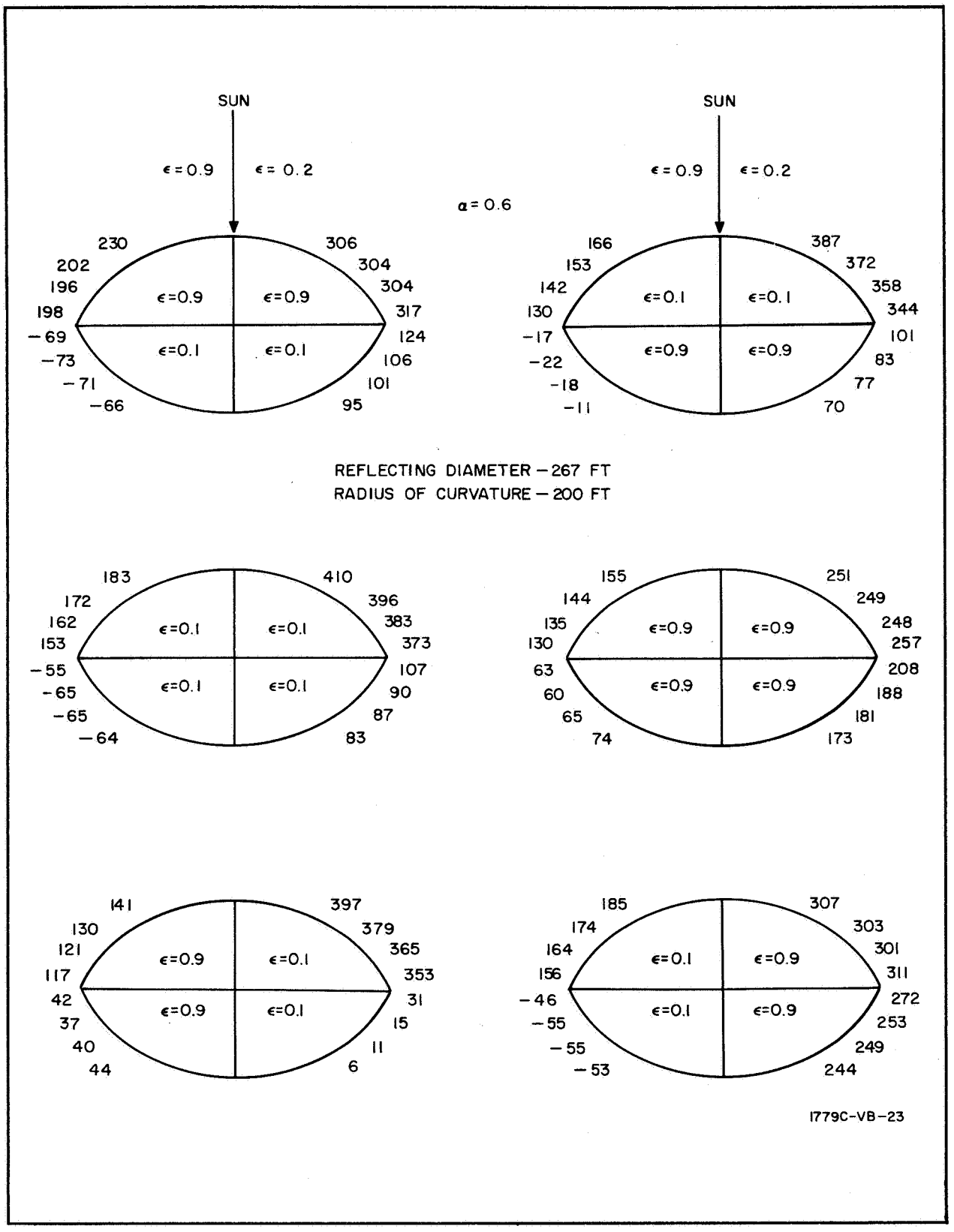

Figure VI-1. Internal Emissivity Study

In general, it can be seen that the higher emissivity configurations distribute the energy more uniformly over the surface of the satellite, thus producing a more uniform temperature distribution. The results of this particular study indicate that a uniform internal emissivity of as high as possible a value will produce the most uniform temperature distribution and thus the lowest maximum temperature. For this reason a uniform internal emissivity of 0.9 (highest practical internal emissivity which can be achieved by Goodyear) has been chosen.

In order to estimate the relative mobility associated with various configurations, a procedure used in estimating the relative mobility of a spherical satellite has been used. Since the absorptivity is assumed to be uniform over the surface, the mobility will be produced by a difference in the reradiation forces over the orbit. In the case of the spherical satellite, the difference in the tangential component of the reradiation forces when the axis of symmetry is aligned in opposite directions along the sun line has been found to be a very good indication of the relative mobility capabilities of various coating configurations. Since the lenticular shape under consideration is not too far removed from a sphere, it was believed, and in fact, has subsequently been shown, that the same quantity would be a good indication of the relative mobility capabilities of the lenticular configuration.

It can be shown that the reradiation force on a sphere when the axis of symmetry of the satellite is aligned with the sun line vector is:

$$F_R = \frac{-4\pi R^2}{3C} \left[\frac{\epsilon_1}{\epsilon_1 + \epsilon_i} \left(\frac{C_S a_S}{3} + \frac{\delta S}{2} \right) - \frac{\epsilon_2}{\epsilon_2 + \epsilon_i} \frac{\delta S}{2} \right]$$

where δS is the product of the internal absorptivity and the radiation incident on the internal surface and can be determined by:

$$\delta S = \left[\frac{\dfrac{\epsilon_i}{\epsilon_1 + \epsilon_i}}{\dfrac{\epsilon_1}{\epsilon_1 + \epsilon_i} + \dfrac{\epsilon_2}{\epsilon_2 + \epsilon_i}} \right] \frac{C_s a_S}{2}$$

and ϵ_1 and ϵ_2 are the external emissivities of the sides facing towards and away from the sun respectively, α_s is the solar absorptivity of the external surface, ϵ_i is the internal emissivity of the surface, C_S is the solar radiation density (440 Btu/hr ft^2), R is the radius of the sphere, and C is the speed of light.

The mobility of the satellite is then assumed to be directly proportional to the net difference in the reradiation force evaluated for opposite sides facing the sun. Using the 125 degrees per month mobility of the configuration studied in Phase II as a base, the mobility of the various configurations has been estimated.

The distribution of skin temperatures for some of the configurations studied are shown in figures VI-2 through VI-5. In these figures the effects of earth radiation are neglected. In general, it can be shown that the earth radiation will add approximately 20 degrees to both the maximum and minimum temperatures.

The configuration of figure VI-2 is that which was used in the Phase II final report. Figure VI-3 shows the effects of lowering the high emissivity to 0.8 and is seen not to affect the temperatures significantly. In figure VI-4 the lower emissivity is lowered to 0.1 and is seen to increase the temperatures significantly. In figure VI-5 the effects of reducing the absorptivity are shown to reduce the temperatures since less energy is absorbed by the satellite. Table VI-1 summarizes these results and also shows the estimated mobilities for each of these configurations.

At this point of the study additional inputs were obtained from the Goodyear Aerospace Corporation with regards to the properties of the surface materials. The maximum allowable surface temperature was specified to be 250°F and an external emissivity of 0.8 was specified as the highest value achievable.

Since none of the configurations fit the design criteria very closely, a new search was initiated to find the best combination of surface coatings. The

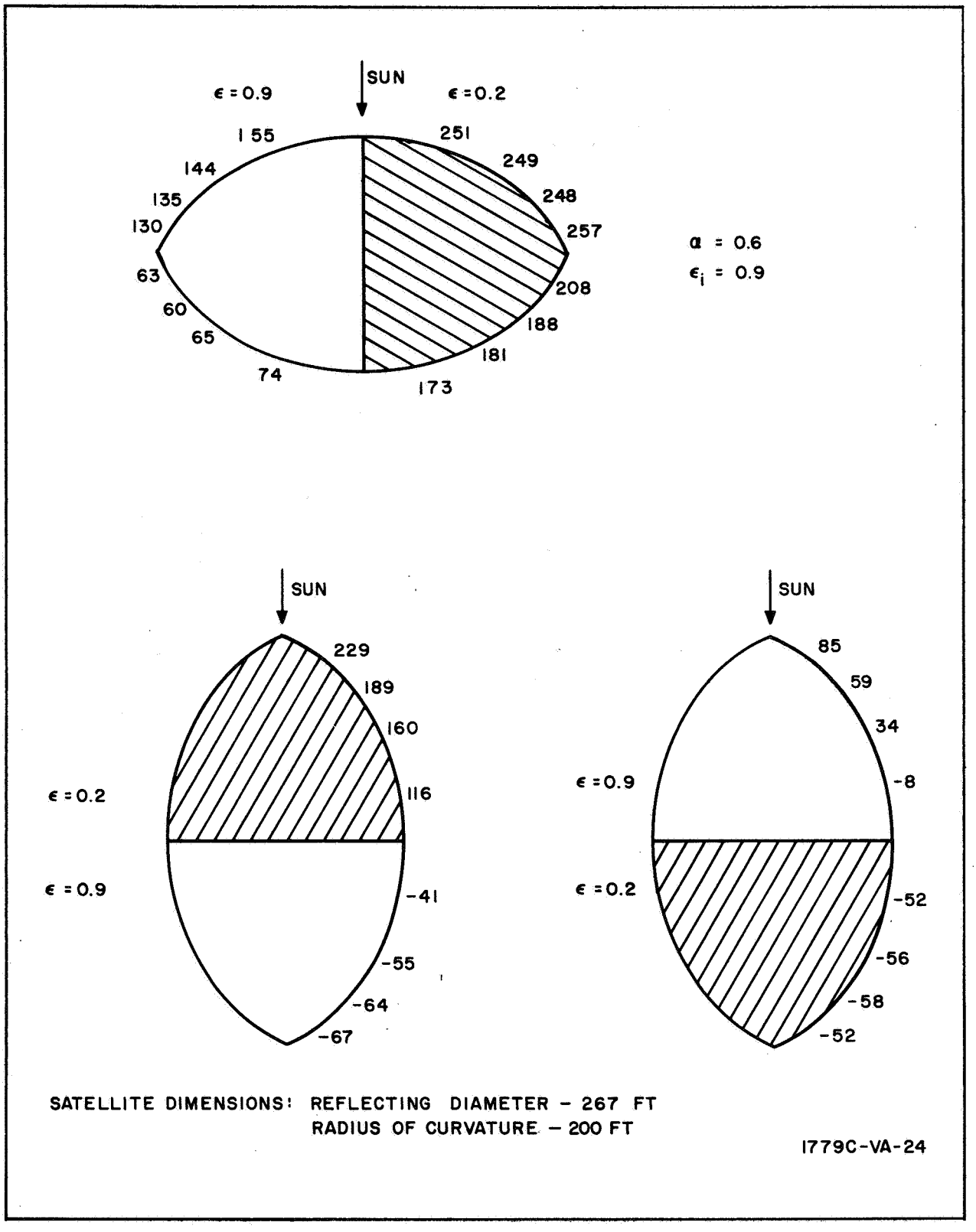

Figure VI-2. Skin Temperatures; 0.2 and 0.9 Emissivity and 0.6 Absorptivity

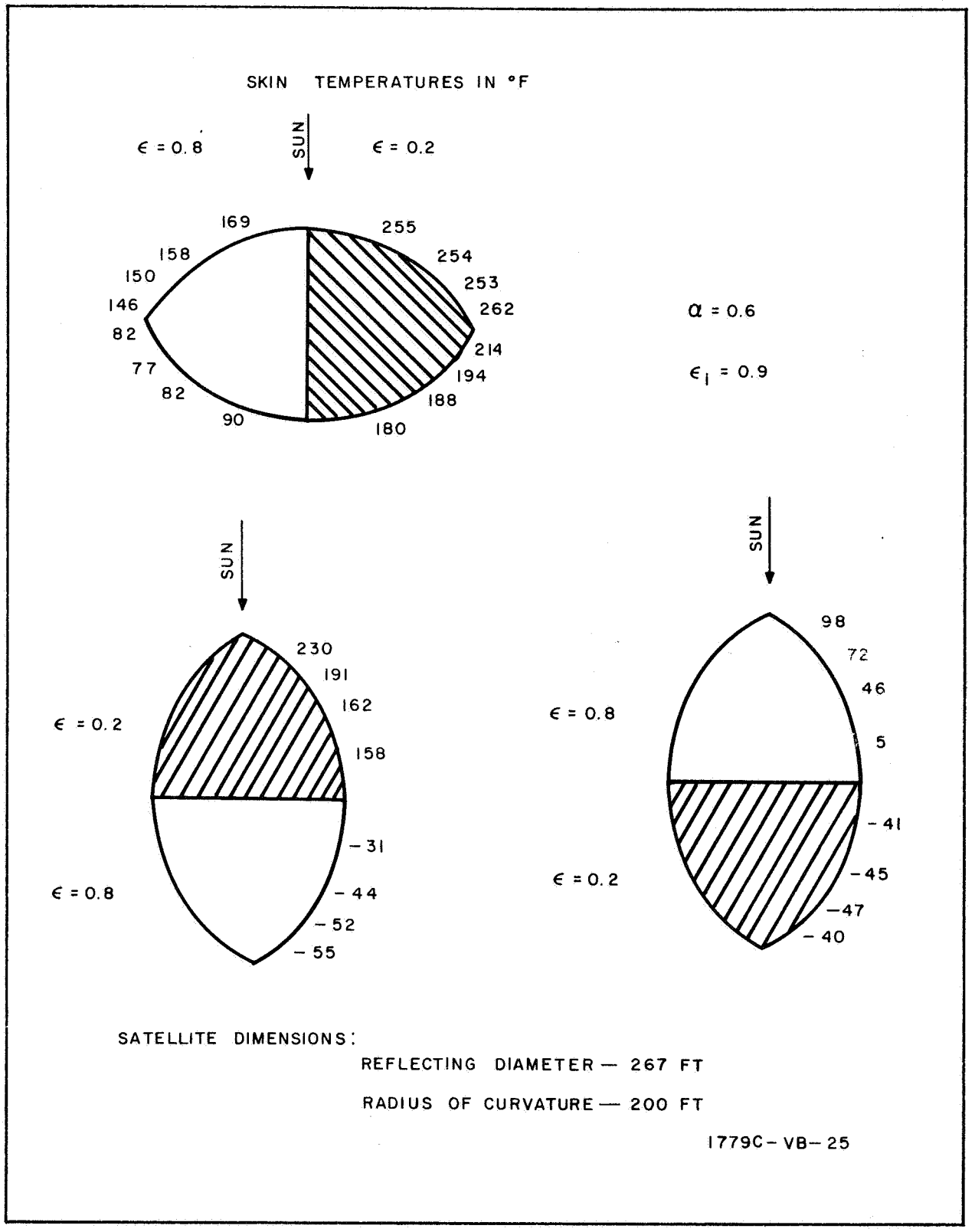

Figure VI-3. Skin Temperatures; 0.2 and 0.8 Emissivity and 0.6 Absorptivity

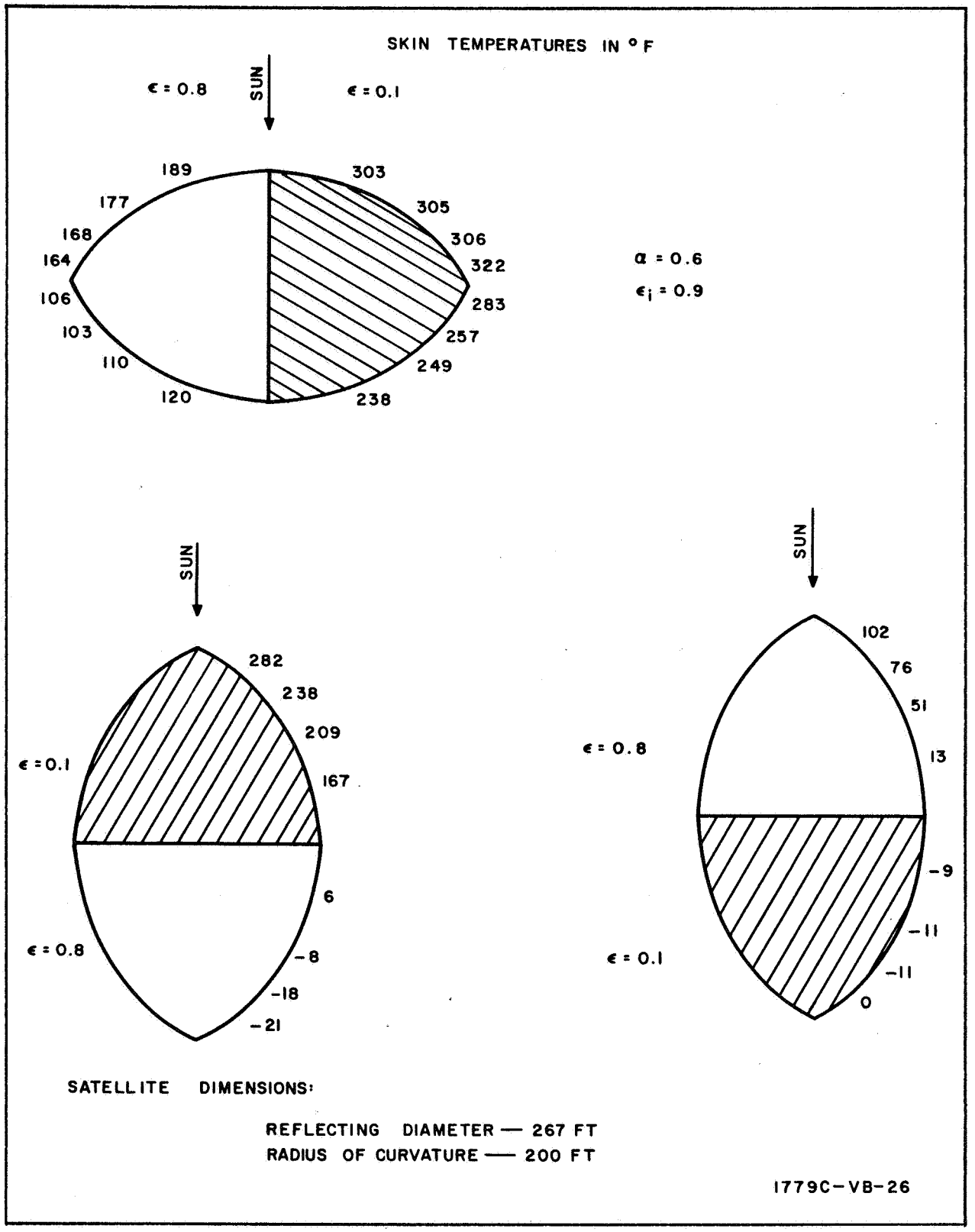

Figure VI-4. Skin Temperatures; 0.1 and 0.8 Emissivity and 0.6 Absorptivity

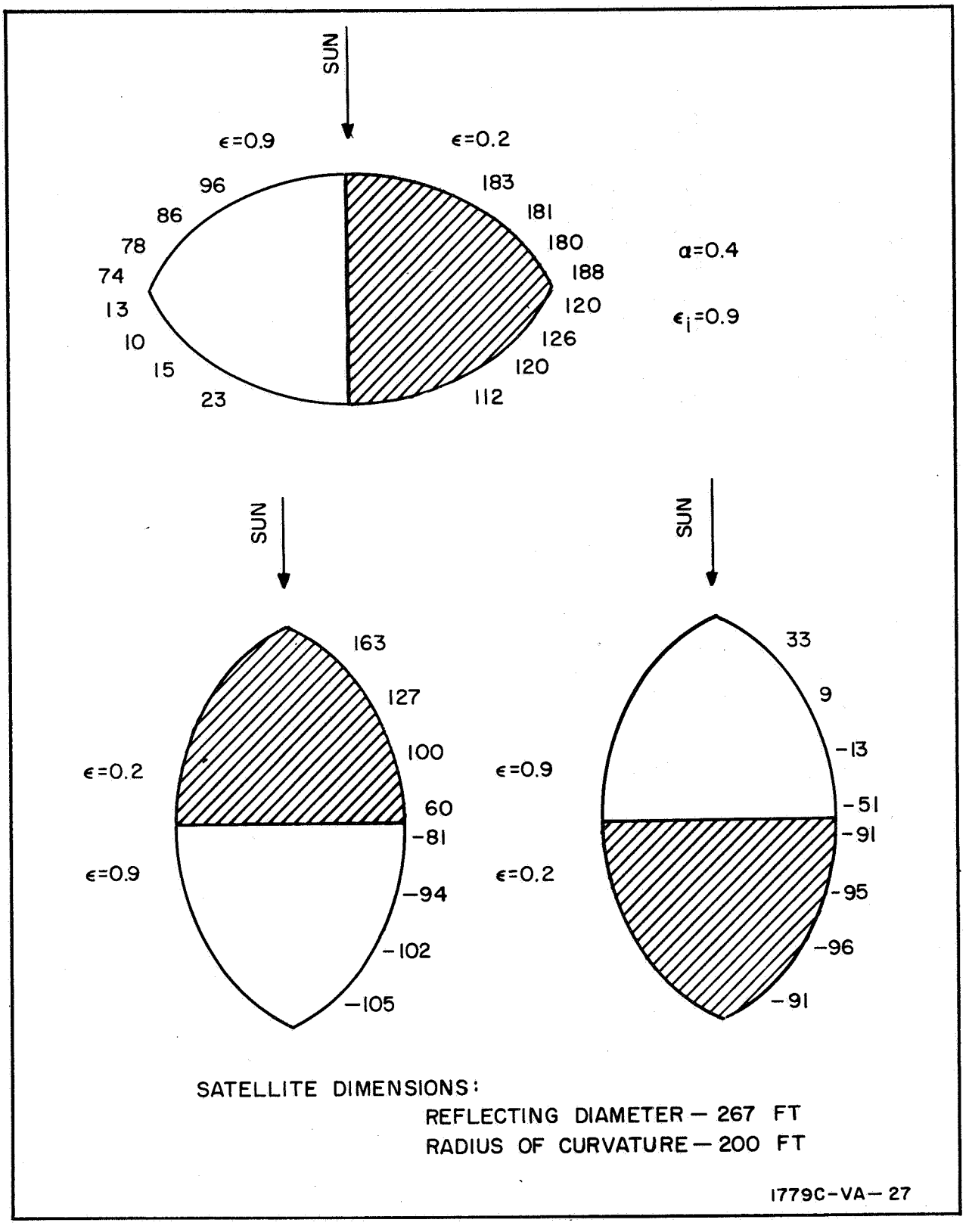

Figure VI-5. Skin Temperatures; 0.2 and 0.9 Emissivity and 0.4 Absorptivity

TABLE VI-1

TEMPERATURE, MOBILITY SUMMARY CHART

ϵ_1	ϵ_2	α	T_{max} (°F)	T_{min} (°F)	Mobility (deg/month)
0.9	0.2	0.6	257	-67	125
0.8	0.2	0.6	262	-55	119
0.8	0.1	0.6	322	-21	173
0.9	0.2	0.4	188	-105	83

previous studies indicated two directions for the search to take. The first was to maintain an external emissivity pattern of 0.8 and 0.2 while lowering the absorptivity until the temperature remained within the 250-degree limit. The second was to follow the same procedure using an external emissivity pattern of 0.8 and 0.1.

The final skin temperatures of these two searches are shown in figures VI-6 and VI-7. The estimated mobility associated with the 0.8, 0.2 external emissivity pattern was 99 degrees per month while the other pattern produced 101 degrees per month. Thus, since the 0.8, 0.1 external emissivity pattern produced both slightly lower temperatures and slightly higher mobilities it was selected as the pattern to be used for study in the current report.

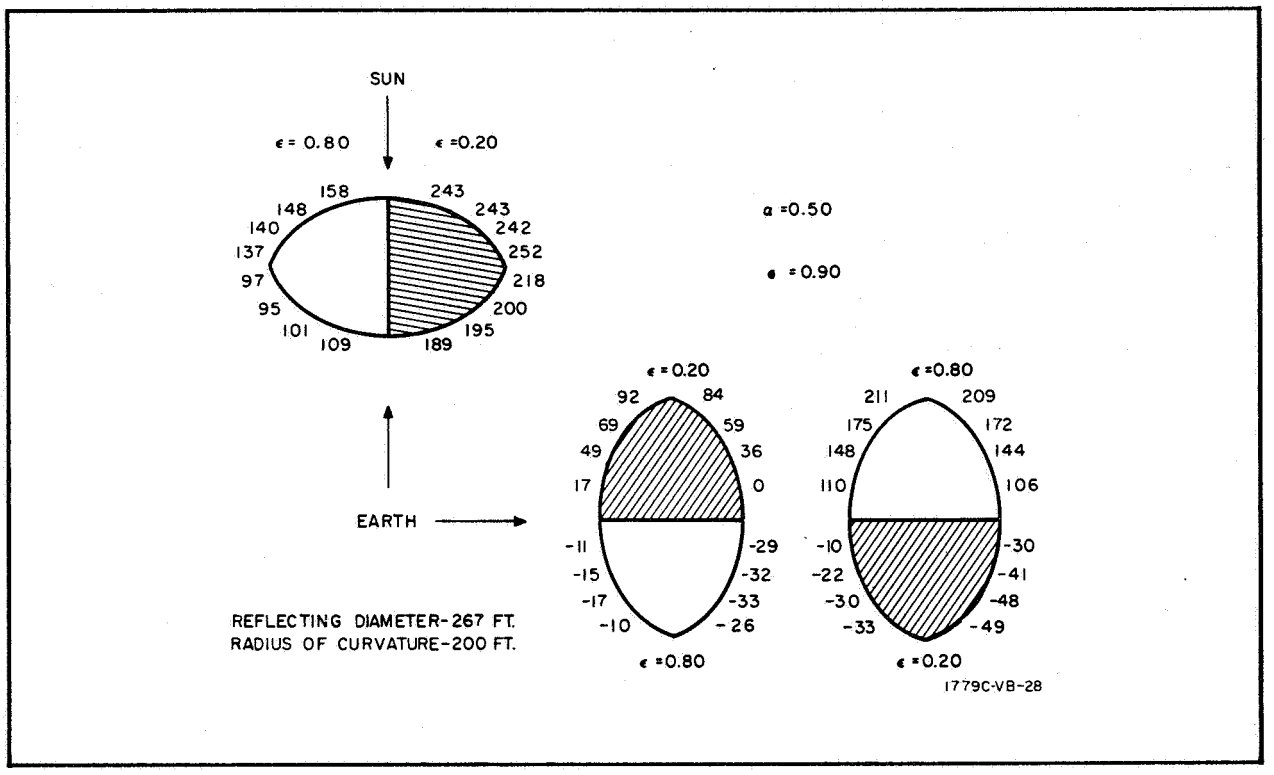

Figure VI-6. Skin Temperatures; 0.8 and 0.2 Emissivity and 0.5 Absorptivity

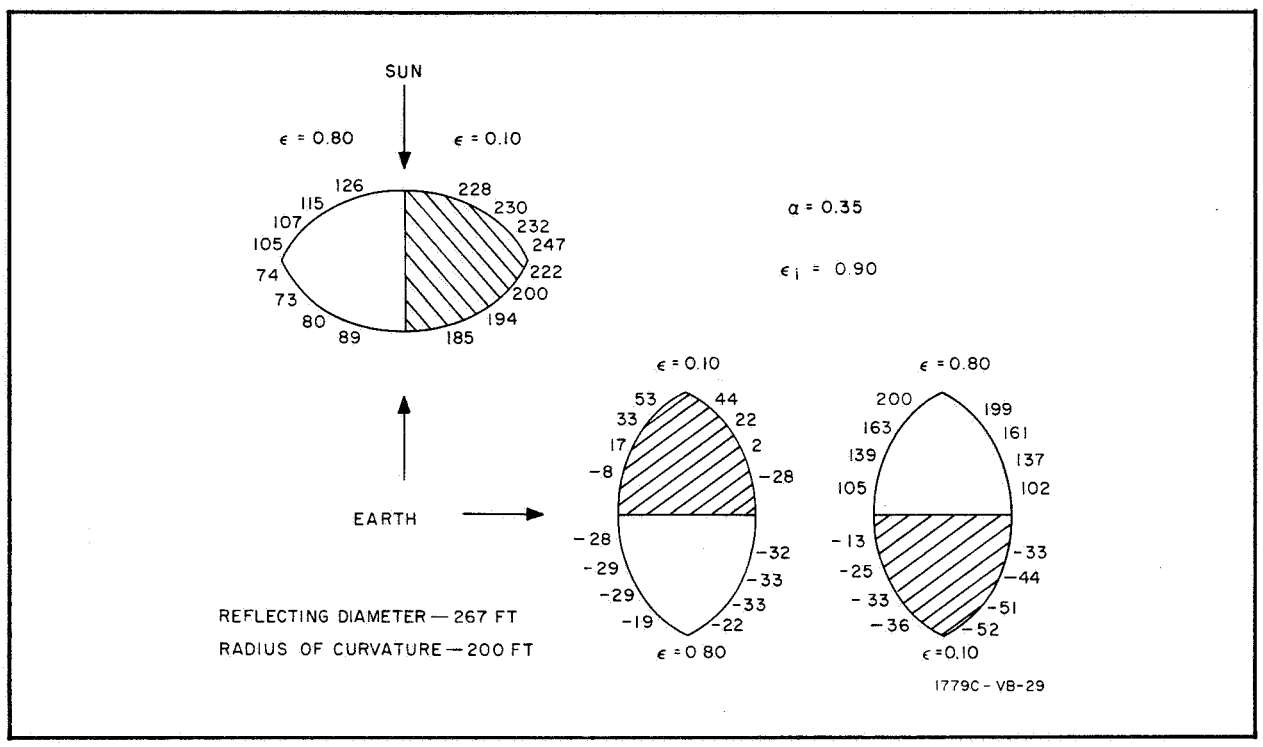

Figure VI-7. Skin Temperatures; 0.8 and 0.1 Emissivity and 0.35 Absorptivity

APPENDIX VII

SKIN TEMPERATURE, MOBILITY TRADEOFF STUDY FOR SAIL MATERIAL

In selecting a coating pattern for the sail material, the problem is similar to that encountered in selecting a pattern for the opaque lens. The pattern selected should both maintain a feasible temperature and produce as much mobility as possible.

In order to calculate the sail temperature, the balance of energy equation, which equates the energy absorbed by the sail to the energy emitted by the sail, can be written at the point where the plane of the sail is normal to the sun line vector as:

$$\alpha_i C_s = \sigma (\epsilon_1 + \epsilon_2) T^4$$

where

- α_i - solar absorptivity of side facing the sun
- $\epsilon_1 \epsilon_2$ - emissivities of the two sides
- C_s - solar radiation density (440 Btu/hr ft^2)
- σ - Stefan-Boltzman constant (1.73×10^{-9} Btu/hr $ft^2 deg^4$)
- T - surface temperature

Since the criteria as specified by Goodyear is that the surface temperature cannot exceed 250° Fahrenheit, it is sufficient to examine the point of maximum temperature. This is seen to occur when the side having the higher absorptivity is facing the sun under the normal condition described above. Thus the maximum temperature can be expressed as:

$$T_m^4 = \frac{\alpha_m C_s}{\sigma (\epsilon_1 + \epsilon_2)}$$

From the analysis of Appendix VI, the mobility is seen to be directly proportional to the quantity:

$$\frac{\alpha_2 \epsilon_1 - \alpha_1 \epsilon_2}{\epsilon_1 + \epsilon_2}$$

For the coating configuration originally selected on the basis of the maximum mobility within the range of values of coating parameters specified by Goodyear (Appendix IV), a maximum temperature of 271° Fahrenheit was calculated. Since the later upper limit of 0.8 on the external emissivity is seen to both lower the temperature and increase the mobility, this was the next configuration considered. For this configuration, a temperature of 250° was calculated. Even though this temperature is within the safe limits, it must be remembered that the effects of earth radiation have not yet been considered. Although in normal operation the effects of earth radiation will be very small since the sail is aligned parallel to the earth's axis, a margin of safety of about 20° was sought to cope with any large attitude control errors which might be encounted in the detumbling phase.

As can be seen, there were two remaining possibilities for obtaining a further reduction in the maximum temperature. Either the higher absorptivity could be lowered or the lower emissivity could be raised. The effects of these two courses of action along with the previous cases, are shown in table VII-1. In this table, the mobility of the original configuration is arbitrarily set to one and the other mobilities are calculated relative to that case. For all cases, an absorptivity of 0.1 was used for side one.

TABLE VII-1

SUMMARY CHART OF TEMPERATURE, MOBILITY STUDY

α_2	ϵ_1	ϵ_2	Relative Mobility	Maximum Temperature (°F)
0.9	0.7	0.1	1.000	271
0.9	0.8	0.1	1.018	250
0.9	0.8	0.2	0.904	232
0.8	0.8	0.1	0.904	230

Since there is little to choose between the last two cases with regards to either skin temperature or mobility, the configuration of the third case was chosen on a somewhat arbitrary basis as the configuration to be used in the final study of the sail mobility.

APPENDIX VIII

STUDY OF SAIL AND LENTICULAR MOBILITIES

This appendix describes the studies performed on the mobility capabilities of both the sail and lenticule final coating configurations selected as described earlier. The mobility of the sail as a function of the angle between the plane of the sail and the plane of the orbit is shown. The relative mobilities associated with several different methods of controlling the sail angle are discussed and the tradeoffs in selecting a method of control are shown. An average mobility based upon calculated distributions of the inclination of the sun line to the plane of the orbit as a function of the inclination of the orbit is developed.

The geometry associated with the study of mobility as a function of the sail angle is shown in figure VIII-1. The top view shows the direction of motion of the satellite and the plane of the sail being aligned along the radius vector to the satellite. The side view shows the plane of the orbit and the plane of the sail as seen from the radius vector. The sail angle, ϕ, then is defined to be the angle between a vector, $\bar{N}$, normal to the plane of the sail, and the plane of the orbit and is defined to be positive counterclockwise. The regions of positive and negative sun line inclinations are defined as shown.

Based upon these definitions, figures VIII-2 and VIII-3 show the change in semi-major axis per orbit as a function of the inclination of the sun line to the orbital plane for a 1500-pound satellite having a sail area of 7500 square feet and orbiting the earth at a 2000-nautical mile altitude. Figure VIII-2 shows families of curves at 15-degree increments of the sail angle for first quadrant angles, while figure VIII-3 gives the same information for third quadrant angles. From symmetry considerations, it can be shown that the

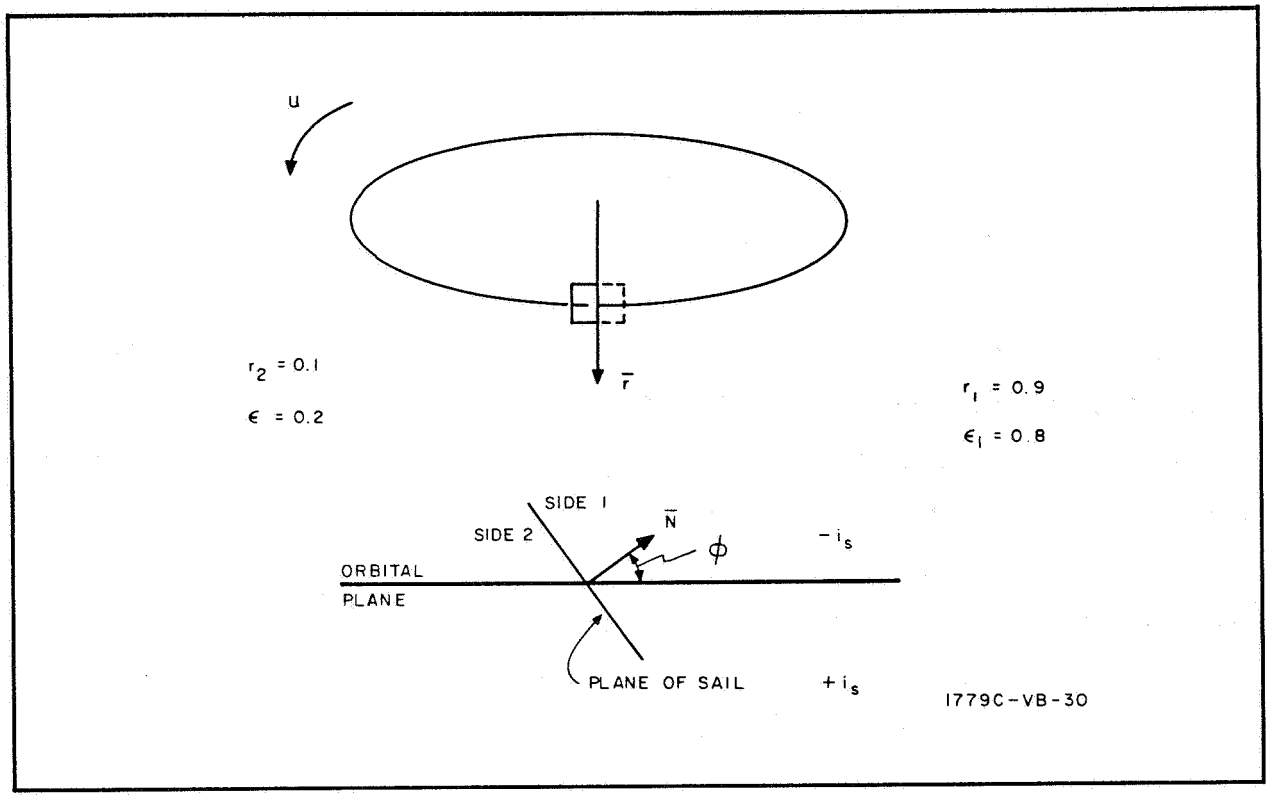

Figure VIII-1. Geometry of Sail Angle

following relationships can be used to determine the mobilities for the values of i_s and ϕ not shown in the figures.

$$M(-\phi, -i_s) = M(\phi, i_s) \qquad \text{(VIII-1)}$$

$$M(\pi - \phi, i_s) = -M(\phi, i_s) \qquad \text{(VIII-2)}$$

where $M(\phi, i_s)$ is defined as the change in semi-major axis per orbit at the value of ϕ and i_s specified.

As can be seen, the conventional method of control, that is, achieving the mobility by aligning the plane of the sail normal to the plane of the orbit (ϕ equal to 0 and 180 degrees) produces the optimum mobility only in a small region of i_s around 0. As the sun line vector moves out of the plane of the orbit, it is seen that other sail angles produce a greater amount of mobility. In particular, a sail angle varying between 0 and 45 degrees is seen to produce the optimum positive Δa in the region of negative i_s.

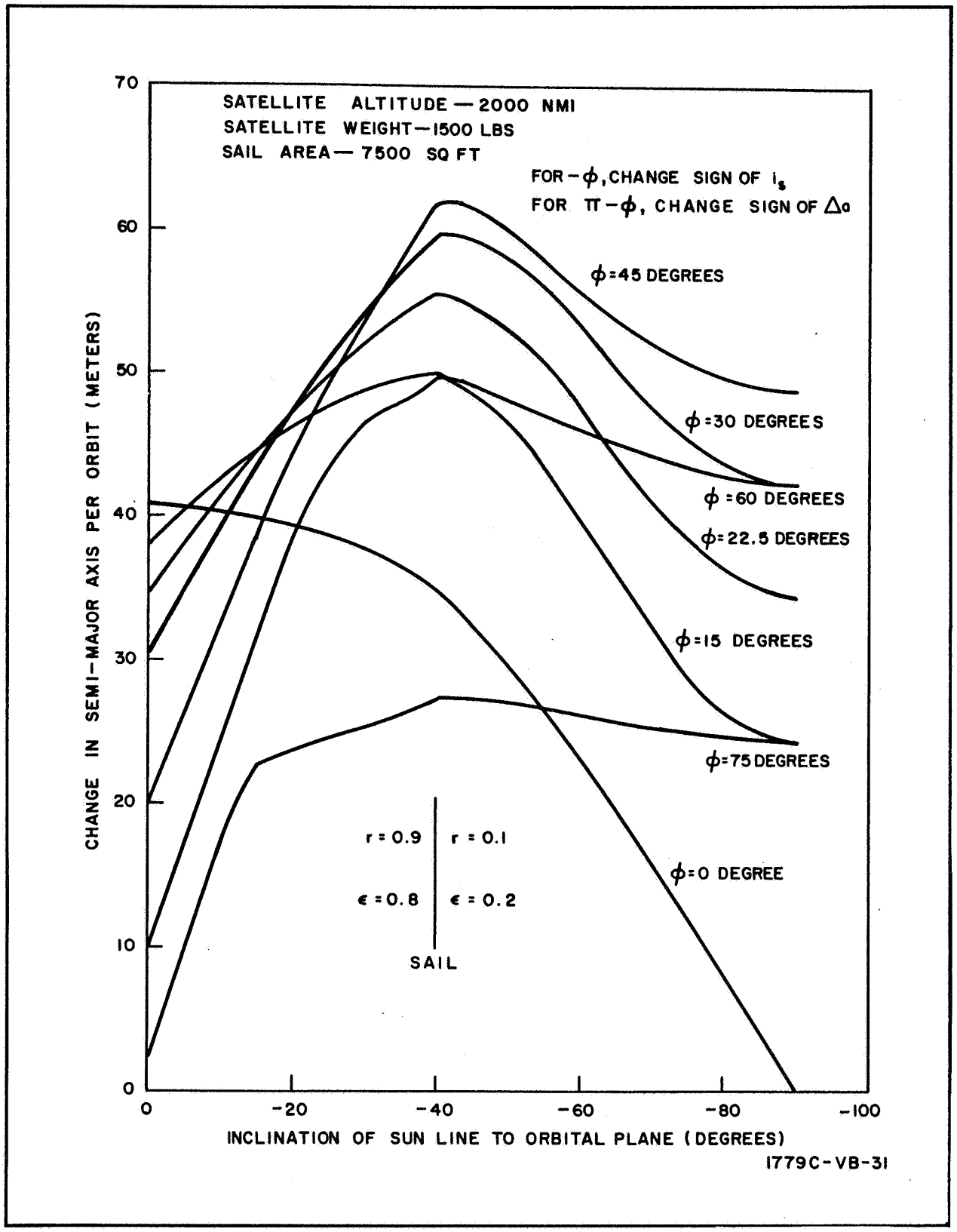

Figure VIII-2. First Quadrant Sail Angle Mobilities

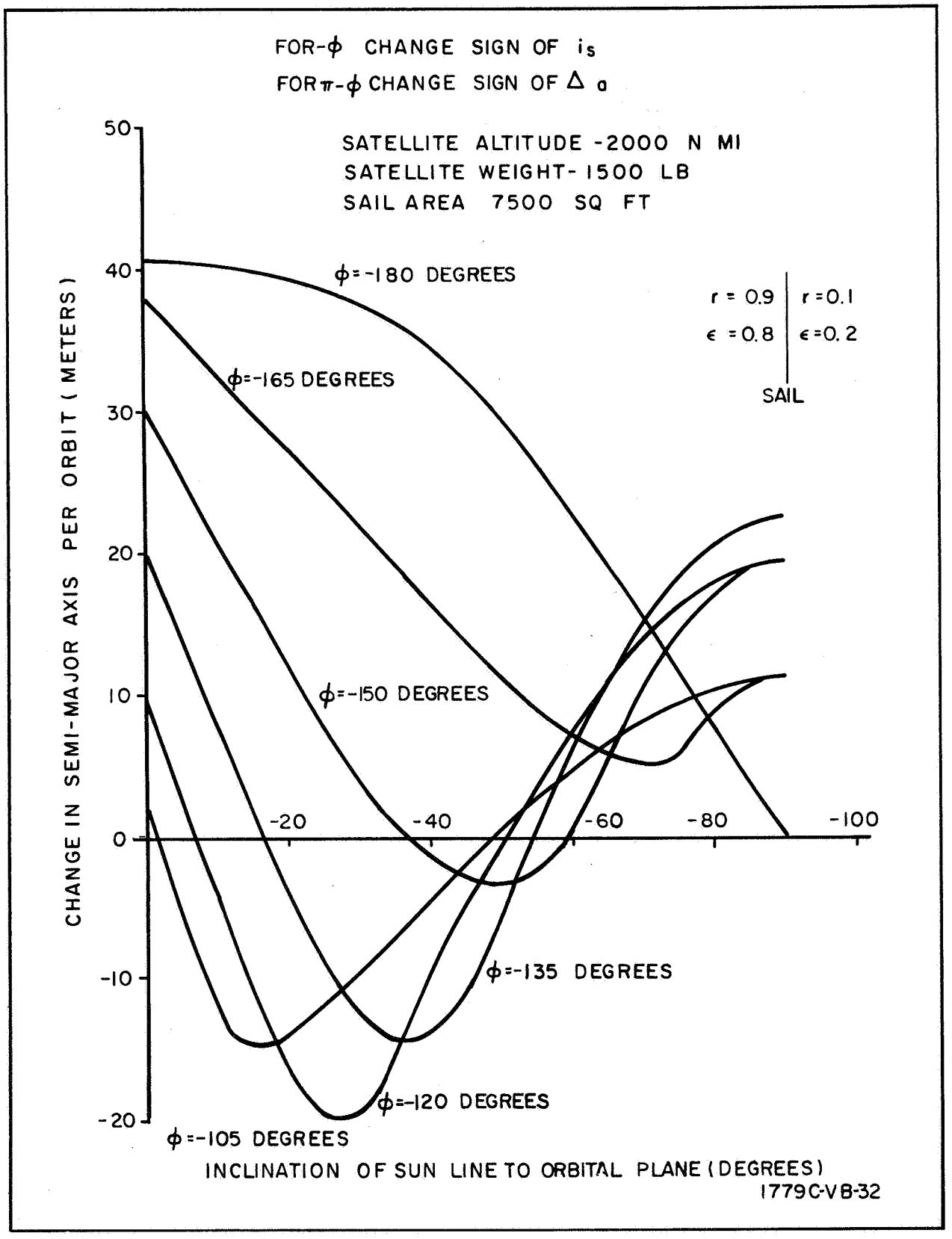

Figure VIII-3. Third Quadrant Sail Angle Mobilities

Figure VIII-4 shows the change in semi-major axis per orbit which can be achieved by each of three different control procedures. The procedure labeled continuous compensation involves a procedure whereby the variation of the sun line inclination is continuously compensated by varying the sail angle such that the optimum mobility is achieved. The procedure labeled fixed compensation involves a setting of the sail angle at some fixed value (22.5 degrees) which gives an approximately balanced Δa curve with respect to i_s. The third method, called uncompensated, uses the conventional control philosophy of aligning the sail normal to the plane of the orbit.

In figure VIII-5 are shown the sail angle settings required for the various control procedures as a function of the inclination of the sun line to the orbital plane. The settings required are shown for both increasing energy and decreasing energy modes. For example, the required settings for the increasing energy and decreasing energy modes under the uncompensated control procedure are seen to be 0 and 180 degrees, respectively. The two neutral mode settings at sail angles of plus or minus 90 degrees are also shown

As can be seen, the uncompensated control requires two state settings for the sail angle (0 and 180 degrees), the fixed compensation control requires four state settings (22.5, -22.5, 157.5, and -157.5 degrees), and the continuous compensation control requires a continuously variable sail angle. In addition, it is desirable to make a neutral mode available for all the control procedures in order to eliminate the necessity for a duty cycle type of control during normal operation of the system.

Figure VIII-6 shows the change in semi-major axis per orbit as a function of the sun line inclination for the opaque lens. As can be seen, the curve remains fairly constant from 0 to 30 degrees, peaks at the point where the orbit emerges from the earth's shadow, and decreases at the higher sun line inclinations. In general, it can be seen that the mobility of the opaque lens is less than that of the sail configuration shown, especially for the fixed compensation and continuous compensation control schemes.

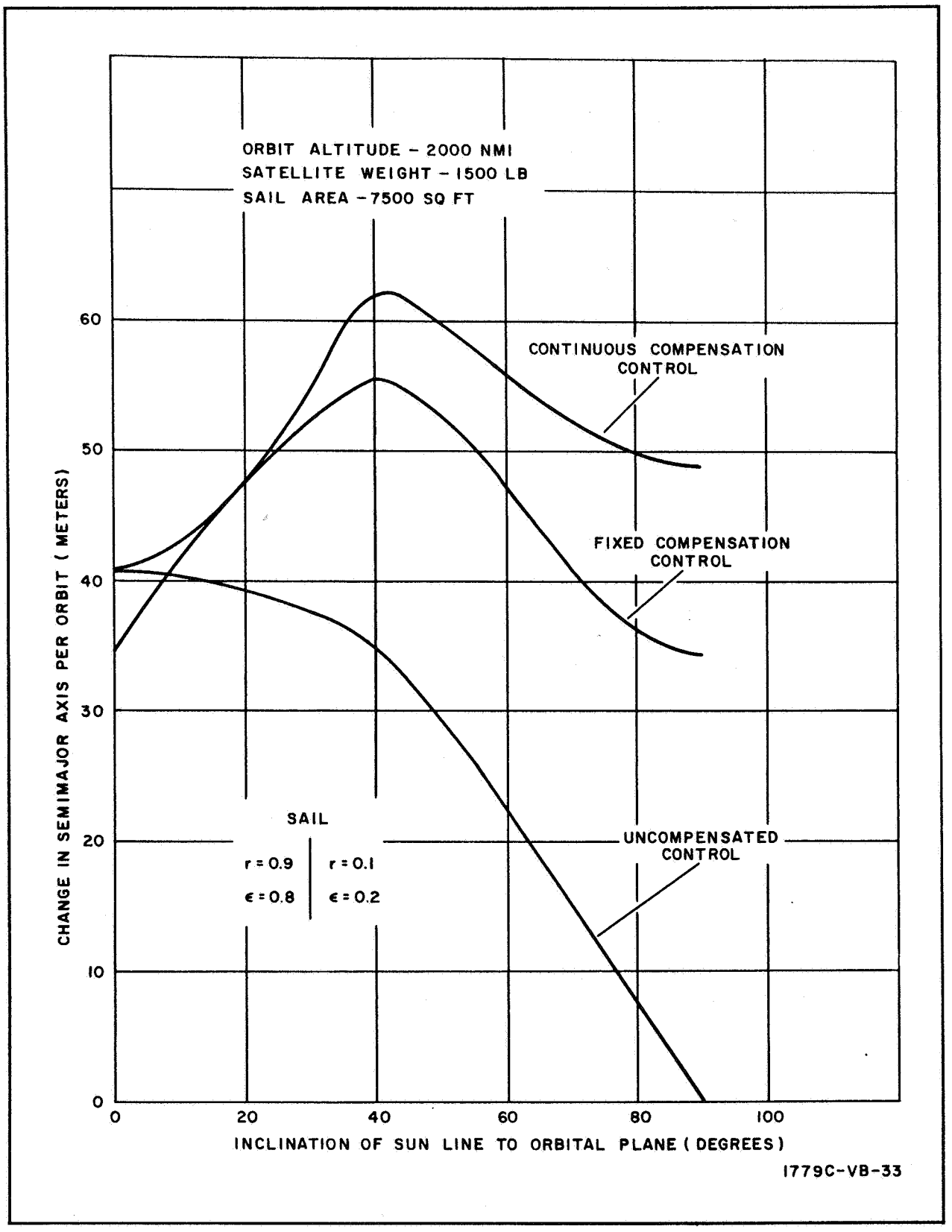

Figure VIII-4. Delta a's for Various Sail Control Procedures

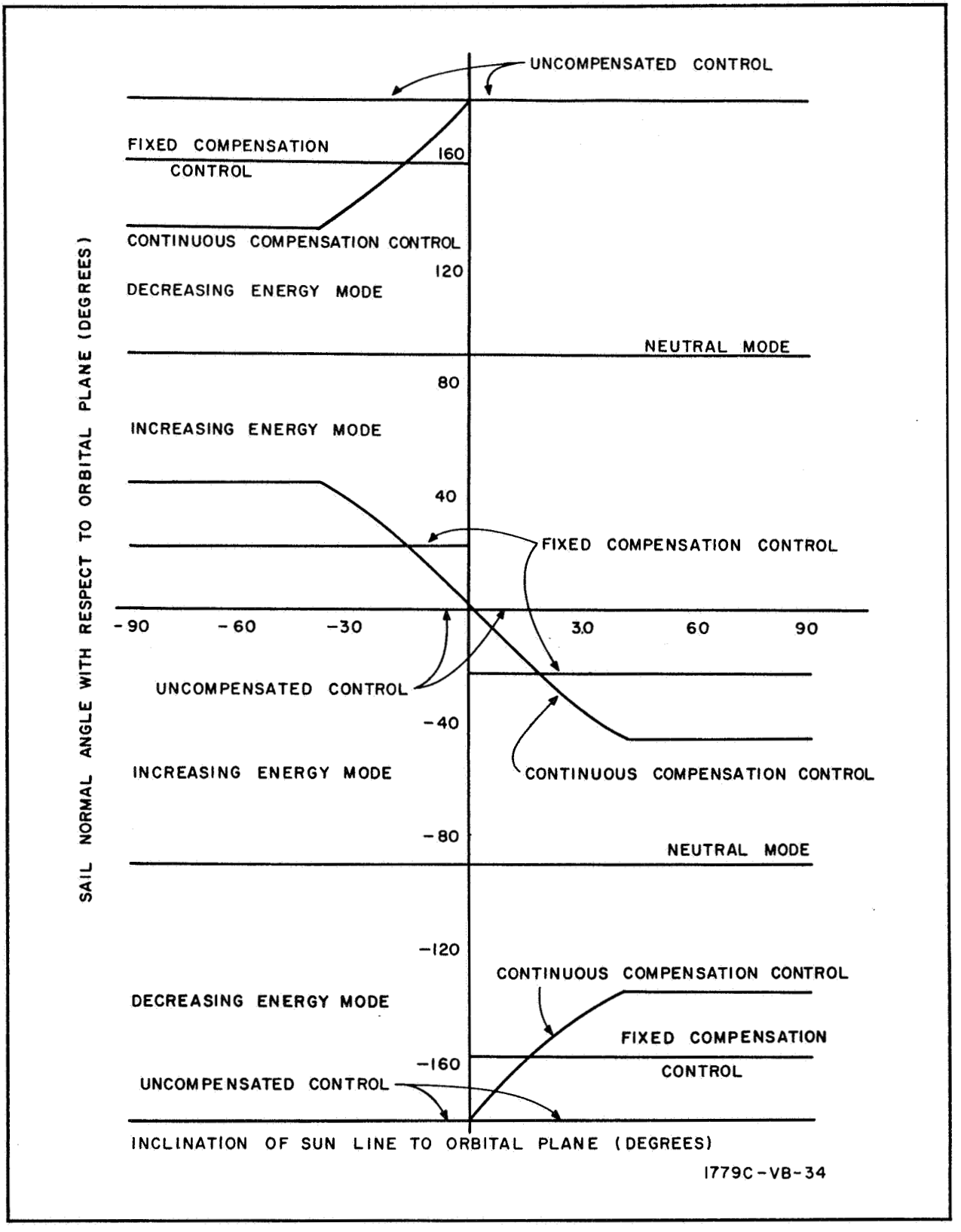

Figure VIII-5. Sail Angle Settings for Various Control Procedures

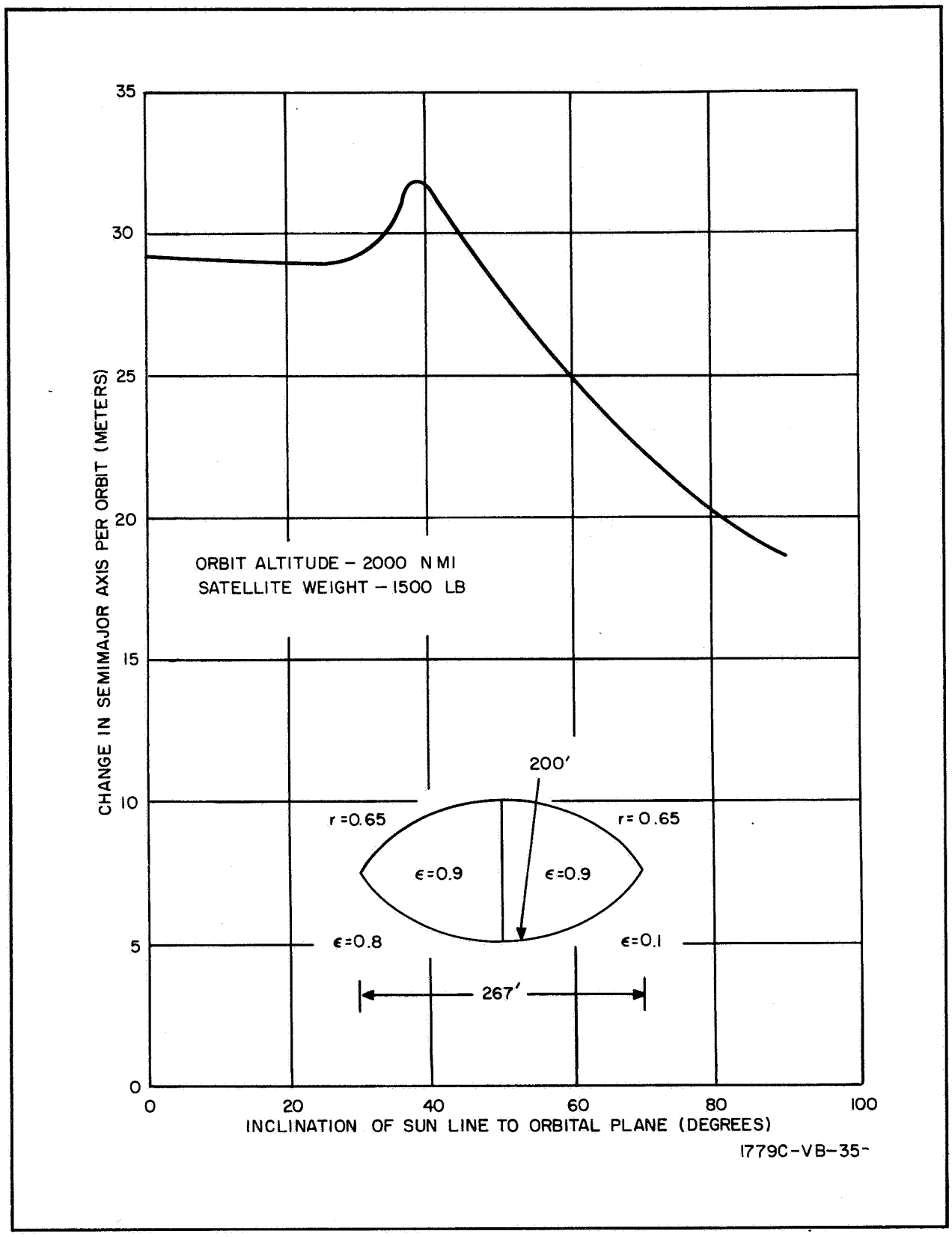

Figure VIII-6. Delta a Curve for Opaque Lens

In order that the relative capabilities of the various configurations could be compared more accurately, the distribution of sun line inclinations was calculated for several orbital inclinations at the 2000-nautical-mile altitude of the study. The calculation was made through the use of a modification to the Lifetime 18 orbital prediction program. At the end of each day, the sun line inclination was calculated and its value noted to the nearest 5 degrees. At the end of the run, the precentage of time that each 5-degree increment was observed was calculated by simply taking the ratio of the number of days that sun line inclination occurred to the total number of days.

Figure VIII-7 shows the results of these calculations for 45-, 60-, and 75-degree orbits. The figures were calculated by running the particular orbits through the Lifetime 18 program for a period of 20 years so as to ensure a more random phasing of the separately varying quantities which cause the sun line inclination variations.

The sun line inclinations vary as a function of both the precession of the right ascension along with the apparent motion of the sun around the earth and with the apparent motion of the sun in and out of the plane of the equator. The first of these, standing alone, would cause a sinusoidal variation in the sun line inclination of amplitude equal to the inclination of the orbit, while the latter would cause a sinusoidal variation of approximately 23 degrees in magnitude. It should be noted that the distributions shown in figure VIII-7 can be closely approximated by the distribution of two sine waves of amplitudes equal to 23 degrees and the inclination, respectively, and having a random phase relationship.

If the distributions of figure VIII-7 are applied to the change in semi-major axis curves of figures VIII-4 and VIII-6; that is, if the product of the two curves is taken an average figure for the Δa shown in figure VIII-8 is obtained at each inclination.

If now an average $\overline{\Delta a}$ for each orbit is assumed to be the Δa which acts on the satellite at all times, an average mobility can be calculated by the following relationships:

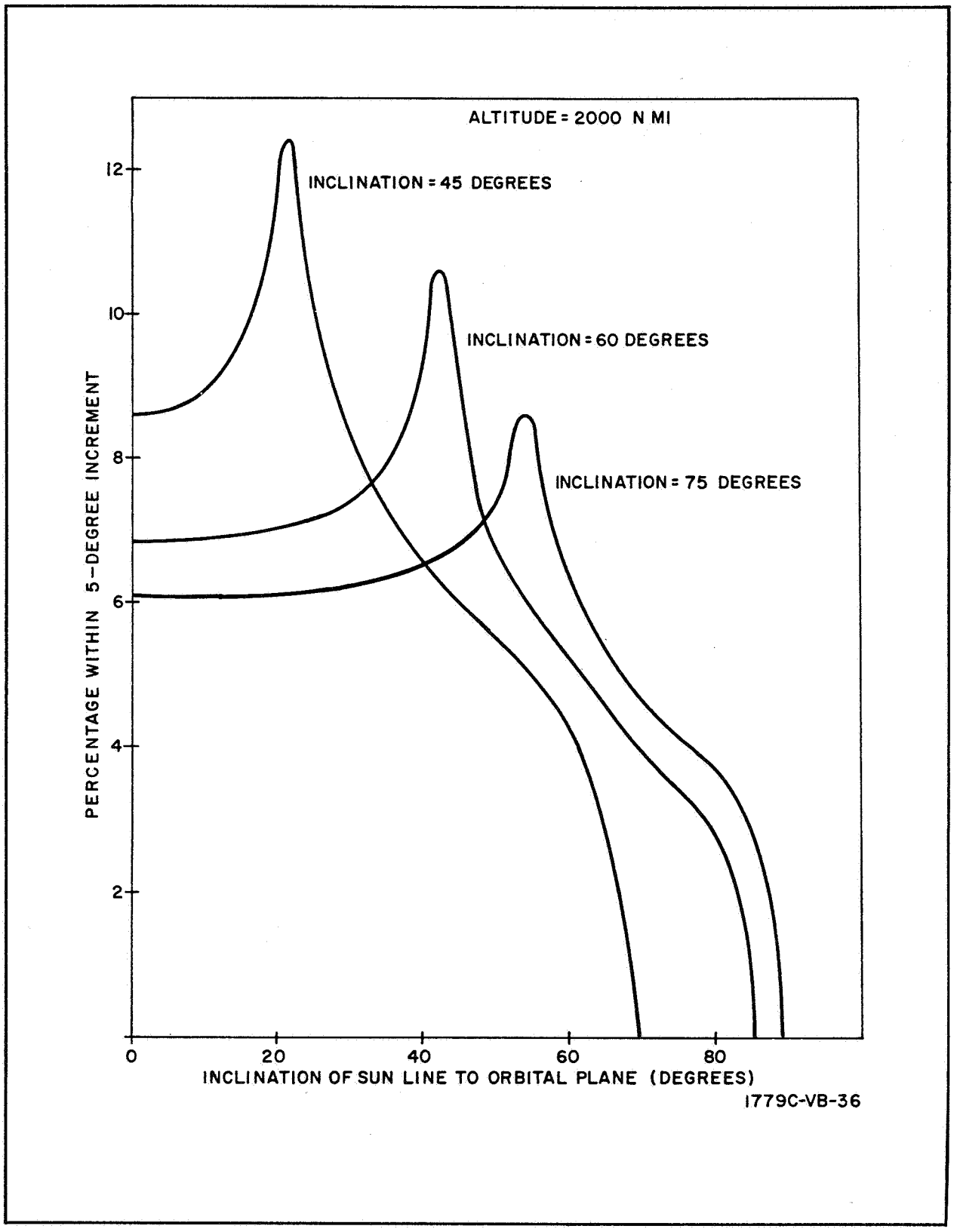

Figure VIII-7. Distribution of Sun Line Inclinations

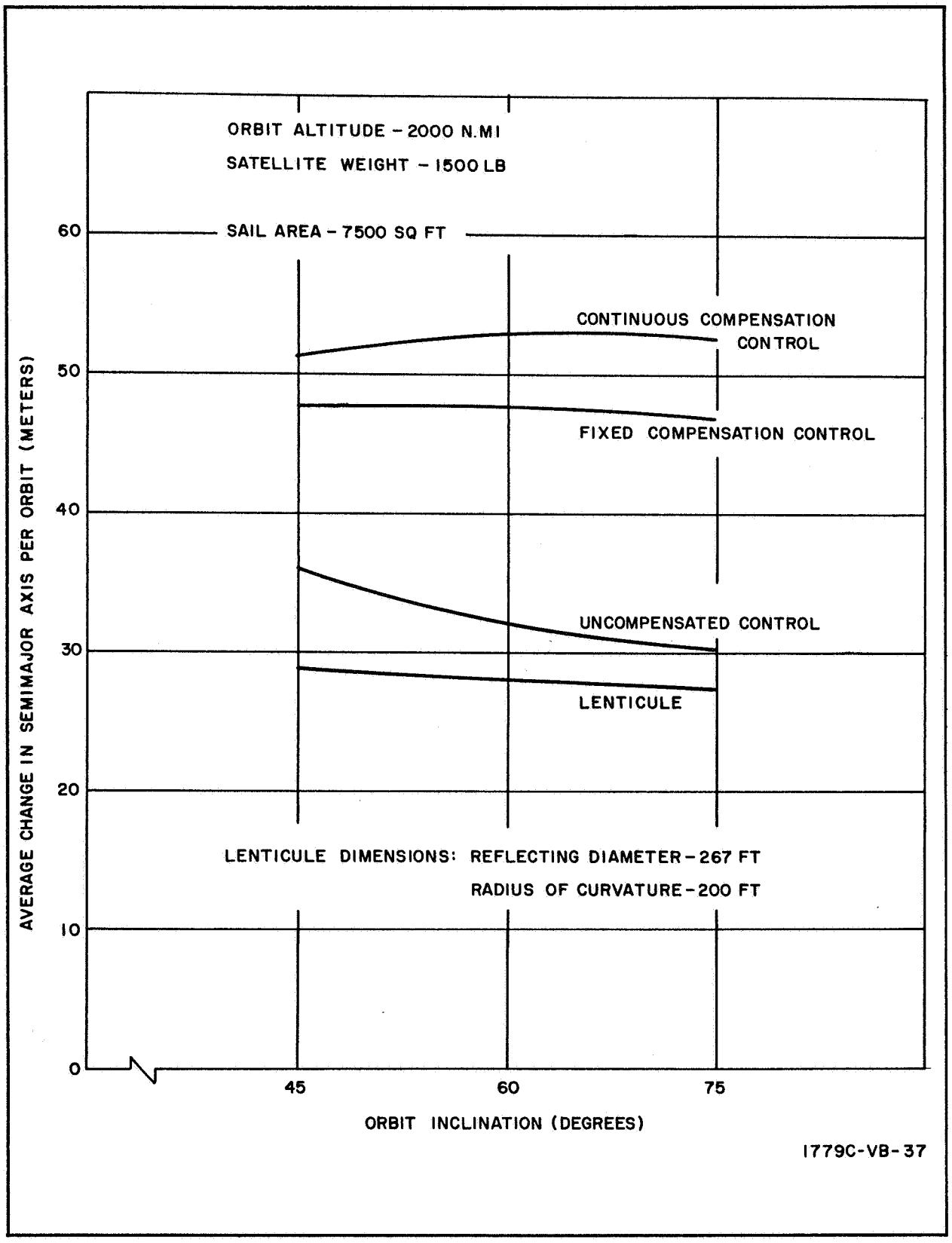

Figure VIII-8. Average Delta a's for Sail and Lenticule

$$\Delta P_{po} = \frac{2\pi}{K\sqrt{M}} \left[(a + \bar{\Delta}a)^{3/2} - (a - \bar{\Delta}a)^{3/2} \right] \qquad \text{(VIII-3)}$$

where ΔP_{po} represents the period change between the two satellites per orbit, K is the universal gravitational constant, M is the mass of the earth, and a is the semi-major axis of the orbit. Applying the binomial theorem to equation VIII-3, the following relationship is obtained:

$$\Delta P_{po} = \frac{2\pi a^{3/2}}{K\sqrt{M}}$$

The angular separation between the satellites as a function of time or mobility can be shown to be:

$$= \frac{2\pi}{P} N^2 \Delta P_{po}$$

where P is the period of the orbit and N is the number of orbits. When these relationships are applied to the $\bar{\Delta}a$'s of figure VIII-8, the average mobilities shown in figure VIII-9 are obtained.

It will be remembered that mobility in this sense has been defined as the angular separation as a function of time between two identical satellites started in identical orbits but placed in opposite modes of operation. The relative mobilities of the three different sail control techniques are shown clearly on this graph. As can be seen, the fixed compensation and continuous compensation schemes produce considerably more mobility than does the uncompensated schemes. However, it does not appear that the continuous compensation control technique offers nearly a large enough improvement over the fixed compensation scheme to warrant the required complications in the attitude control system. For this reason, the fixed compensation scheme has been chosen for use in the remaining studies.

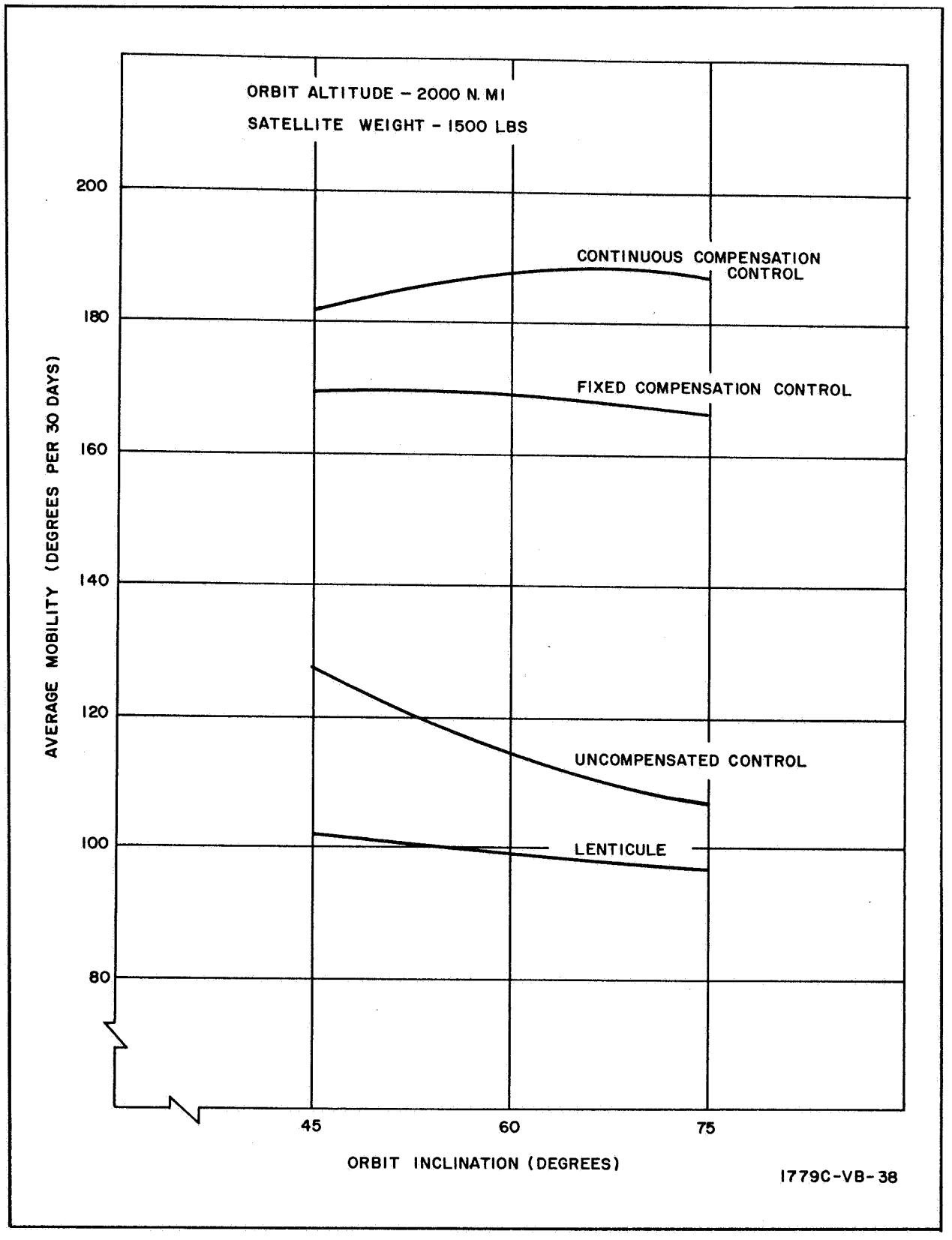

Figure VIII-9. Average Mobilities for Sail and Lenticule

APPENDIX IX

EFFECTS OF ATTITUDE CONTROL ERRORS ON MOBILITY

All the mobility results shown in Appendix VIII for both the lenticule and sail assume an ideal orientation of the satellite. However, the design limitations on the attitude control system may allow as much as a 10-degree angular error on the yaw orientation and 5 degrees on both the roll and pitch axes. Since the angular error on the yaw axis is largest and since this error is easiest to simulate in the mobility program, it has been decided to study the effects of a sinusoidal yaw error on the mobility of the two configurations.

Results of the attitude control study (see attitude control section) have shown that an approximately sinusoidal error of amplitude as large as 10 degrees and a frequency of 1 cycle per 2-1/3 orbits will occur on the configuration A opague lenticule satellite. The same type of yaw angle error will occur on the configuration B sail satellite, but having a maximum amplitude of only 6 degrees.

In order to compare the results for the two configurations, a 10-degree sinusoidal error was also studied for the configuration B satellite. Figure IX-1 shows the effects of this error on the change in semi-major axis per orbit for a portion of the same run used to determine the 60-degree inclination maximum mobility (shown in section entitled "Sail and Lenticule Mobility Study"). The dashed line shows the nominal Δa for a 0 attitude error. The variations from this line show the integral over each orbit of the solar forces (Δa). Since the frequency of the yaw angular error was so high (1 cycle per 2-1/3 orbits), not enough data points were obtained to draw the true smooth sinusoidal variation of Δa, and, hence, straight lines were simply drawn between adjacent points. The outer solid lines define the envelope of variation which the 10-degree sinusoidal error produces. On a different scale, the sun line inclination as a function of time for this particular run is shown.

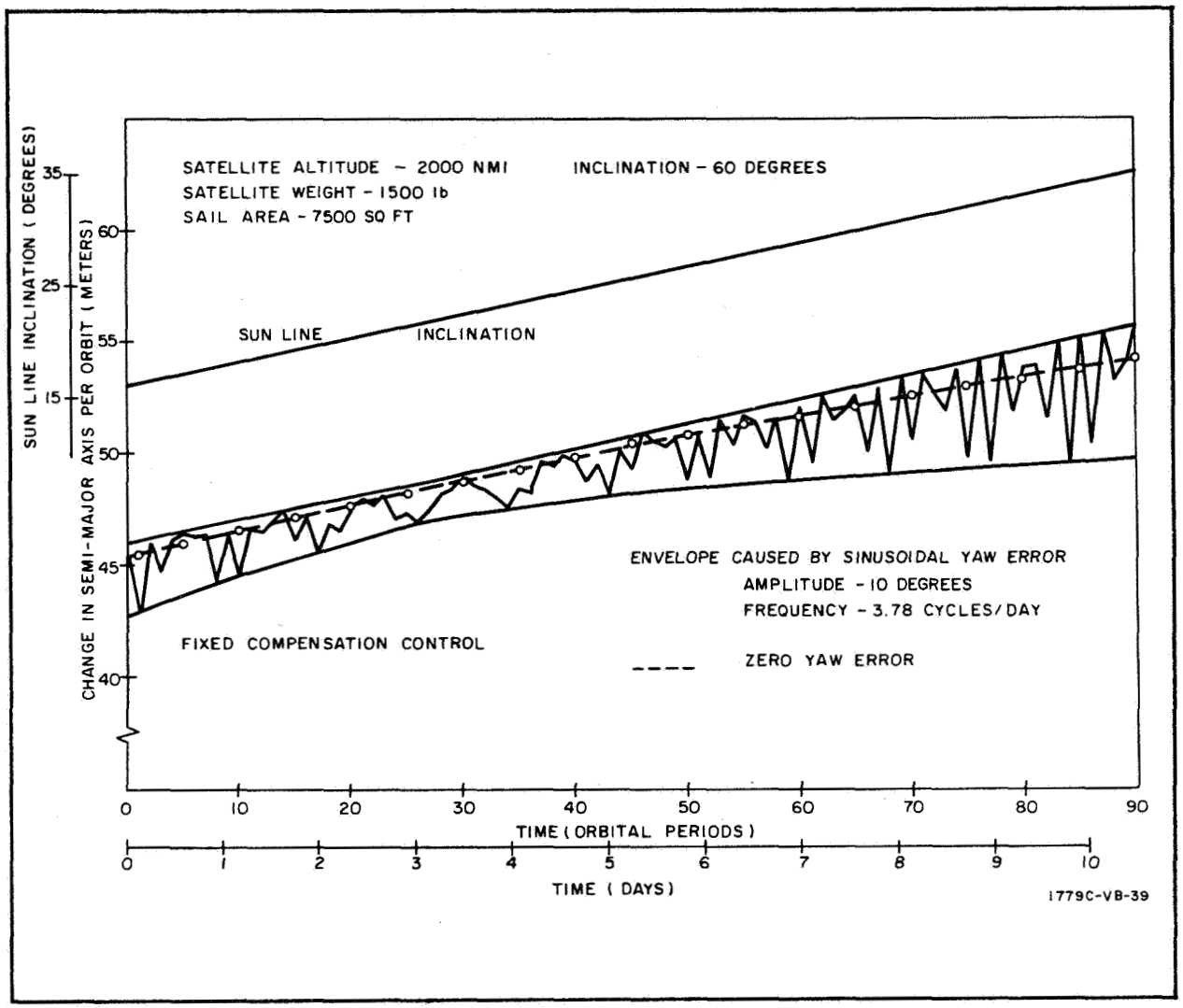

Figure IX-1. Effects of Sinusoidal Yaw Error on the Change in Semimajor Axis Per Orbit of Sail

In order to explain the increasing variation of Δa as a function of time, reference should be made to figure VIII-2. As can be seen at the point where the envelope is narrowest, the sun line inclination is about 20 degrees. For this inclination, the change in semi-major axis for sail angles of 15, 22.5, and 30 degrees are nearly equal; thus, a yaw angular error will cause only a small change in the Δa. Furthermore, the change will be predominately in the negative direction since both the 15- and 30-degree sail angle curves are less than the 22.5-degree curve at that point. After 10 days, the sun line

inclination has increased to about 35 degrees and the 22.5-degree curve lies between the 15- and 30-degree sail angle curves, and the variation due to yaw error is much larger with the 0 error curve being more nearly centered in the envelope.

The mobilities for the same two runs, that is, with no attitude error and with a 10-degree sinusoidal yaw error, differed after 30 days by 1.3 percent. Thus, the 10-degree sinusoidal yaw error has very little effect on the mobility of the sail under the fixed compensation control scheme. This is due partially to the relatively high frequency of the error, but mostly is due to the fact that an error in the attitude of the sail under the fixed compensation control can produce either more or less mobility than the correct attitude and thus the effects of the error are partially averaged out. For the continuous compensation control scheme where the sail is continuously adjusted to produce optimum mobility, the yaw angular errors would cause a somewhat greater degradation of the mobility.

The effects of imposing the same 10-degree sinusoidal yaw error on the opague lens satellite are shown in figure IX-2. As can be seen, the envelope of the variations encloses an area of less than 1 meter per orbit with the variations from the 0 error curve being predominately negative. The rather sharp variations in the 0 error curve itself are believed to be caused by slight errors in the computation of the perturbing forces on the opague lens. These errors are not large enough to show up on a normal sized scale but do become evident on the exaggerated scale of this curve.

The mobility of the lens under the 10-degree sinusoidal yaw error is degraded by only 0.7 percent over a 30-day time period. Thus, again for the opague lens, the effects of attitude control errors on the mobility are seen to be very small.

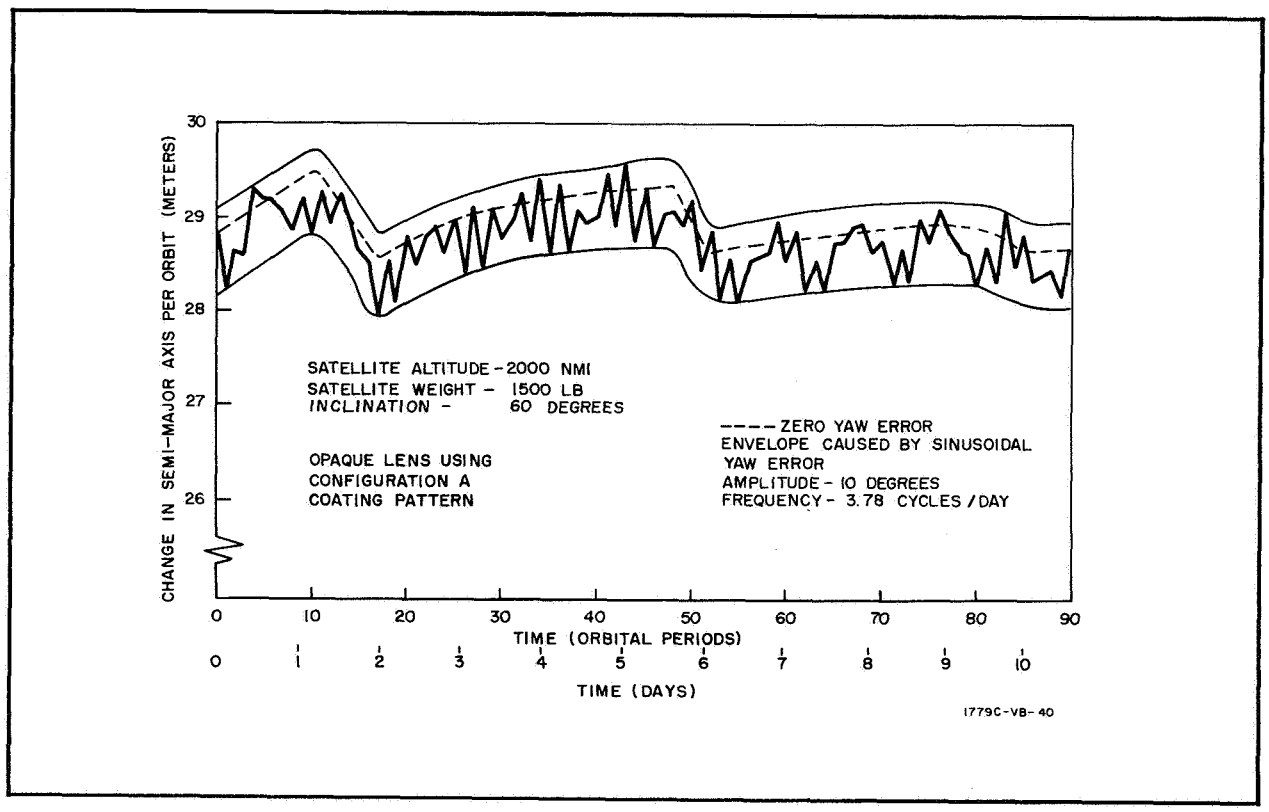

Figure IX-2. Effects of Sinusoidal Yaw Error on the Change in Semi-Major Axis Per Orbit of Lenticule

APPENDIX X

EXTRAPOLATION OF MOBILITY WITH RESPECT TO ALTITUDE

The mobility calculations on the two configuration satellites have been made in detail at one altitude only (2000 nautical miles). This appendix describes the general manner in which the mobility varies as a function of the orbital altitude and shows estimates of mobility based upon extrapolated lenticular configurations designed for other altitudes.

Previous studies on both spherical and lenticular configurations have shown that if the same satellite is placed at two different altitudes, the mobility will be inversely proportional to the semi-major axis of the orbit. Similarly, the change in semi-major axis per orbit or Δa of the satellites has been observed to be directly proportional to the square of the period of the orbit. Furthermore, it has been observed in comparing the mobilities of the lenticule and sphere having the same coating pattern that the mobility is directly proportional to the projected area of the lenticule (sphere) in a radial plane and inversely proportional to the weight of the satellite.

Thus the mobility can be estimated as a function of the extrapolated dimensions and weights of the lenticule at various altitudes. The detailed calculations which have been made on the lenticule at 2000 nautical miles have been used as the basis of this estimate. Shown in table X-1 are the dimensions, weights, and other pertinent quantities for the altitudes examined. The mobilities shown in this table are based upon the 60-degree-inclination average mobility calculated for the lenticule at 2000 nautical miles (see Appendix VIII). Figure X-1 shows these mobilities plotted as a function of altitude. As can be seen, the mobility decreases as a function of altitude due to both the decreased area-to-mass ratio of the satellite and the inverse relationship with respect to the semi-major axis.

Table X-1

LENTICULE DIMENSIONS, WEIGHT, AND MOBILITY
AS FUNCTION OF ALTITUDE

Altitude (nmi)	Radius of Curvature (feet)	Rim Diameter (feet)	Projected Area in Radial Plane (sq ft)	Weight (lb)	Area to Mass (ft^2/lb)	Estimated Mobility (deg/ 30 days)
1000	91.3	147	7760	463	16.75	125
2000	200	267	18700	1152	16.25	99
4000	412	400	28800	2232	12.9	57
6000	918	604	40000	3452	11.6	41

The change in semi-major axis per orbit and the mobility of the sail can be shown to vary in a manner similar to that of the lenticule. Thus, for a constant area-to-mass ratio sail satellite, the mobility will essentially vary as the inverse of the semi-major axis, while the change in semi-major axis will be directly proportional to the square of the period of the orbit. For a satellite using a sail as the orbit position control means, the mobility can also be assumed to be directly proportional to the area-to-mass ratio. This neglects the effects of the earth shadow angle on the mobility, but this effect should be very small above 1000 nautical miles.

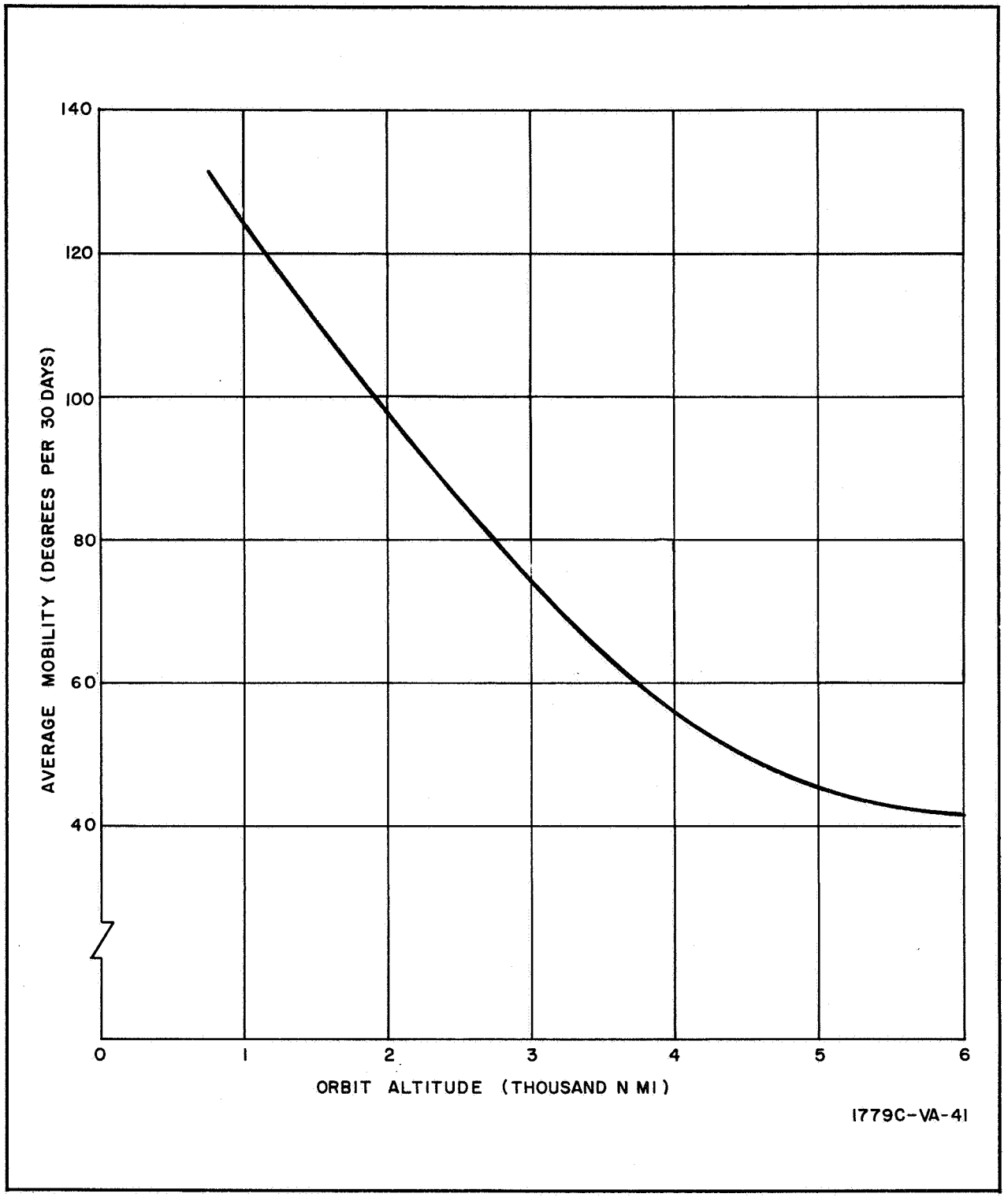

Figure X-1. Lenticular Mobility as a Function of Altitude

APPENDIX XI

STRUCTURAL ANALYSIS OF EXTENDIBLE BOOMS FOR A GRAVITY-GRADIENT STABILIZED SATELLITE

Introduction

Both yaw and damper rods for the torque-boom system of satellite attitude control and damping consist of unfurlable beryllium copper tubes. The use of long overlapping split tubes requires an analysis of the deflection produced by both gravity gradient forces and thermal bending. In addition to producing rod deflections, thermal bending and gravity gradient forces may combine to apply a torsional moment to the rod. Each of these problems is treated separately in this analysis and the general equations for deflection, solar bending, and torque are presented. As a summary, three rod sizes are compared as yaw and damper rods for use with the symmetrical and asymmetrical satellite on the basis of maximum deflection, torsional moment, and safety factor.

Thermal Bending

Sun light incident on tubular rods in space acts to produce a thermal gradient between that side of the rod on which the energy is incident and that side which faces black space. The temperature gradient across the rod diameter may be expressed as follows:[1]

$$\Delta T = \frac{d^2 R_s \alpha_s}{4Kt} \qquad \text{(XI-1)}$$

Since the solar absorptivity α_s of beryllium copper is high and causes large thermal gradients, the use of a silver alloy or the application of silver plating to the BeCu rods has been considered.[2, 3] The application of a 0.0002-inch thick silver plating can be expected to reduce the solar absorptivity to 0.1. The temperature gradient given by equation XI-1 can be considered as a uniform thermal moment, M_t, defined as follows.

A constrained rod subjected to a uniform thermal gradient ΔT across its diameter has a maximum tensile or compressive outer fiber stress given by

$$\sigma = \epsilon \ E = C_T \left(\frac{\Delta T}{2}\right) E \qquad \text{(XI-2)}$$

The "thermal moment" corresponding to this stress is

$$M_t = \frac{\sigma I}{d/2} = \frac{2 \sigma I}{d} \qquad \text{(XI-2a)}$$

Substituting equation XI-2 into XI-2a yields

$$M_t = \frac{C_T \Delta R \ EI}{d} \qquad \text{(XI-2b)}$$

Combining equations XI-1 and XI-2b with the equation for tip deflection of a cantilever beam under a uniformly applied moment, $\delta = Ml^2/2EI$, yields

$$s = \frac{C_T \alpha_s R_s l^2}{8K} \left(\frac{d}{t}\right) \qquad \text{(XI-3)}$$

The following substitutions can be made for a 200-foot rod length:

$l = 2.4\ (10)^3$ inches $\qquad$ $(d/t) = 225$ (minimum for BeCu rods)

$C_T = 9.3\ (10)^{-6}$ in./in. $\qquad$ $\alpha_s = 0.10$

$R_s = 450$ Btu/ft^2-hr $\qquad$ $K = 900$ Btu-in./hr-ft^2-°F

This results in a deflection of the rod tip of $\delta_s = 75$ inches. It should be noted that since the diameter to thickness ratio is fixed by the selection of material, the deflection produced by solar bending will be independent of rod diameter.

Applied Loads

The loads applied to the satellite rods are produced by gravity gradient and rotation of the satellite about its own center of mass. Both of these loads are proportional to the mass of the rod and its height above the satellite center of mass (CM). For the calculation of rod forces, the tip mass plus half the rod mass is considered concentrated at the rod tip. This simplifying assumption gives correct values for the maximum bending moment; however, it yields slightly higher than actual values for the maximum torsional moment and

the rod tip deflection. It has been shown that actual values of torsional moment and tip deflection are within 15 percent of those given in this report. The height above satellite CM is assumed to be 400 feet for the symmetrical configuration and 275 feet for the asymmetrical as shown in figure XI-1.

The three rod sizes considered in this study are:

Diameter (in.)	Thickness (in.)	Weight per 200 ft (lb)
1.125	0.005	19.2
0.90	0.004	12.4
0.675	0.003	7.0

For a yaw tip weight of 16 pounds and a damper tip weight of 8 pounds, the following maximum normal and axial compressive loads have been calculated:

Symmetrical Satellite Yaw Rod

	1.125 Diameter	0.90 Diameter	0.675 Diameter
normal load, F_n (lb)	$3.9\ (10)^{-4}$	$3.4\ (10)^{-4}$	$3.0\ (10)^{-4}$
axial compression, F_c (lb)	$1.4\ (10)^{-5}$	$1.2\ (10)^{-5}$	$1.1\ (10)^{-5}$

Symmetrical Satellite Damper Rod

	1.125 Diameter	0.90 Diameter	0.675 Diameter
normal load, F_n (lb)	$2.7\ (10)^{-4}$	$2.2\ (10)^{-4}$	$1.8\ (10)^{-4}$
axial compression, F_c (lb)	$1.0\ (10)^{-5}$	$0.8\ (10)^{-5}$	$0.7\ (10)^{-5}$

Asymmetrical Satellite Yaw Rod

	1.125 Diameter	0.90 Diameter	0.675 Diameter
normal load, F_n (lb)	$2.76\ (10)^{-4}$	$2.4\ (10)^{-4}$	$2.1\ (10)^{-4}$
axial compression, F_c (lb)	0	0	0

Asymmetrical Satellite Damper Rod

	1.125 Diameter	0.90 Diameter	0.675 Diameter
normal load, F_n (lb)	$1.9\ (10)^{-4}$	$1.6\ (10)^{-4}$	$1.3\ (10)^{-4}$
axial compression, F_c (lb)	0	0	0

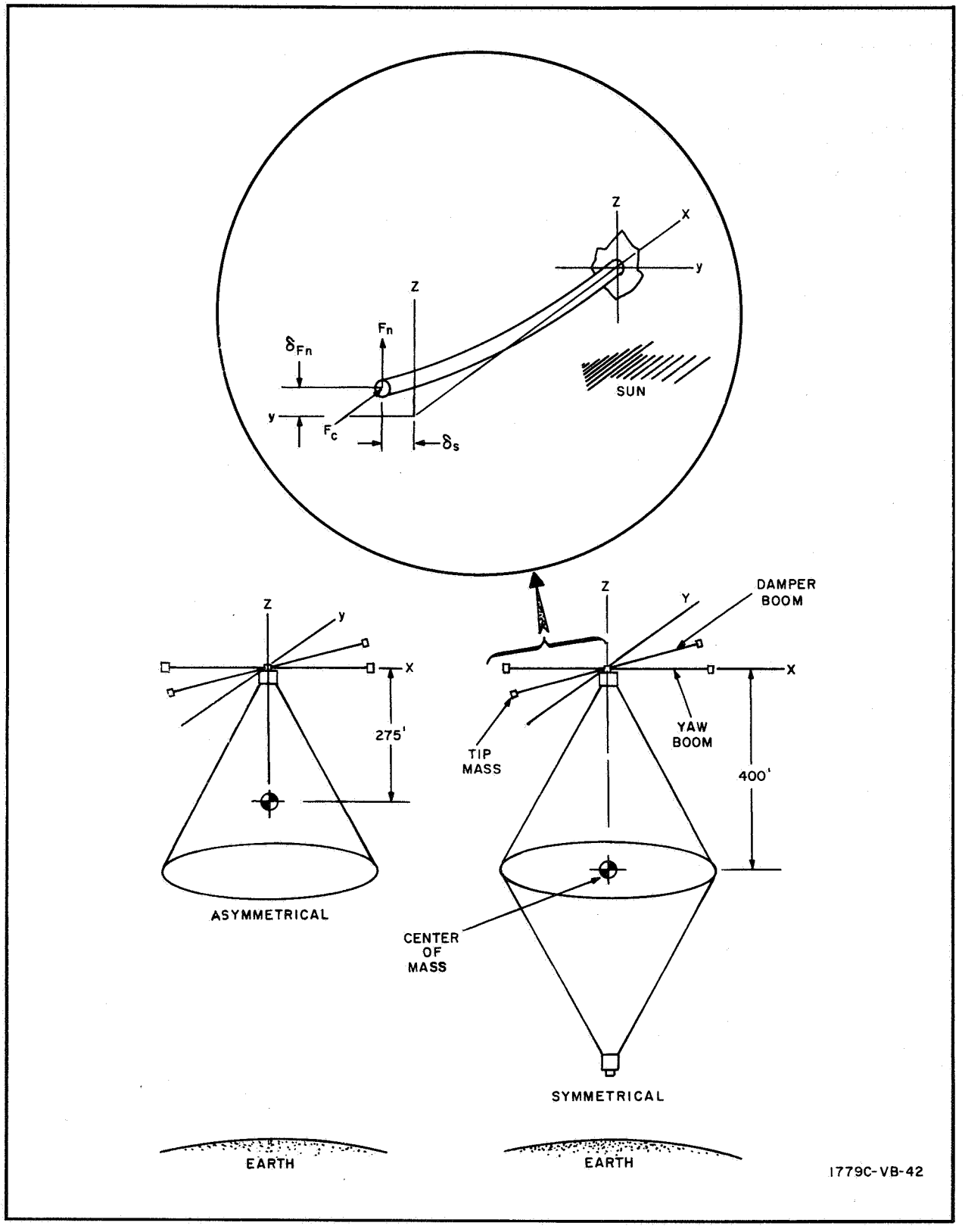

Figure XI-1. Satellite Configurations and Boom Loads

Determination of EI for an Overlapped Tube - The theoretical area moment of inertia for a thin-walled tube is proportional to r^3t where r = tube radius and t = thickness. The effective moment of inertia for a 160-degree overlapped tube construction has been determined by a test program conducted under NASA Contract NAS 7-234 for the Ames Research Center.[4] In this program, two 0.45-inch diameter tubes fabricated from 2-mil BeCu were loaded and the effective bending stiffness, EI, measured. The results of this test indicate an average EI = 1870 lb-in.^{2}. Solving for the coefficient, A, of r^3t we find,

$AEr^3t = EI\ experimental^1 = 1870\ lb\text{-}in.^2$

$E = 19 \times 10^6$ psi

$r = 0.225$ in.

$t = 0.002$ in.

$$A = \frac{(1870)}{2.28\ (10)^{-5} \times 19\ (10)^6} = 4.3$$

Work performed under the above-mentioned contract has shown that at an overlap angle of 160 degrees, the area moment of inertia is equal about the axis of symmetry and an axis normal to it (i.e., principal axes). Under such conditions, the bending stiffness EI is equal about any axis of the tube, and as previously shown, is expressed as

$$EI = 4.3\ Er^3t \qquad \text{(XI-4)}$$

Assuming a modulus of elasticity, E, for beryllium copper of 19×10^6 psi, the value of EI for each rod size is given below.

Rod Diameter (in.)	Thickness (in.)	EI (lb-in.^{2})
1.125	0.005	$72.0\ (10)^3$
0.900	0.004	$29.8\ (10)^3$
0.675	0.003	$9.5\ (10)^3$

Deflections Due to Normal Forces - The deflection of a cantilever beam produced by a concentrated normal load applied at the tip is given by the following equation:

$$\delta = \frac{F_n l^3}{3EI} \qquad \text{(XI-5)}$$

For the 1.125-inch tube, the calculation of lateral tip deflection using equation XI-5 is

$$\delta_{FN} = \frac{3.9\,(10)^{-4} \times \left[2.4\,(10)^3\right]^3}{3 \times 72\,(10)^3} = 25 \text{ inches}$$

Deflections Due to Compressive Forces - Lateral deflection is also produced by the axial compressive load, F_c, and is calculated as follows:

$$\delta_{FC} = \frac{e\,(1 - \cos pl)}{\cos pl} \quad \text{(ref. 5)} \qquad \text{(XI-6)}$$

where

$$p = \sqrt{\frac{F_c}{EI}} \quad \text{(ref. 6)} \qquad \text{(XI-7)}$$

The maximum e is found by assuming the lateral deflection due to the normal load in the same direction as the bending produced by the thermal gradient. This gives a value of e of 75 + 25 = 100 inches. Substituting

$$p = \sqrt{\frac{1.4\,(10)^{-5}}{72\,(10)^3}} = 0.14\,(10)^{-4}$$

$$pl = 0.14\,(10)^{-4} \times 2.4\,(10)^3 = 0.0336$$

$$\delta_{FC} = \frac{100\,(1 - \cos\,(0.0336))}{\cos\,(0.0336)} = 0.05 \text{ inch}$$

The largest deflection due to axial compressive loading occurs for the 0.675-inch diameter rod. The compressive load from Section 3 (1.1×10^{-5} lb) gives a deflection of less than 1 inch (0.73 inch). Because of these small values, the deflection due to the compressive forces will be neglected.

Total Deflections - The maximum total deflection produced by combined solar bending and concentrated loads is

$$\delta_T = \delta_s + \delta_{FN} = 75 + 25 = 100 \text{ inches}$$

for the 1.125-inch diameter rod.

Bending Moment

Moment due to normal load

$$M_{BFn} = F_n l$$
$$= 3.9\,(10)^{-4} \times 2.4\,(10)^{3}$$
$$= 0.94 \text{ in.-lb}$$

Moment due to axial compressive load

$$M_{BFc} = F_c e = F_c\,(\delta_s + \delta_{FN})$$
$$= 1.4\,(10)^{-5} \times 100$$
$$= 1.4 \times 10^{-3} \text{ (negligible)}$$

Critical bending moment

The equation for the critical bending moment of split overlapped tubes as given by DeHavilland Aircraft of Canada Limited is

$$M_{Bcr} = \frac{0.042\,(12)\,K_b\,Edt^2}{F_b\,(1 - \upsilon^2)} \qquad \text{(ref. 7)} \qquad \text{(XI-8)}$$

For the 1.125-inch diameter rod, the critical bending moment is

$$M_{Bcr} = \frac{0.042\,(12)\,(0.75)\,19\,(10)^6\,(1.125)\,(0.005)^2}{1.3\,(1 - 0.09)} = 170.4 \text{ in.-lb}$$

To give some confidence in the result given by equation XI-8, another expression for the critical bending moment is derived as follows. The critical bending buckling stress for thin-walled seamless tubes is given by

$$\sigma_{cr} = K_{BU}\,E \qquad \text{(ref. 8)} \qquad \text{(XI-9)}$$

where K_{BU} is the buckling constant depending on the r/t ratio.[9]

The maximum compressive stress in bending is given by the familiar

$$\sigma = \frac{Mc}{I} \qquad \text{(XI-10)}$$

Combining equations XI-9 and XI-10 and substituting M_{Bcr} for M, r for C, and $\pi r^3 t$ for I, yields

$$M_{Bcr} = \frac{\pi r^2 t K_{BU} E}{F_b} \qquad \text{(XI-11)}$$

Substituting the values for the 1.125-inch rod and using the same DeHavilland safety factor gives

$$K_{BU} = 0.0026 \text{ for } \frac{r}{t} = \frac{0.56}{0.005} = 112$$

$$M_{Bcr} = \frac{\pi (0.56)^2 (0.005) (0.0026) 19 (10)^6}{1.3} \quad 187 \text{ in.-lb}$$

The result given by equation XI-11 is 10-percent higher than the result given by equation XI-8. Therefore, the DeHavilland equation will be used for the design. The maximum applied moment and critical moment are presented in table XI-1 for all tube sizes considered. It is apparent that the applied bending moment is in no case a significant percentage of the allowable bending moment.

Torsional Moment

Torsional Loading - In order to illustrate the mechanism of rod torsion, the following combination of thermal bending and gravity gradient forces will be considered. As shown in figure XI-1, the gravity gradient forces acting on the rod and its tip mass are always directed away from the earth. If the axis of solar bending is assumed to be perpendicular to these forces, it can be seen that a torsional moment is created whose maximum magnitude is the product of the gravity gradient force and the maximum rod tip deflection. The application of this torque will cause rotation of the overlapped tube with its low torsional rigidity.

If a rod were permanently bowed by the thermal gradient, it would slowly rotate 90 degrees and come to rest with the torsional moment arm having been reduced to zero. Such is not the case however, since as the rod rotates, a new surface is exposed to the sun and the moment arm is re-established. It follows that a slow twisting of the rod results and will continue until the rod has developed sufficient spring torque to balance the external torque.

As stated, the worst possible moment will be produced when the maximum normal force acts perpendicular to the maximum thermal deflection of the rod. Therefore, the 1.125-inch diameter rod,

$$\text{Max } M_T = F_N (\delta_s) = 3.9\ (10)^{-4} \times 75 = 0.029 \text{ in.-lb}$$

Critical Torsional Moment - The equation for the critical torsional moment of split thin-walled tubes as given by DeHavilland Aircraft of Canada Limited is

$$M_{Tcr} = \frac{K_t E\, t^3}{F_t (1 - \upsilon^2)^{0.75}} \sqrt{\frac{t}{d}} \qquad \text{(ref. 10)} \qquad \text{(XI-12)}$$

Substituting the values for the 1.125-inch diameter rod yields

$$M_{Tcr} = \frac{(0.75)\ 19\ (10)^6\ (0.005)^3}{(1.3)\ (1 - 0.09)^{0.75}} \sqrt{\frac{5 \times 10^{-3}}{1.12}}$$

or

$$M_{Tcr} = 0.0975 \text{ in.-lb}$$

The deviation of equation XI-12 is considered DeHavilland Company proprietary information. To give some confidence in the results indicated by the equation, an expression was also developed for this critical torque by Westinghouse. It will be seen that the Westinghouse equation gives values of critical torque which are in close agreement with the DeHavilland equation for the tube sizes considered. The expression for critical torque is derived as follows:

The critical buckling shear stress for long curved panels in uniform shear is given by

$$\tau_{cr} = 1.67\, E \frac{t}{d} \sqrt{\frac{t}{r}} \sqrt{1 + 68.7\, \frac{r^2 t^2}{b^4}} \qquad \text{(ref. 11)} \qquad \text{(XI-13)}$$

where Poisson's ratio (υ) is assumed to be 0.3. This is shown in figure XI-2a. The distribution of shear stress in a torqued open tube is shown in figure XI-2b. It increases from zero at the open end to a maximum at 180 degrees from the split end. The maximum shear stress as a function of the torsional moment is given by

$$\tau_{max} = \frac{M_T\,(6\pi r + 1.8t)}{4\pi^2 r^2 t^2} \qquad \text{(ref. 12)} \qquad \text{(XI-14)}$$

This expression assumes the thickness (t) small compared with the mean radius which is correct for the tube sizes under consideration.

By equating τ_{max} of equation XI-14 to τ_{cr} of equation XI-13 we can arrive at an expression for TM_{cr}. This assumption is conservative as the maximum shear stress in the open tube could be higher to simulate an "equivalent" uniform shear. This is indicated in figure XI-2c. However, actual buckling usually occurs at a value less than the theoretical, thus justifying the conservative assumption.

Consideration of the small values of r and t and substitution of $(2\pi r)$ for (b) reduces equation XI-13 to:

$$\tau_{cr} = \frac{1.67\, E}{2\pi} \frac{t}{r} \sqrt{\frac{t}{r}} \qquad \text{(XI-15)}$$

By the same reasoning, equation XI-14 reduces to:

$$\tau_{max} = \frac{3\, TM}{2\pi r\, t^2} \qquad \text{(XI-16)}$$

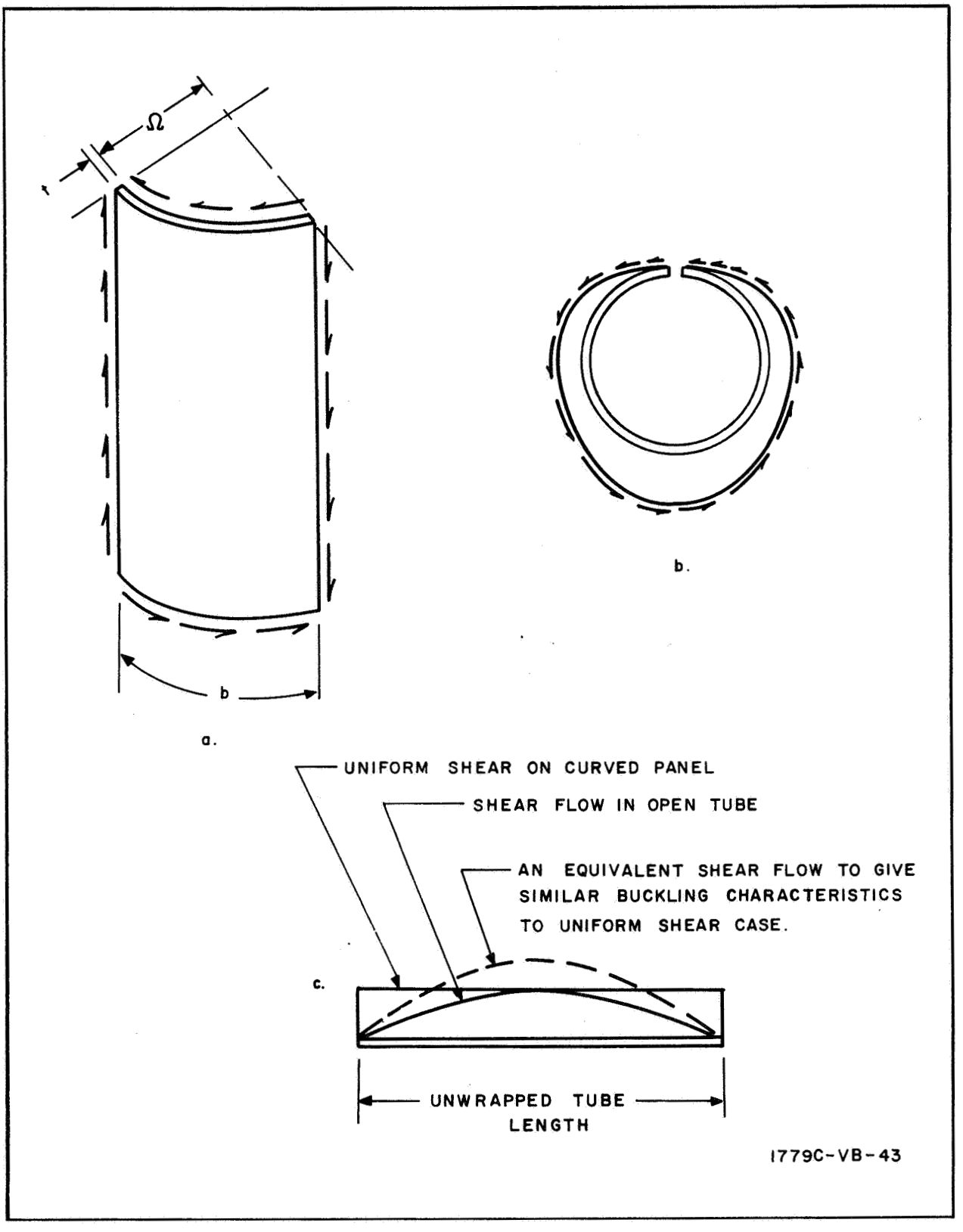

Figure XI-2. Shear Flow in Curved Panels

Combining equations XI-15 and XI-16 and adding a safety factor, the critical torsional moment becomes,

$$M_{Tcr} = \frac{0.556}{F_t} \quad Et^3 \sqrt{\frac{t}{r}} \qquad \text{(XI-17)}$$

Using the DeHavilland safety factor ($F_t = 1.3$) equation XI-1 becomes:

$$M_{Tcr} = 0.428 \; Et^3 \quad \sqrt{\frac{t}{r}} \qquad \text{(XI-18)}$$

Substituting the values for the 1.125-inch diameter rod gives

$$M_{Tcr} = 0.428 \; (19) \; 10^6 \; (0.005)^3 \quad \sqrt{\frac{5 \times 10^{-3}}{0.56}}$$

or

$$M_{Tcr} = 0.096 \text{ in.-lb}$$

Since equation XI-18 gives approximately the same results as equation XI-12, equation XI-12 will be used for determining the critical torque. The values of maximum applied torque and critical torque are presented in table XI-1 for the three rods studied.

Twist Angle - As previously discussed, the application of torsional loads produced twisting of the satellite rods. If the applied torque is of sufficient duration, a rod will twist through an angle θ, such that the torsional moment developed in the rod exactly balances the applied torque. It will be shown that due to the low torsional rigidity of an overlapped tube, θ will be a number of revolutions rather than degrees.

- Equations

The general expression for angular twist of a rod with length, L, under an applied torsional moment, M_T, is

$$\theta = \frac{M_T L}{C} \qquad \text{(XI-19)}$$

The quantity C in the above expression is the torsional rigidity of the rod, JG. It is related to both the physical characteristics of the rod and the end

constraints during twist. For an overlapped tube with no end constraints J is given by reference 12 as,

$$J = \frac{2}{3}\,\gamma\,\pi\,r\,t^3 = \frac{1}{3}\,\gamma\,\pi\,d\,t^3$$

and

$$G = \frac{E}{2\,(1+\upsilon)}$$

$$C = JG = \frac{\gamma\,\pi\,d\,t^3\,E}{6\,(1+\upsilon)} \qquad \text{(XI-20)}$$

Tests of overlapped tubes conducted by the DeHavilland Aircraft Company have shown that the torsional rigidity is most nearly approximated by the following equation which assumes warping to be prevented at one end only. The derivation of this equation is outlined in reference 13.

$$C' = \frac{C}{\left(1 - \frac{a}{L}\,\tanh\frac{L}{a}\right)} \qquad \text{(XI-21)}$$

where a, for an overlapped circular tube is

$$a = \frac{d^2\,\gamma\,\pi\,\sqrt{1+\upsilon}}{2\,\sqrt{2\,t}} \qquad \text{(ref. 14)} \qquad \text{(XI-22)}$$

For long tubes such as are being considered here, $\tanh L/a \approx 1$, and C' may be written as

$$C' = \frac{C}{\left(1 - \frac{a}{L}\right)} \qquad \text{(XI-23)}$$

Thus, combining equations XI-19, XI-20, and XI-23 for twisting of a rod constrained at one end yields the following formula:

$$\theta = \frac{6M\,(L-a)\,(1+\upsilon)}{\gamma\,E\,\pi\,d\,t^3} \qquad \text{(XI-24)}$$

- Yaw Rod Twist

Applying the equations for twist angle to the 1.125-inch diameter rod gives the following results:

$$a = \frac{(1.125)^2\,(1.445)\,\pi\,\sqrt{1.3}}{(2\,\sqrt{2})\,(5 \times 10^{-3})} = 460 \text{ inches}$$

θ_m = twist due to maximum torsional load of (0.029 in.-lb)

$$\theta_m = \frac{6\,(0.029)\,(2400 - 460)\,(1.3)}{(1.445)\,(19 \times 10^6)\,\pi\,(1.125)\,(5 \times 10^{-3})^3} = 36.2 \text{ radians}$$

$$= 5.8 \text{ revolutions}$$

By comparison, the θ corresponding to critical torque would be

$$\theta_{cr} = \theta_m \frac{M_{Tcr}}{M_T} = 5.8\left(\frac{0.098}{0.029}\right) = 19.7 \text{ revolutions}$$

The values of θ resulting from the applied maximum torques are presented in the summary tables for the configurations and rod sizes studied.

Combined Loading

The problem of combined bending and torsional stresses in split overlapped tubes becomes very complex. For the present investigation, it was decided to use the combined stress equation for a thin seamless tube with an appropriate safety factor. This assumption is reasonable as the stresses due to the bending loads are very small compared to the critical load. The combined equation is

$$\left(\frac{M_B}{M_{Bcr}}\right)^2 + \left(\frac{M_T}{M_{Tcr}}\right)^2 = 1.0 \quad \text{(ref. 15)} \qquad \text{(XI-25)}$$

The margin of safety is then

$$\text{M.S.} = \frac{1}{\sqrt{\left(\frac{M}{M_{Bcr}}\right)^2 + \left(\frac{M_T}{M_{Tcr}}\right)^2}} - 1 \qquad \text{(XI-26)}$$

A sample calculation for the 1.125-inch diameter tube yields

$$\text{M.S.} = \frac{1}{\sqrt{\left(\frac{0.029}{0.098}\right)^2 + \left(\frac{0.94}{170}\right)^2}} - 1 = 2.4$$

The M.S. for each rod size loaded as a yaw or damper boom is presented in tables XI-1 through XI-4.

Results

The results are contained in tables XI-1 through XI-4.

TABLE XI-1

COMPARISON OF YAW RODS FOR THE SYMMETRICAL CONFIGURATION

	Rod Diameter and Thickness		
	1.125-in. Dia. 0.005 t	0.90-in. Dia. 0.004 t	0.675-in. Dia. 0.003 t
δ_s - Thermal deflection (in.)	75	75	75
δ_{Fn} - Deflection due to F_n* (in.)	25	53	147
δ_T - Maximum total deflection (in.)	100	128	222
M_B - Bending moment, maximum (in.-lb)	0.94	0.82	0.72
M_{Bcr} - Bending moment, critical (in.-lb)	170.4	87.0	36.6
M_T - Torsional moment, maximum (in.-lb)	0.029	0.025	0.022
M_{Tcr} - Torsional moment, critical (in.-lb)	0.098	0.050	0.020
θ_m - Twist angle of tip mass (rev)	5.8	12.7	-
M.S. - Margin of safety	+2.40	+1.0	-
Wt - Weight (200 feet) (lb)	19.2	12.4	7.0

* Value of F_n obtained from previous discussions.

1.12-in. Diameter	0.90-in. Diameter	0.675-in. Diameter
a = 460	a = 370	a = 276
c = 1.55	c = 0.64	c = 0.20
c'= 1.24c = 1.92	c'= 1.18c = 0.0755	c'= 1.13c = 0.226

TABLE XI-2

COMPARISON OF DAMPER RODS FOR
THE SYMMETRICAL CONFIGURATION

	Rod Diameter and Thickness		
	1.125-in. Dia. 0.005 t	0.90-in. Dia. 0.004 t	0.675-in. Dia. 0.003 t
δ_s - Thermal deflection (in.)	75	75	75
δF_n - Deflection due to F_n* (in.)	17	34	88
δ_T - Maximum total deflection (in.)	92	109	163
M_B - Bending moment, maximum (in.-lb)	0.65	0.53	0.43
M_{Bcr} - Bending moment, critical (in.-lb)	170.4	87.0	36.6
M_T - Torsional moment, maximum (in.-lb)	0.020	0.016	0.013
M_{Tcr} - Torsional moment, critical (in.-lb)	0.098	0.050	0.020
θ_m - Twist angle of tip mass (rev)	4.0	8.1	22.1
M.S. - Margin of safety	+3.9	+2.1	+0.5
Wt - Weight (200 feet) (lb)	19.2	12.4	7.0

* Value of F_n obtained from previous discussions.

TABLE XI-3

COMPARISON OF YAW RODS FOR THE ASYMMETRICAL CONFIGURATION

	Rod Diameter and Thickness		
	1.125-in. Dia. 0.005 t	0.90-in. Dia. 0.004 t	0.675-in. Dia. 0.003 t
δ_s - Thermal deflection (in.)	75	75	75
δF_n - Deflection due to F_n* (in.)	18	37	103
δ_T - Maximum total deflection (in.)	93	112	178
M_B - Bending moment, maximum (in.-lb)	0.66	0.58	0.51
M_{Bcr} - Bending moment, critical (in.-lb)	170.4	87.0	36.6
M_T - Torsional moment, maximum (in.-lb)	0.021	0.018	0.016
M_{Tcr} - Torsional moment, critical (in.-lb)	0.098	0.050	0.020
θ_m - Twist angle of tip mass (rev)	4.2	9.1	27.0
M.S. - Margin of safety	+3.7	+1.8	+0.25
Wt - Weight (200 feet) (lb)	19.2	12.4	7.0

* Value of F_n obtained from previous discussions.

TABLE XI-4

COMPARISON OF DAMPER RODS FOR THE ASYMMETRICAL CONFIGURATION

	Rod Diameter and Thickness		
	1.125-in. Dia. 0.005 t	0.90-in. Dia. 0.004 t	0.675-in. Dia. 0.003 t
δ_s - Thermal deflection (in.)	75	75	75
δF_n - Deflection due to F_n* (in.)	12	25	63
δ_T - Maximum total deflection (in.)	87	100	138
M_B - Bending moment, maximum (in. -lb)	0.46	0.39	0.31
M_{Bcr} - Bending moment, critical (in. -lb)	170.4	87.0	36.6
M_T - Torsional moment, maximum (in. lb)	0.014	0.012	0.010
M_{Tcr} - Torsional moment, critical (in. -lb)	0.098	0.050	0.020
θ_m - Twist angle of tip mass (rev)	2.8	6.0	17.2
M.S. - Margin of safety	+6.0	+3.1	+1.0
Wt - Weight (200 feet) (lb)	19.2	12.4	7.0

* Value of F_n obtained from previous discussions.

Conclusions

General - The analysis indicates that the use of unfurlable beryllium copper tubes is entirely feasible from a structural standpoint for the satellite configurations outlined in figure XI-1. Because of the high radius-to-thickness ratio of the tubes and the possibility of local imperfections, a higher margin of safety will be used than is normally required. On this basis, the following recommendations are made in table XI-5. Total weight is defined as the weight of: two 200-ft yaw booms, two 16-lb tip masses, two 200-ft damper booms, and two 8-lb tip masses.

TABLE XI-5

RECOMMENDATIONS

Configuration	Yaw Boom Size	Damper Boom Size	Total Weight
Symmetrical	1.125-in. dia. 0.005-in. thick	0.90-in. dia. 0.004-in. thick	111.2 lb
Asymmetrical	0.90-in. dia. 0.004-in. thick	0.675-in. dia. 0.003-in. thick	86.8 lb

If subsequent test programs prove the accuracy of the analyses presented, the margins of safety could be reduced. By reducing the boom sizes, a system weight saving on the order of 20 to 40 pounds could be achieved. However, care should be exercised in reducing boom size in that greater boom deflections, (tables XI-1 through XI-4) may then become the new limiting design criteria.

Boom Natural Frequencies - To assure that the satellite librations produced by gravity gradient forces would not excite the erectable booms, boom natural frequencies were calculated and shown to be much higher than satellite natural frequencies. The gravity gradient libration frequencies are given below based on satellite inertia ratios of $I_{yaw}/I_{pitch} = 0.2$ to 0.3 and $I_{roll}/I_{pitch} = 0.8$ to 0.9.

The libration frequencies are:

Roll	Pitch	Yaw
$1.8\text{-}20\ \omega_o$	$1.2\text{-}1.5\ \omega_o$	$0.8\text{-}0.5\ \omega_o$

where ω_o for 2000 nautical miles is 6.24×10^{-4} sec^{-1} and the period is 2.80 hours.

Natural frequencies of the various boom sizes are calculated using the following equation which assumes a uniform cantilever boom of mass, m, with a concentrated tip mass, M.

$$\omega_n = \sqrt{K/M + 0.23\ m} \qquad \text{(XI-27)}$$

Table XI-6 lists the boom natural frequencies.

TABLE XI-6

BOOM NATURAL FREQUENCY TABLE

Boom Size (in.)	Tip Wt. (lb)	ω_n (sec^{-1})	ω_n/ω_o	Period (min)	Application
1.125 dia x 0.005 t	16	0.0172	26.8	6.1	sym. yaw boom
0.900 dia x 0.004 t	8	0.0152	24.2	6.9	sym. damper boom
0.900 dia x 0.004 t	16	0.0115	18.4	9.1	asym. yaw boom
0.675 dia x 0.003 t	8	0.0091	14.6	11.5	asym. damper boom

Since boom natural frequencies are high relative to satellite libration frequencies, it is concluded that resonance and amplification will not occur.

List of Symbols

Symbol	Description
A	Experimental constant
b	Width of curved panel
C	Torsional rigidity of rod (warping not prevented)
C'	Torsional rigidity of rod (warping prevented one end only)
C_T	Coefficient of thermal expansion
CM	Center of mass
d	Rod diameter
e	Eccentricity of applied load
E	Modulus of elasticity in tension
ETM	Effective tip mass
F_n	Normal load
F_c	Axial compressive load
F_b	DeHavilland safety factor (bending - 1.3)
F_t	DeHavilland safety factor (torsion - 1.3)
I	Area moment of inertia
K	Thermal conductivity
K_b	DeHavilland experimental constant based on zero torsional stress (0.75)
K_t	DeHavilland experimental constant based on zero bending stress (0.75)
L, l	Rod length
M_B	Bending moment
M_{Bcr}	Critical bending moment
M_t	Thermal bending moment
M_T	Torsional moment
M_{Tcr}	Critical torsional moment
r	Rod radius
R_s	Incident solar radiation

Symbol	Description
t	Rod wall thickness
ΔT	Temperature gradient across rod diameter
α_s	Solar absorptivity
δ	Deflection of rod tip
γ	Overlap factor
υ	Poisson's ratio
θ	Angle of twist
θ_m	Maximum twist angle (due to torsional load)
θ_{cr}	Critical angle of twist
τ_{cr}	Critical shear stress
τ_{max}	Maximum shear stress
σ_{cr}	Critical compressive stress
σ	Stress
ϵ	Strain

References

1. J.N. MacNaughton, "Unfurlable Metal Structures for Spacecraft"; Presented at the Canadian Aeronautics and Space Institute Astronautics Symposium, Montreal, Canada, March 1963.
2. B. Paul, et al, "A Passive Gravitational Attitude Control System for Satellites," Bell Laboratories, May 1963.
3. Study of Thermal Effects on Gravity Gradient Rods, Final Report, General Electric Company, Document No. 63SD851, October 11, 1963.
4. Study of Thermal Effects on Gravity Gradient Rods, Final Report, General Electric Company, Document No. 63SD851, October 11, 1963.
5. S. Timoshenko, "Strength of Materials", Part I, D. Van Nostrand Company, Incorporated, New York, 1955, p. 260.
6. Ibid, p. 259.
7. Data Sheet No. 200, The DeHavilland Aircraft Company of Canada Limited, Special Prod. and Applied Research, Malton, Ontario, Canada.
8. E.F. Bruhn, "Analysis and Design of Airplane Structures," John S. Swift Company, Incorporated, PB 3.1.
9. Ibid, Figure B 3.3, PB 3.2.
10. Data Sheet No. 200, The DeHavilland Aircraft Company of Canada Limited, op. cit.
11. Trimoshenko and Gere, "Theory of Elastic Stability," McGraw-Hill Book Company, New York, 1961, p. 489.
12. R.J. Roark, "Formulas for Stress and Strain," McGraw-Hill Book Company, New York, 1954, p. 176.
13. S. Timoshenko, "Strength of Materials," Part II, D. Van Nostrand Company, New York, 1956, pp 255-265.
14. J.N. MacNaughton, DeHavilland Aircraft, Personal Communication, October 1964.
15. E.F. Bruhn, "Analysis and Design of Airplane Structures," op. cit.

APPENDIX XII

ATTITUDE CONTROL SIMULATION AND ANALYSIS

The following is a record of the important results obtained from the digital computer simulations of attitude motion described in the text. The simulations were made with the aid of a computer program based on equations derived by J. Garber of the Rand Corp. The equations are approximate in that they are based on the assumption that the satellite is made of two rigid bodies. The approximation is acceptable, however, since the satellite structure was designed to have a maximum bending on the order of 1 degree under stress conditions short of tumbling. As described elsewhere, the program was modified to include representations of disturbance torques and a hysteresis damper with mechanical stops. The basic satellite inertial configuration studied was advanced by B. Tinling and V. Merrick of the Ames Research Center. Seven parameters define this configuration. They are the three principal moments of inertia of the main satellite body, the damper rod moment of inertia, the angle between the damper axis and the body principal axis, and the spring and damping constants of the damper. Throughout the present study, the angle between the damper axis and the body major axis was held at 60 degrees. This, together with the condition $I_y - I_x = 2 I_D$, causes the equilibrium position of the damper rod to be 45 degrees from the orbit plane, which is approximately the position for optimum damping. The spring constant was fixed according to the relationship $K_s = 4.5 I_D \omega_o^2$ which is also an approximately optimum condition. A linear damping constant was used only for an initial comparison. For a major part of the study, a hysteresis damper was included in the simulation, and the saturation torque was varied to obtain the best results. The remaining parameters, the four moments of inertia, were

calculated for the different satellite structures which were studied. The values for the significant cases studied are given in table XII-1.

The computer simulation was used to study both the steady state performance and the initial orientation capability of the satellite. Because the initial behavior of the Ames configuration had been established in earlier studies, a large part of the present analysis was of the steady state performance, and the results of this will be given first. After initial orientation, the satellite is supposed to be aligned with the earth center and the orbit plane. The maximum deviation from this alignment is denoted as the vertical and yaw error. The two factors which were found to be significant causes of attitude error are orbit eccentricity and disturbance torques due to radiation pressure. The analysis of these factors is presented in separate appendices, and the appropriate torque functions were used in the simulation of a given satellite. Since the hysteresis damper was new to the simulation, the effect of the damper on satellite performance was one of the first things examined. It was found that the value of the damper saturation torque affected both the steady state error and the rate of damping of initial librations. From a series of steady state simulation runs in which all parameters but the saturation torque were the same, a value of saturation torque was found which resulted in minimum steady state error. This is given approximately by $T_m = 0.25 I_D \omega_o^2$ and corresponds to the damper spring torque at about 3 degrees deflection. Although it was found that larger values of T_m would result in faster damping, the pointing error was the more critical requirement and the damper torque was set accordingly for the remainder of the study.

Near the beginning of the study, an overall comparison was made between the two satellite structures being considered, the symmetrical and unsymmetrical configurations. They were compared on the basis of settling time and steady state error with both linear and hysteresis dampers. This comparison is summarized in table XII-2. The settling time is defined as the time required for the attitude errors to decrease from the given initial conditions to

TABLE XII-1

MOMENTS OF INERTIA OF SATELLITES

No.	Figure	Quadrapod Height (ft)	Launch Weight (lb)	Orbit Weight (lb)	Alterations	10^6 slug-ft^2			
						I_x	I_y	I_z	I_d
1	XII-4	400	1230	1110	120-lb quad 0.5 in. rods	1.031	1.077	0.256	0.0231
2	XII-5	350			infl at top	0.894	0.940	0.180	0.0231
3	XII-4	400	1300	1180	100-lb quad	1.762	1.818	0.293	0.028
4	XII-4	400	1520	1360	96-degree lens	1.848	1.904	0.433	0.028
5	XII-5	400	1310	650	100-lb quad infl jettisoned	0.622	0.672	0.185	0.025
6	XII-4	450			68-lb quad	1.957	2.013	0.288	0.028
7	XII-6	300	1250		45-lb quad	0.835	0.891	0.1793	0.028

TABLE XII-2

COMPARISON OF SYMMETRICAL AND UNSYMMETRICAL CONFIGURATIONS

Structure	Inertias	Damping	Settling Time (orbits)	Vertical Error (degrees)	Yaw Error (degrees)
Symmetrical	No. 1	Linear $K_D = 7.3$ lb-ft-sec	17	3.1	2.2
Symmetrical	No. 1	Hysteresis $T_m = 1.4 \times 10^{-3}$ lb-ft	7	4.1	6.0
Unsymmetrical	No. 2	Linear $K_D = 7.3$ lb-ft-sec	18	15.1	30.0
Unsymmetrical	No. 2	Hysteresis $T_m = 1.4 \times 10^{-3}$	7	19.5	36.0

Note: Initial conditions: 0.2-rad pitch error, others as for steady-state
Orbit conditions: sun in orbit plane, e = 0

the steady state values. It is seen that the hysteresis damper results in slightly larger attitude errors than the linear damper. The indicated superior damping of the hysteresis damper is partly due to the definition of settling time which does not favor the exponential decay of the linearly damped system. When the two satellites are compared, the obvious difference is the pointing error. The errors of the symmetrical configuration would be acceptable, whereas the errors of the unsymmetrical configuration are much too large. The errors could be reduced by increasing the satellite moments of inertia or by reducing the disturbance torques. Since the height of the structure would have to be more than doubled to obtain the required inertia, consideration was given to reducing the disturbance torque. As indicated in another appendix, a large part of the disturbance torque could be canceled by a sphere attached to the top of the quadrapod. This configuration was simulated in a second comparison of the two satellites. In this comparison, which is

summarized in table XII-3, the maximum sunlight induced eccentricity for the two satellites was included in the simulations. The unsymmetrical satellite with the balancing sphere was shown to have a very low error - so low in fact, that it was decided not to improve the approximate disturbance torque formula used in the simulation.

TABLE XII-3

COMPUTED STEADY STATE PERFORMANCE OF SYMMETRICAL AND BALANCED UNSYMMETRICAL CONFIGURATIONS

Structure	Inertias	e	Disturbance Torque	Vertical Error (degrees)	Yaw Error (degrees)
Symmetrical	No. 1	0.035	No	4.3	8.6
Balanced unsymmetrical	No. 2	0.015	No	1.6	3.0
Symmetrical	No. 1	0.000	Yes	3.3	4.7
Balanced unsymmetrical	No. 2	0.000	Yes	1.4	3.1
Symmetrical	No. 1	0.035	Yes	6.3	10.5
Balanced unsymmetrical	No. 2	0.015	Yes	1.6	2.4

Note: Orbit conditions - sun in orbit plane

Due to the large eccentricity, the symmetrical satellite had large errors. Two approaches were taken to compensate for this. One approach was to consider the use of a lens with a larger included angle so that equivalent RF ground coverage would result in spite of the larger vertical error. A comparison made for this case is indicated by the first two entries of table XII-4. These show the pointing errors of two satellites, identical except for 84- and 96-degree included angles, respectively. It is seen that the larger lens increases the vertical error only slightly. The 96-degree lens is an extreme case and would add approximately 200 pounds to the satellite weight. The second approach to compensate for the large errors of the

TABLE XII-4

STEADY STATE ERRORS OF VARIOUS SATELLITE CONFIGURATIONS

Structure	Inertias	e	Vertical Error (degrees)	Yaw Error (degrees)
Symmetrical	3	0.03	3.9	7.5
Symmetrical	4	0.03	4.3	3.5
Symmetrical CM offset	6	0.035	4.0	6.0
Balanced unsymmetrical	5	0.015	2.0	2.5
Symmetrical sail	7	0.01	1.8	6.0

symmetrical satellite was to increase the height of the structure. Errors caused by disturbance torques decrease in proportion to the increase in moments of inertia, while errors due to eccentricity approach a minimum as the ratio between the satellite principal moments of inertia approach that of a slender rod. The pointing errors of a satellite with a 450-foot quadrapod are given in the third listing. For this case, a more realistic disturbance torque function was used which included the effects of a 3-foot shift in the mass center. The two remaining listings in the table are for two different configurations which were studied.

The fourth listing is for an altered version of the unsymmetrical configuration. Rather than place the mass of the inflation equipment at the top of the quadrapod, it appeared that it might be desirable to attach this mass below the lens in order to produce a symmetrical configuration during the erection process. The satellite that would result when the inflation equipment is subsequently jettisoned, would have the errors indicated in the fourth listing. At the close of the present study, a third type of satellite structure was introduced. It consists of a symmetrical configuration with a transparent lens and symmetrically placed solar sails. It was advanced on the supposition that a sail material could be made which would not interfere with the RF characteristics of the lens. As the final listing of table XII-4 indicates, this satellite should have a quite low steady state error.

As a complement to the steady state simulations, an examination was made of the possible attitude behavior of a satellite after it is erected in orbit in order to determine what might be expected during this transient phase and what active control elements would be necessary to assure that the satellite becomes oriented with the proper end facing the earth. As a starting point for the discussion, it is obvious that the satellite will at least begin with large oscillations. This would be caused by attitude errors in the placement of the canister and additional errors resulting from the unfolding of the satellite and by an angular rate error of approximately orbital rate. The rate error due to initial rate would produce an initial oscillation of about 45 degrees in pitch. The dynamic simulation has shown that such large pitch oscillations cause complete rotations in yaw so that the final velocity pointing attitude of the satellite cannot be predetermined. This is not a serious problem because the velocity pointing direction can be determined from ground by observing the direction of orbit position change with a known angle between the lens and yaw stabilization boom. The serious problem is, rather, that the vertical pointing direction might be in doubt. The combination of attitude and rate errors alone could possibly cause the satellite to tumble end over end. In addition, it has not been shown that the impulse due to gas leaving the satellite would not be high enough to cause tumbling.

Since tumbling is a distinct possibility, this was simulated to determine the damping characteristics of the satellite with relatively large initial rate errors. The results of this simulation are indicated in table XII-5, with the results for some less severe initial conditions. The initial orientation performance of the satellites were evaluated in terms of the settling time which was measured as the time required for the attitude errors to reach the steady state values. It is seen that the performance is similar for different configurations and is satisfactory.

TABLE XII-5

INITIAL ORIENTATION PERFORMANCE OF SATELLITES

Structure	Inertias	e	Initial Conditions		Settling Time (orbits)
			a_o	$\dot{a}_o$	
Symmetrical sail	6	0.01	0	ω_o	22
Symmetrical	3	0.035	0	$-\omega_o$	35
Symmetrical	3	0.035	-20°	$-\omega_o$	75
Symmetrical	3	0.035	0	$2\omega_o$	90*

* Tumbled 47 orbits.

It can be said that the satellites would settle reasonably quick to a stable position even from a tumbling condition.

If the resultant position should be incorrect, the inversion technique described later in this appendix could be used.

Simulation of Hysteresis Damper and Damper Stops

Because of the relatively large damping requirements of the satellite being considered, a magnetic hysteresis damper was calculated to have a significant weight and size advantage over an eddy current damper. The linear torque versus angular velocity relationship of the eddy current damper had been used previously in the digital computer simulation of the satellite attitude motion, and it now became necessary to incorporate the nonlinear characteristic of the hysteresis damper. A prototype of such a damper had been built and tested in a company-sponsored study and a typical measured torque versus angle curve is shown in figure XII-1. The hysteresis loops were produced when the damper rotor was rotated between fixed limits. The enclosed area is proportional to the dissipated energy. When the damper rotor is cycled between random limits, the torque locus is a continuous line formed of segments similar to those shown, always enclosing area in clockwise sense for the axes shown. It is a characteristic of the damper that after a continuous rotation greater than a certain amount, the torque reaches a maximum value which has been called the saturation torque. It is also a characteristic that unless the saturation torque is attained, the locus will be confined to loops centered at a fixed angle. Thus, if the rotor were displaced and released, it would return to a position differing from the starting position by slightly more than the angle through which saturation torque was exerted. This rather complicated function was simulated quite closely in the computer program.

Figure XII-2 shows the main features of the simulated torque function. The curved lines are calculated as sections of parabolas. Using logic which is a function of the latest previous angle at which saturation torque was reached, the torque increases along a parabola until, at the apex, the

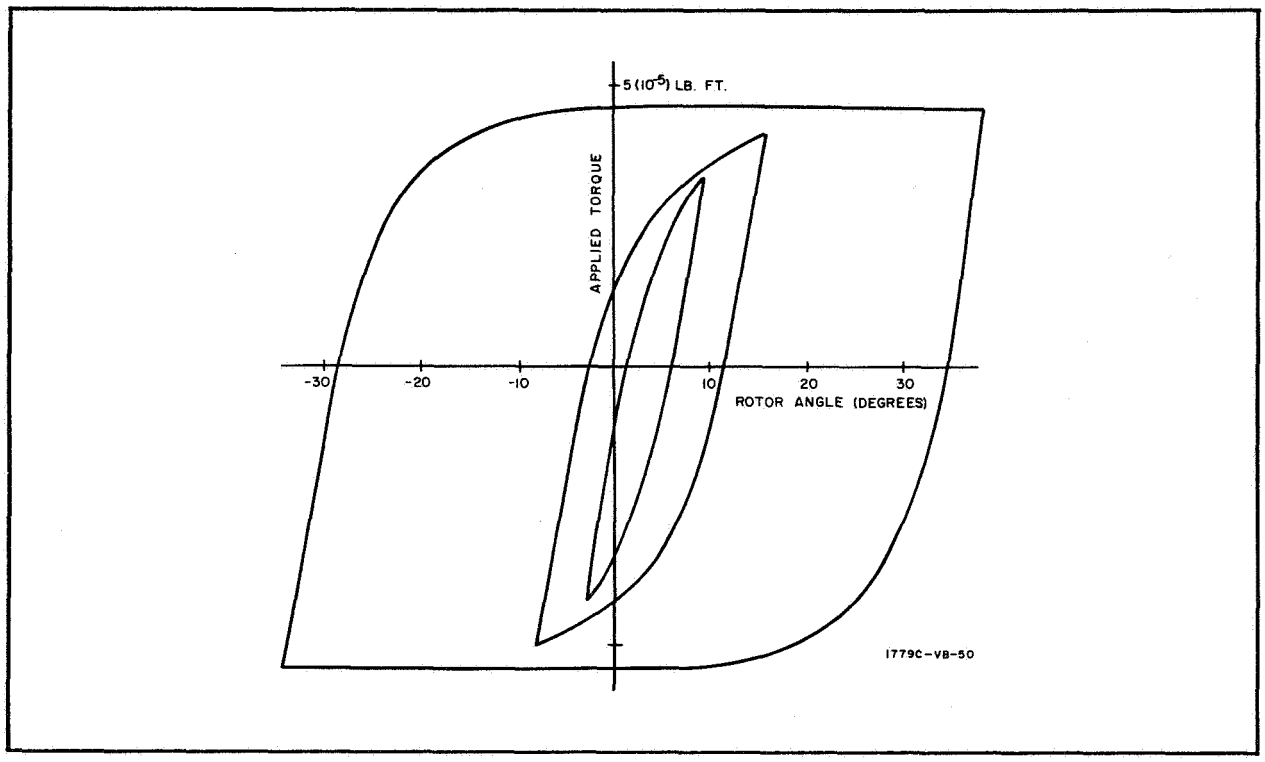

Figure XII-1. Torque vs Angle of Hysteresis Damper, $-5\ (10^{-5})$ lb-ft

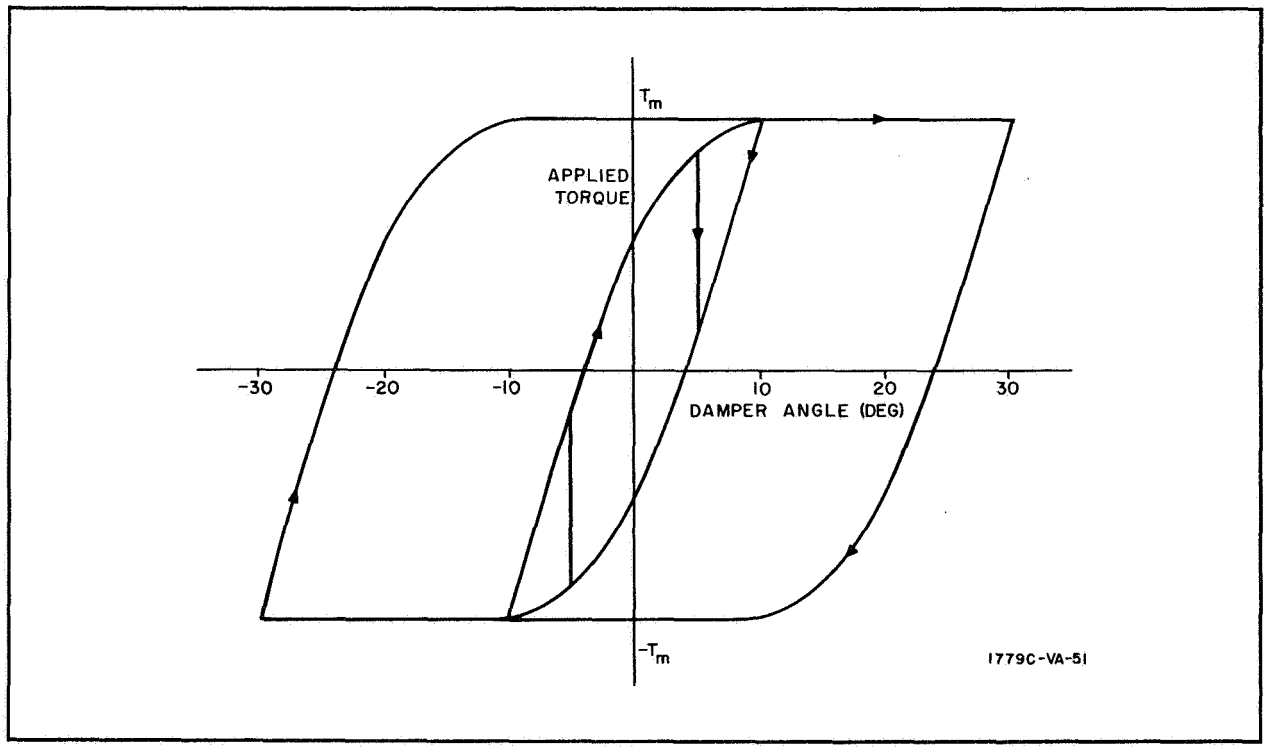

Figure XII-2. Approximation of Hysteresis Damper Characteristic (Arrows Indicate Time Sequence)

saturation torque is reached. If the saturation torque is not reached when the rotation is reversed, the torque function is confined to an inverted parabola which would intersect the previous one at its apex. Thus, the important characteristics of the damper were represented. The magnitude of the saturation torque was left variable, since this has the primary effect on satellite performance and would be adjusted to give the best results.

Mechanical stops would be required in the damper because the damper rod cannot have unrestricted rotation. If the damper should hit a stop during large librations, the rod tip masses and the lens mass could be expected to continue their relative motion until restrained by the elastic deformation of the structure as shown in the exaggerated sketch of figure XII-3.

Therefore, the torque at the damper due to the stop would be the linear torque function of a spring provided, the torque did not exceed the elastic limit. Since the characteristics of the structure specified by the G. A. C. were not known, it was assumed to be a rigid body. This is an excessively severe approximation because the more rigid the coupling between the lens and rod mass, the higher the resulting impact torques would be. In order to evaluate the elastic spring constant, the bending characteristic of the damper rod was used. As shown in figure XII-4, a torque and angle can be defined from a force and deflection so that the spring constant is defined as

$$K_{STOP} = F \frac{F \ell^2}{\delta}$$

For the two rod sizes used for dampers, the constants are as follows:

Satellite	Rod Thickness (mils)	Spring Constant (lb ft/rad)
symmetrical	4	3.0
unsymmetrical	3	1.0

In the simulation, the damper stop torque was defined by the following equations:

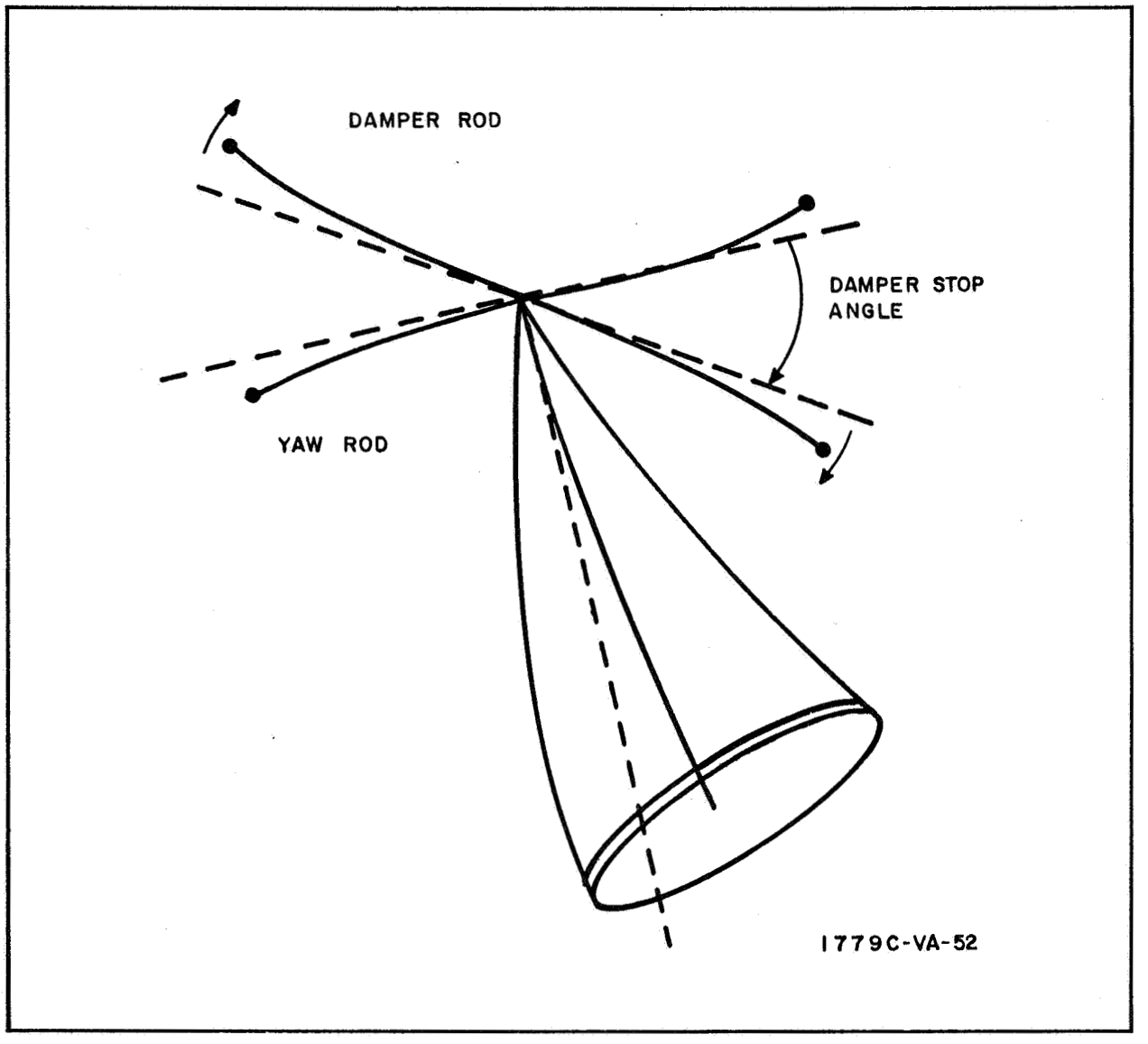

Figure XII-3. Damper Stop Dynamics

$$T_S = K_{STOP}(\sigma - \sigma_{STOP}) \quad , \quad \sigma > \sigma_{STOP}$$

$$T_S = 0 \quad , \quad |\sigma| < \sigma_{STOP}$$

$$T_S = K_{STOP}(\sigma + \sigma_{STOP}) \quad , \quad \sigma < -\sigma_{STOP}$$

where σ is the damper rotation angle. An additional alteration was necessary to produce an accurate simulation because the large accelerations during impact produced errors in the numerical integrations. It was necessary to

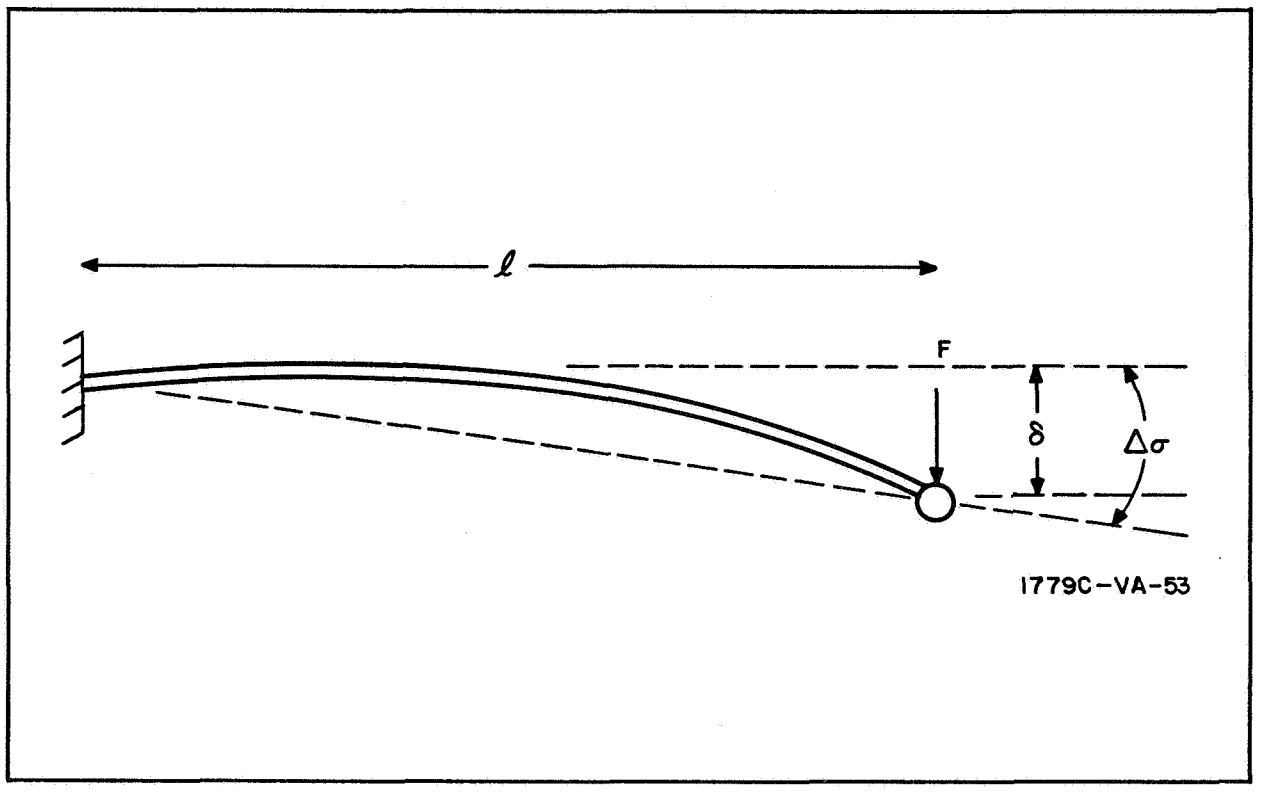

Figure XII-4. Reactions to Determine Elastic Spring Constant of Damper Rod

increase the integration step size during the time the impact torque was exerted so that the integration process was repeated 100 times more frequently than ordinarily. For simulations of high tumbling rates when the damper was held against the stops for long periods of time, the integration frequency could be increased only 10 times without using an exorbitant amount of computer time. The only noticeable effect of this inaccuracy was that the settling times obtained were 5 to 10 percent too short.

With the damper stops simulated, the resulting impact torques were analyzed. A plot taken from one of the computer runs is shown in figure XII-5. The maximum torque was of principal interest because this would determine whether structural damage would result. A series of runs was made for what is believed to be the worst case. The motion of the 400-foot symmetrical configuration with different values of damper stop angle was determined for an initial pitch error of 88 degrees. The maximum impact

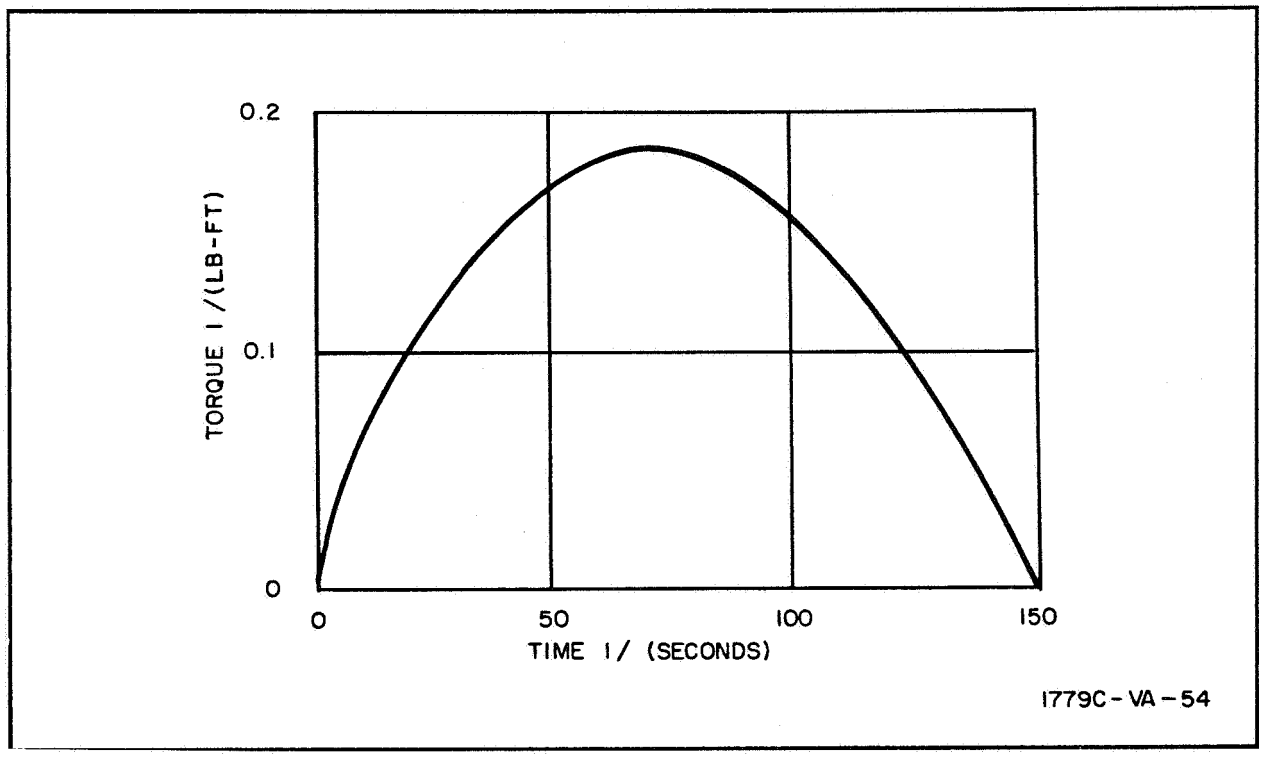

Figure XII-5. Damper Torque Due to Stops

torque as a function of stop angle is plotted in figure XII-6. The torque is at a mimimum when the stops are so far apart that they are not hit. It was decided that 55 degrees was the largest stop angle which could be obtained without complicating the structure, and this was used in the remaining simulations. The 0.25-lb-ft maximum torque is probably higher than would be realized in the actual satellite because of the approximation in the simulation, but this is well within the elastic limits of the dc DeHavilland rods, and is probably not too great a stress for the quadrapod booms.

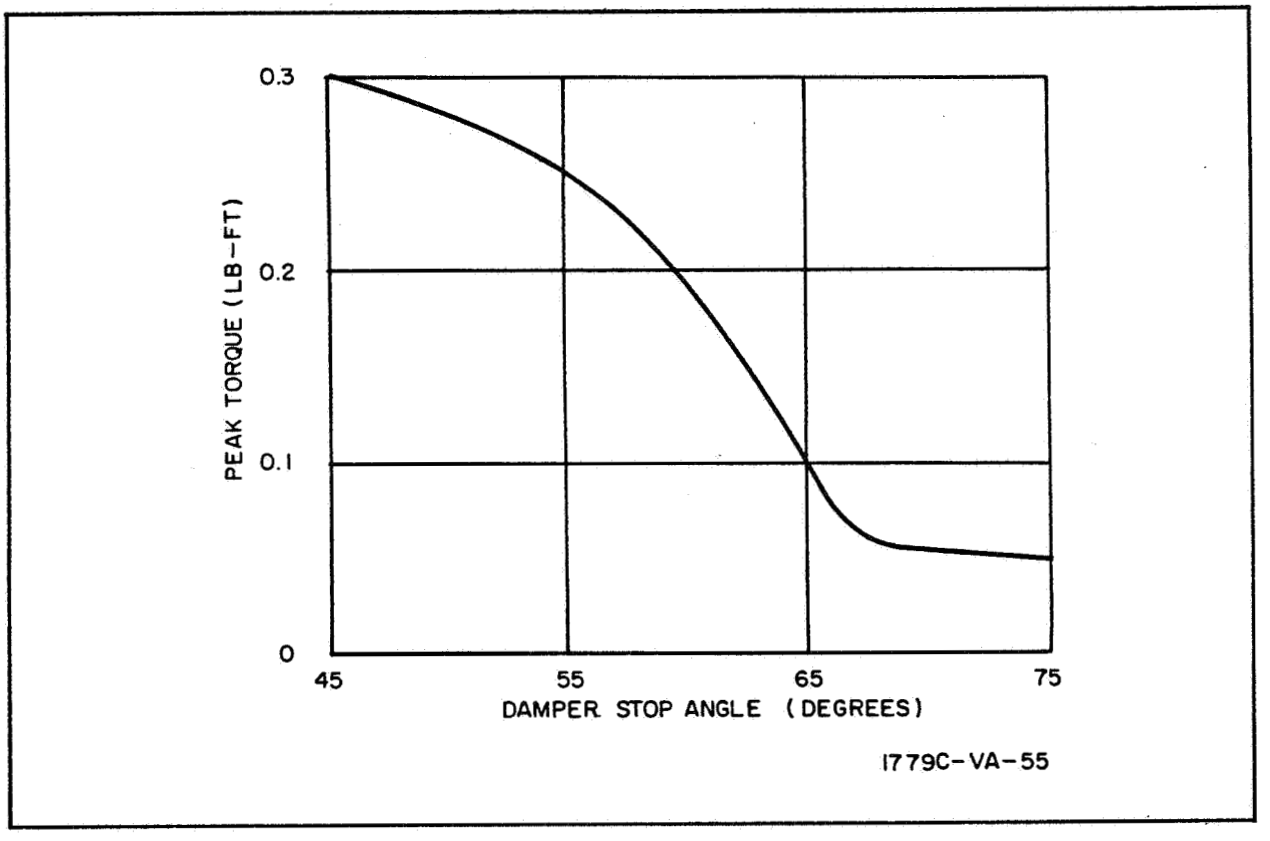

Figure XII-6. Maximum Damper Torque vs Stop Angle

The solar radiation pressure torque for the unsymmetrical configuration was estimated by use of the model of the wire mesh lens. The torque as a function of θ is shown in figure XII-7, and consists primarily of fundamental and third harmonic sine functions of the angle. This was approximated by the fundamental component as follows.

$$T_x = 0.11 \sin\theta \sin\eta \text{ ft-lb}$$

$$T_y = 0.11 \sin\theta \cos\eta$$

$$T_z = 0$$

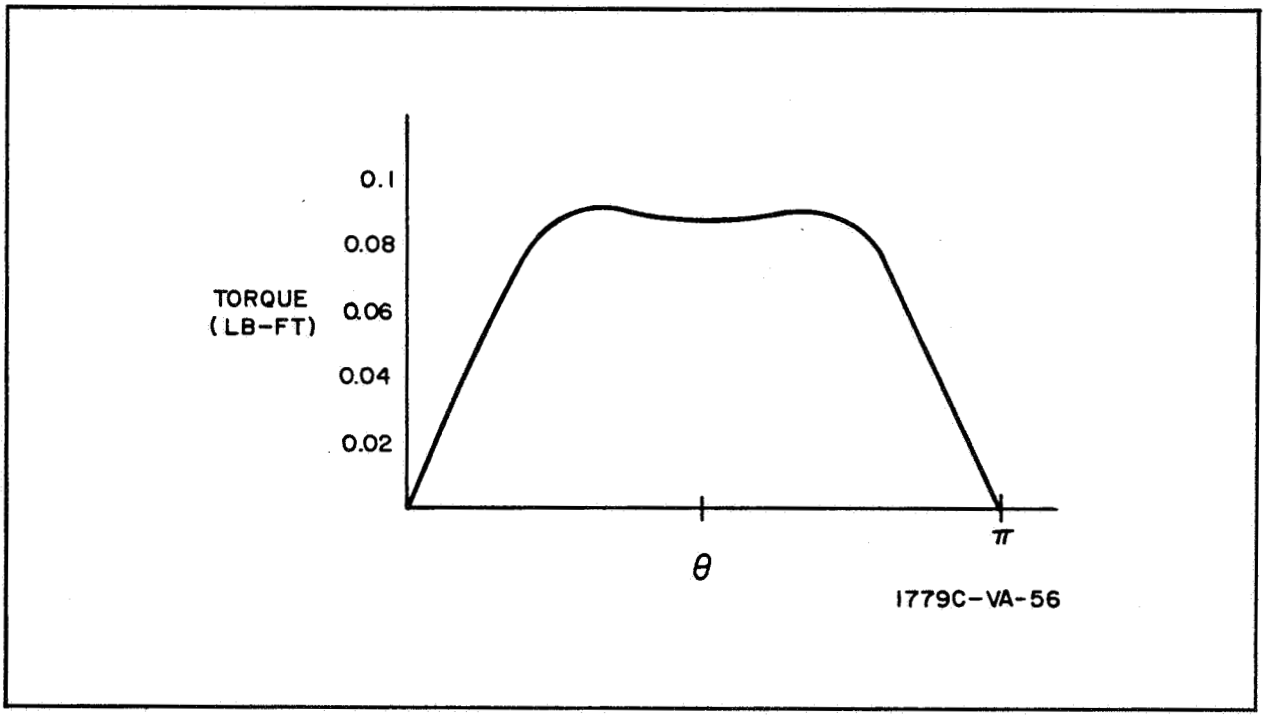

Figure XII-7. Disturbance Torque of Unsymmetrical Satellite

The fundamental component could be balanced by a sphere attached to the apex of the quadrapod, leaving a small third harmonic component. This component was represented in the simulation program with a z-axis torque calculated by assuming a nominal affect of the CM along the x-axis. Thus,

the following disturbance torques were used for the balanced unsymmetrical satellite.

$T_x = 0.02 \sin 3\theta \sin \eta$ ft-lb

$T_y = 0.02 \sin 3\theta \cos \eta$

$T_z = 2.5 (10^{-3}) \sin \theta \sin \eta$

The solar torques due to the transmissive lens when used in a symmetrical configuration would be small enough to be within the range of uncertainty calculating the torque. Accordingly, more significant torques, which would result from imperfections in the satellite, were estimated. The maximum value of these torques are listed below.

Source \ Axis	Torque (lb-ft)	
	x and y	z
20-ft bow in sail	0	$3 (10^{-4})$
1-ft misplacement of sail	$2.5 (10^{-4})$	0
Yaw and damper rods	$2.2 (10^{-3})$	0
1-ft CM displacement	$3.4 (10^{-4})$	$3.4 (10^{-4})$

These were combined to give the following disturbance for the symmetrical sail configuration.

$T_x = 3 (10^{-3}) \sin \theta \sin \eta$ lb-ft

$T_y = 3 (10^{-3}) \sin \theta \cos \eta$

$T_z = 10^{-3} \sin \theta \sin \eta$

In order to provide a model of the solar pressure disturbing torques on the symmetrical satellite for use in the gravity gradient simulation program, the program described in Appendix C of the Phase II final report has been used. In the case of the opaque lens, the program is used to calculate the torques as a function of the position and orientation of the satellite with respect to the sun line; these torques are fit by analytic expressions describing the variation of the torques as a function of position and orientation of the satellite, and the expressions are used directly in the gravity gradient simulation program to calculate the disturbance torques.

The geometry of the coordinate system in which the torques are calculated is shown in figure XII-8. The x-axis lies along a radius vector to the satellite, the y-axis is perpendicular to x in the plane of the orbit, and z is normal in a right-handed sense. The angle θ is the angle between the sun line vector and the radius vector and the angle η represents a counterclockwise rotation of the satellite about the radius vector with the η equal to 0 position being defined as the position where the axis of symmetry of the lens pattern lies along the y-axis. This geometry implies that the satellite is perfectly aligned with the vertical. This is an acceptable approximation because only a small part of the torque is due to earth radiation and the calculation of this part is quite accurate for the important case of small vertical errors during steady state.

The initial coating configuration studied was that used for the lenticular mobility study in the Phase II final report. The configuration and the z-axis torques as a function of θ for η equal to 0 are shown in figure XII-9. For this case, the side having the higher emissivity is aligned along the y-axis at η equal to 0. The curve shown in figure XII-9 can be fit by the following expression:

$$T_z = A \sin 2\theta + B \sin 4\theta + C \cos \theta$$

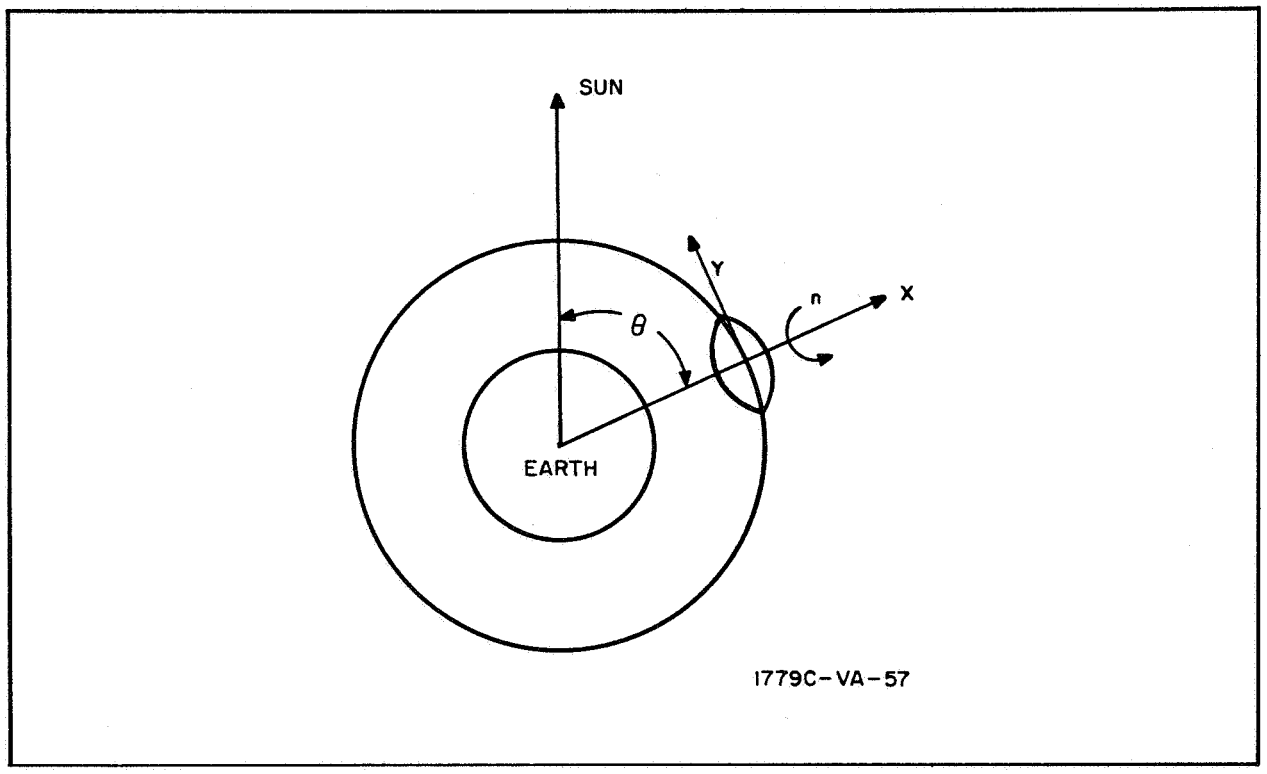

Figure XII-8. Torque Computation Geometry

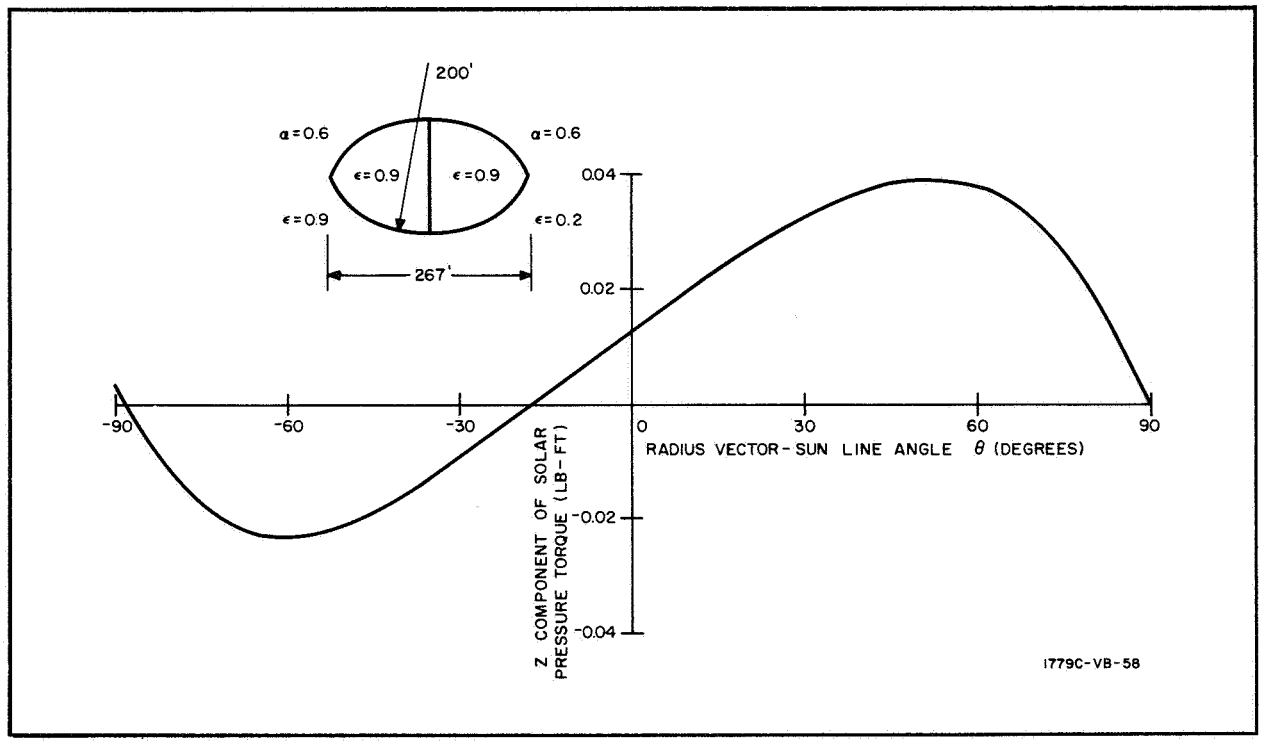

Figure XII-9. Z-Axis Torque for Lenticule

where

$A = 0.03$

$B = 0.005$

$C = 0.013$

Subsequent evaluations of the variation of this torque as a function of the angle η have shown that the C coefficient term varies as a function of the cosine of η. This can be thought of as representing the torque due to the difference in the reradiated solar forces from the surfaces of different emissivity. Similarly, the A coefficient term represents the torques due to the incident solar radiation striking the lenticule at an angle with respect to the vertical axis, and the B coefficient term represents the torques due to earth-emitted and reflected forces. From symmetry, it can be seen that the x-axis torque will be 0 and the y-axis torque will be equivalent to the C coefficient term of the z torque with the exception that will vary as a function of the sine of η. Thus, the torques for this configuration can be summed up as:

$$T_x = 0$$

$$T_y = C \cos \theta \sin \eta$$

$$T_z = A \sin 2\theta + B \sin 4\theta + C \cos \theta \cos \eta$$

When the final coating configuration was chosen (Appendix VI), the torques were reevaluated in the same manner. At the same time, a study was made to determine the effects of a 1-percent difference in the lengths of the booms on the torques. This 1-percent difference is sufficient to cause a shift in the center of gravity of 3 feet in an arbitrary radial direction.

The z-axis torques similar to those shown in figure XII-9 for the center of gravity at the center of the lenticule, the center of gravity shifted 3 feet in either direction along the symmetrical axis, and the center of gravity shifted 3 feet in a vertical direction are shown in figure XII-10. As can be seen; the displacement of the center of gravity into the low emissivity side produces the maximum or worst z-axis torque. The displacement along the

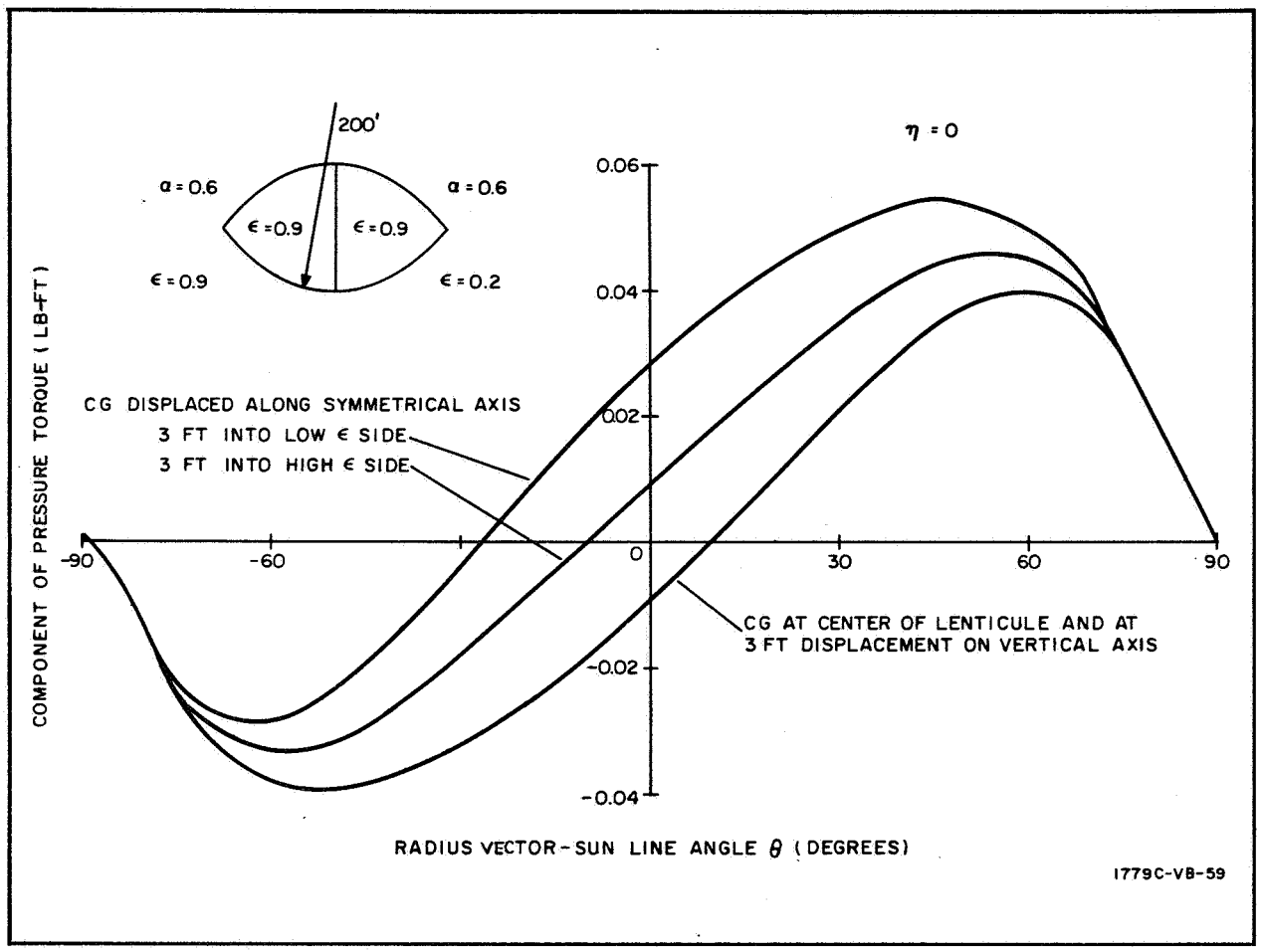

Figure XII-10. Z-Axis Torque for Offset CG Lenticule

vertical axis of course produces no change in the z-axis torque and can be shown to produce smaller magnitude variations on the x- and y-axes than are produced on the z-axis by the former displacement. For this reason, the worst case, that is, a displacement of the center of gravity into the low emissivity side, was chosen for further analysis and use in the gravity gradient simulation program.

The variation of the x, y, and z torques as a function of η are shown in figure XII-11 for this case at a sun line angle of 45 degrees. As can be seen, these variations can be closely approximated by sine, cosine functions. The torques as a function of the position and orientation of the satellite can then be closely approximated by the following expressions:

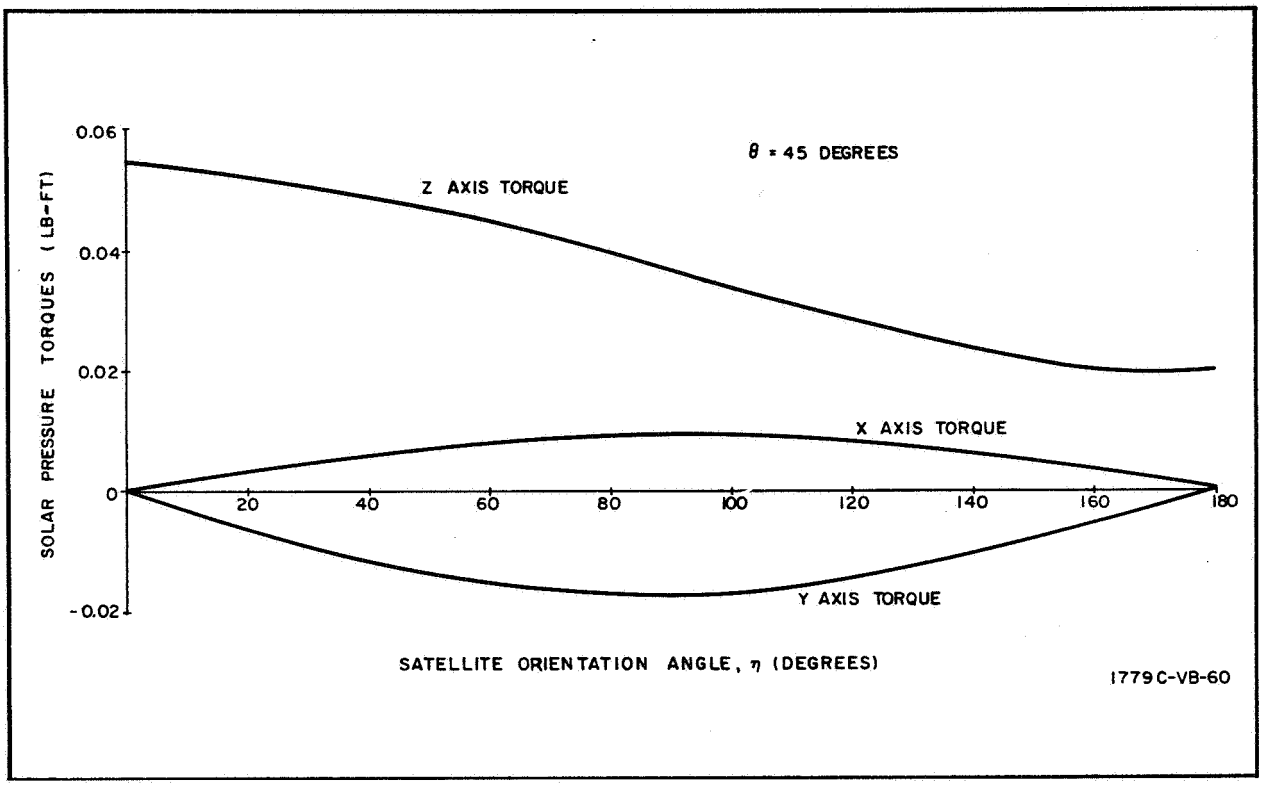

Figure XII-11. Variation of Torques With Satellite Orientation Angle

$$T_x = (C_1 \sin\theta + C_2 \sin 3\theta) \sin\eta$$

$$T_y = (D_1 \cos\theta + D_2 \cos 3\theta) \sin\eta$$

$$T_z = \left[A_0 + \sum_{i=1}^{4} Ai \cos(2i\theta)\right] \cos\eta + \sum_{i=1}^{4} Bi \sin(2i\theta)$$

where

$C_1 = 0.01$ $\quad C_2 = 0.003$

$D_1 = 0.026$ $\quad D_2 = -0.002$

$A_0 = 0.0162$

$A_1 = 0.0122$ $\quad B_1 = 0.0371$

$A_2 = -0.00896$ $\quad B_2 = -0.00602$

$A_3 = 0.000536$ $\quad B_3 = 0.000822$

$A_4 = -0.000259$ $\quad B_4 = 0.000111$

The expression for the z-axis torques represents a Fourier series fit to the calculated data. The x- and y-axis data were considerably easier to fit and the expressions were derived by hand.

The torques as expressed above are transformed into a body centered coordinate system for use in the gravity gradient simulation program. The body axes of the satellite in relation to the orbital axes are shown in figures XII-12 and XII-13. The x- and z-axes are coincident.

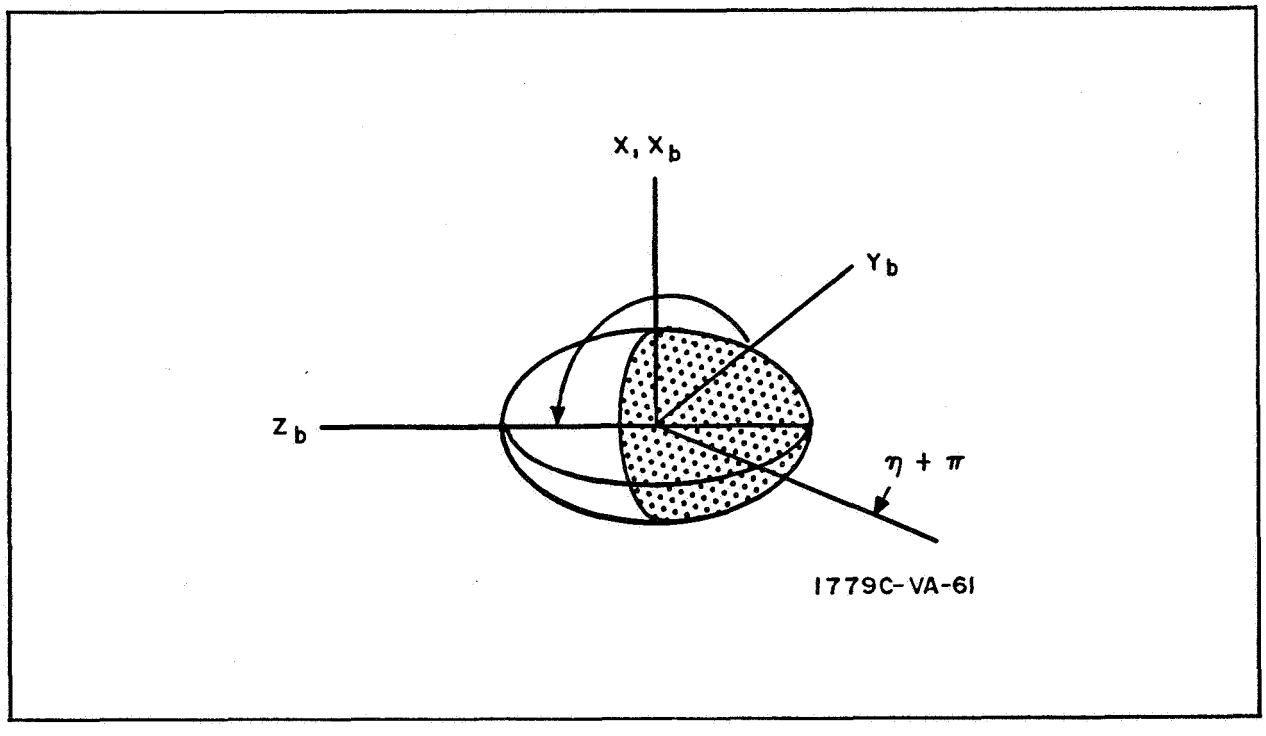

Figure XII-12. Body Axis

The axis of symmetry of the lens pattern could lie anywhere in the x-y plane because of the yaw position controller, but was assumed to be colinear with the x-axis for convenience. With this relationship, the disturbance torques are converted to body coordinates by the following transformation:

$$\begin{pmatrix} T_x \\ T_y \\ T_z \end{pmatrix} = \begin{matrix} 0 & \cos\eta & \sin\eta \\ 0 & -\sin\eta & \cos\eta \\ 1 & 0 & 0 \end{matrix} \begin{pmatrix} T_x \\ T_y \\ T_z \end{pmatrix}$$

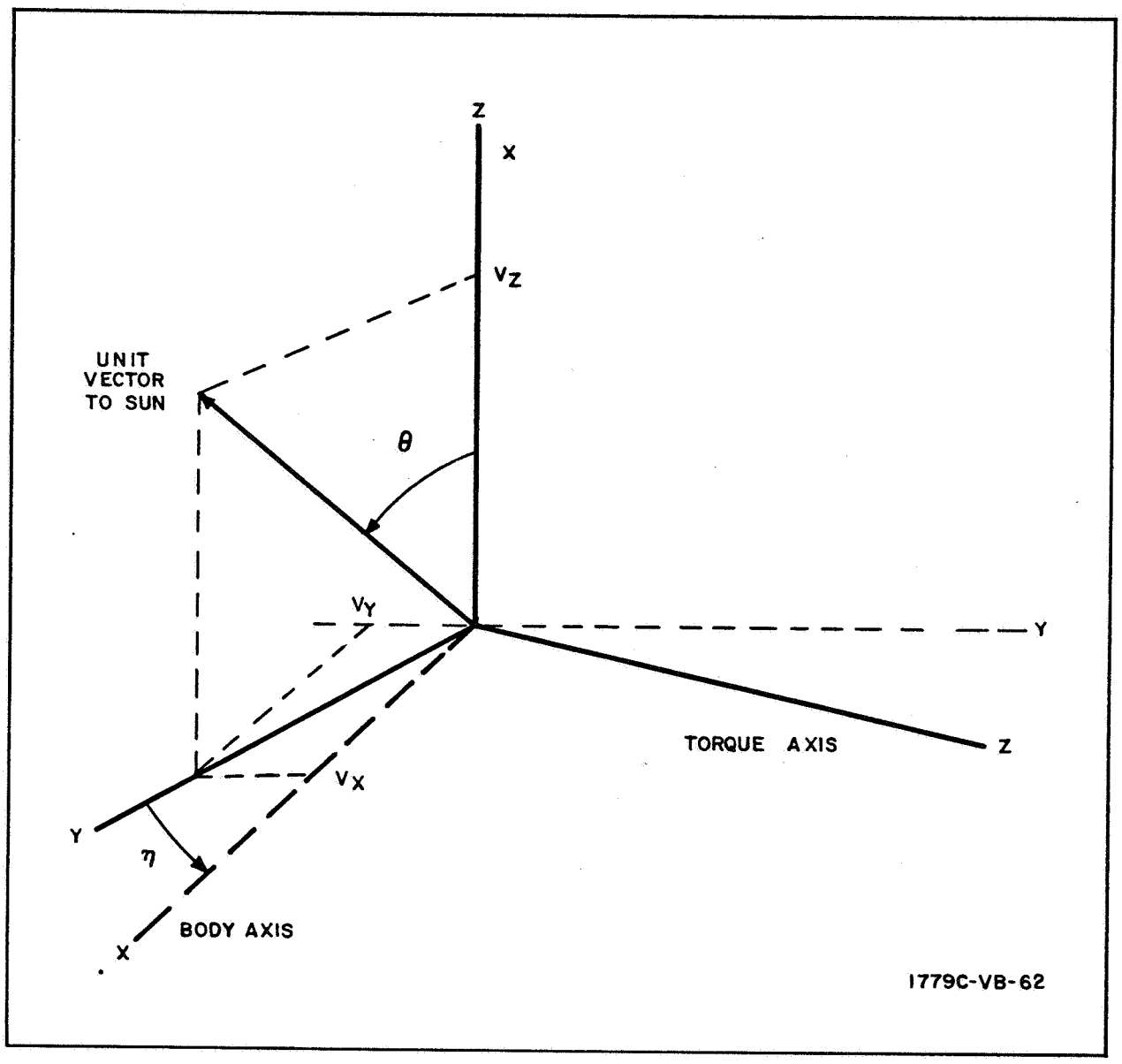

Figure XII-13. Relations Between the Body Axes, the Torque Axes, and the Unit Sun Vector

The two angles required in the torque calculations are obtained in the simulation program as:

$$\theta = \cos^{-1} V_2$$

$$\eta = \tan^{-1} \frac{V_y}{V_x}$$

Not shown here, but included in the program, is the occulation function. In all disturbance torque calculations, the torque was set equal to 0 for the condition of the earth shadowing the satellite.

Phase Plane Analysis - If, during inflation of the satellite, unbalanced torques occur, the satellite may tend to stabilize in an inverted condition. This may require a second controlled inversion to correct the satellite attitude. Such an inversion may be made about the pitch axis, possibly by employing subliming jets to provide torque. By inverting about the pitch axis, cross-coupling about other rotation axes is eliminated.

A simplified analysis may be made by considering the satellite to be a single rigid body and ignoring any damping of the satellite motion. In this case, the equation of motion about the pitch axis is:

$$\ddot{\theta}\, I_p = M(t) - \frac{3}{2}\,\omega_o^{\,2}\,\sin 2\theta\,(I_r - I_y)$$

where

θ is the pitch angle of the satellite from local vertical

I_p, I_r, I_y are the satellite inertias about the pitch, roll, and yaw axes

$M(t)$ is the external applied torque

ω_o is the orbital rate (radians/second)

With $\theta' = 2\theta$, $\tau = \sqrt{\dfrac{3\,\omega_o^{\,2}\,(I_r - I_y)}{I_p}}\; t$,

this equation becomes

$$\frac{d^2\theta'}{d\tau^2} + \sin\theta' - \beta = 0$$

where

$$\beta = \frac{2M}{3\,\omega_o^{\,2}\,(I_r - I_y)}\,,\ M(t) \text{ assumed constant}$$

This equation is equivalent to the system

$$\frac{d\theta'}{d\tau} = z$$

$$\frac{dz}{d\tau} = -\sin\theta' + \beta$$

The phase plane corresponding to this system may be obtained by integration:

$$\frac{dz}{d\theta'} = \frac{\beta - \sin\theta'}{z}$$

$$z\,dz = \beta\,d\theta' - \sin\theta' d\theta'$$

$$z = \pm\sqrt{2\,(\beta\,\theta' + \cos\theta') + k}$$

where k is a constant of integration.

This equation is plotted in figure XII-14 for several values of β, for $k = -2$. This corresponds to a satellite initially vertical with 0 pitch rate. β may be regarded as a normalized torque, with $\beta = 1$ corresponding to the condition in which the applied torque is just equal to the peak gravity gradient torque. Units of τ have been marked along the trajectories, using the approximation

$$\Delta\tau \approx \frac{\Delta\theta'}{z}$$

Only the upper right quadrant has been plotted, for the range $0 \leq \theta' \leq \pi$, which corresponds to the first 90 degrees of satellite rotation. For the remaining 90 degrees of rotation if the torque is reversed in direction but unchanged in magnitude the trajectories will be the mirror images of those plotted about the line $\theta' = \pi$. Thus, at $\theta' = 2\pi$, the trajectories will approach the stable equilibrium point $\theta' = 2\pi$, $\frac{d\theta'}{d\tau} = 0$, which corresponds to a 180-degree satellite inversion.

A measure of the impulse required for inversion is the product $\beta\tau_T$, where τ_T is the total scaled time τ required to reach the point $\theta' = 2$. Figure XII-15 shows this product plotted versus β. The minimum impulse occurs at $\beta = 1$. (Note that this is based on the assumption of a constant torque applied for the first 90 degrees of satellite rotation, with the torque reversed during the second 90 degrees of rotation. Smaller required impulse may result from thrusting at higher levels for shorter portions of the inversion; however, this would result in higher loads on the satellite and slightly more complicated torque control.)

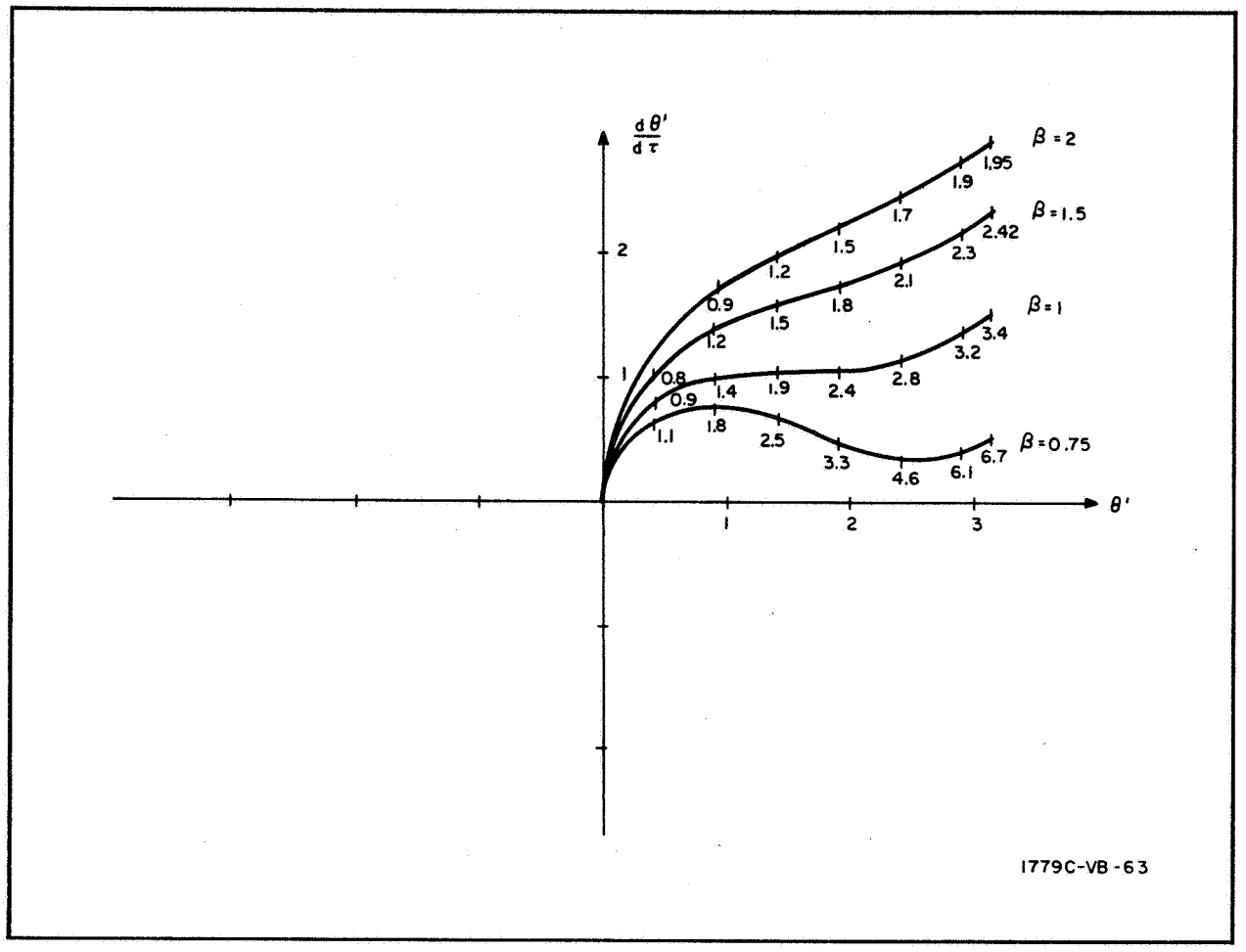

Figure XII-14. Phase Plane Diagram for

$$\frac{d^2\theta'}{d\tau} + \sin\theta' - \beta = 0$$

For $\beta = 1$, the total time required for inversion is given by:

$$T = \frac{\tau}{\frac{T}{\frac{3\omega_o^2 (I_r - I_y)}{I_p}}}$$

while the torque required is

$$M = \frac{3\omega_o^2 (I_r - I_y)}{2}$$

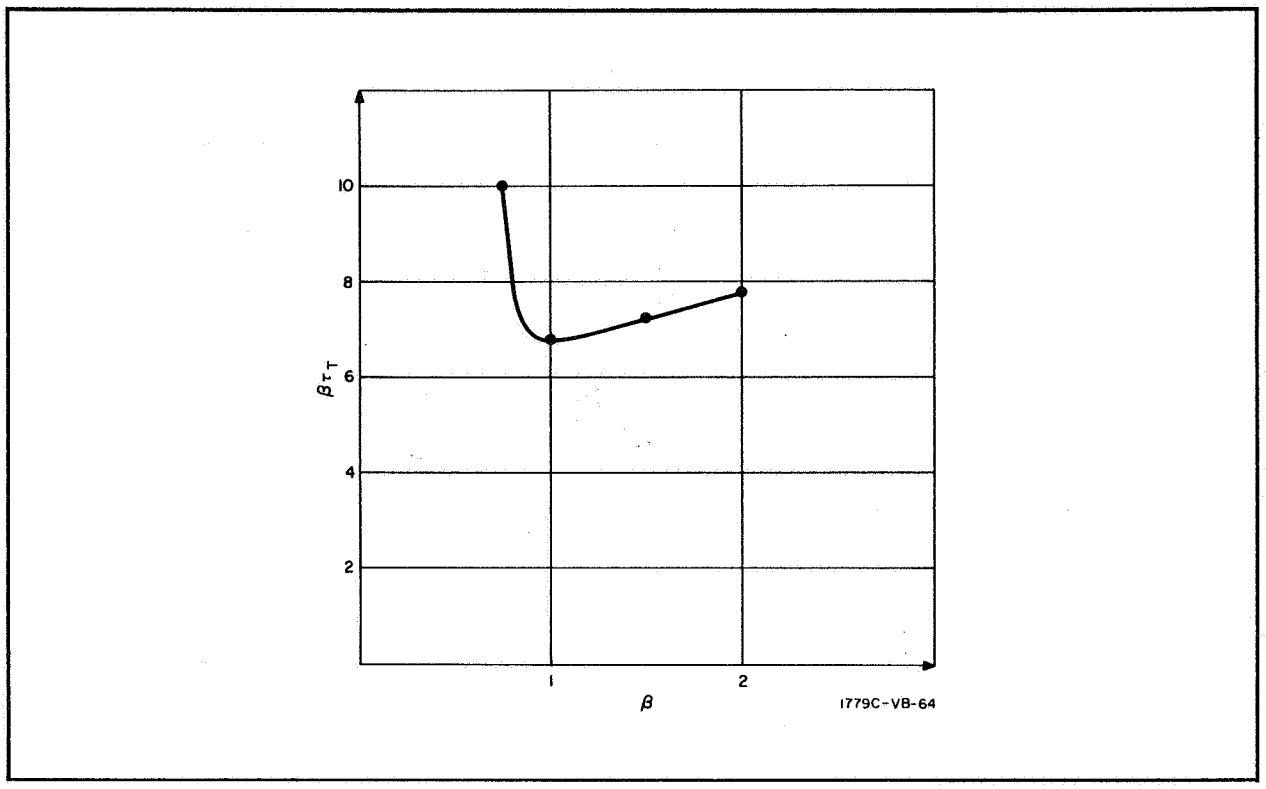

Figure XII-15. Normalized Impulse $\beta\tau_T$ vs β

Assuming values of inertia for the opaque lens satellite of

$I_p = 18.3 \times 10^5$ slug-ft^2

$I_r = 17.8 \times 10^5$

$I_y = 3.2 \times 10^5$

and an altitude of 2000 nmi (corresponding to a period of 2.8 hours), the resulting values of T and M are

$\omega_o = 0.625 \times 10^{-3}$ radians/second

M = 0.853 lb-ft

T = 1.95 hours

= 0.696 orbital periods

Assuming a lever arm of 400 ft, the force is 0.00213 lb, and the total impulse required is:

$$FT = 0.00213\ (1.95 \times 3600)$$

$$= 15 \text{ lb-sec}$$

Tension in Booms - Referring to figure XII-16, torque is assumed applied in the form of forces directed perpendicular to the yaw axis, in the pitch plane of the satellite. These forces will tend to decrease the tension in the supporting booms; in addition, as the satellite rotates toward $\theta = 90$ degrees, the tension in the booms resulting from gravity gradient forces will decrease. To determine the tension in the booms, the various forces on the masses at the end of the booms may be determined as follows. (The total weight of the supporting booms, yaw boom, damper boom, damping mechanism, etc, is treated as though concentrated at the point of M_1, for simplicity.)

x, y, z is taken as a coordinate system centered at the earth's center, rotating at a constant angular velocity $\underline{\omega}_o = \underline{k}\ \omega_o$, where $\underline{i}$, $\underline{j}$, $\underline{k}$ are unit vectors along the x, y, z axes. The orbit is assumed circular and lying in the xy plane. Then, treating M_1, M_2 as particles, the corresponding equations of motion in x, y, z are

$$M\underline{a} = \Sigma \underline{F} + \underline{F}_{\text{centrifugal}} + \underline{F}_{\text{coriolis}}$$

where $\underline{a}$ is the acceleration in x, y, z, $\Sigma \underline{F}$ is the total external force on the particle, and

$$\underline{F}_{\text{centrifugal}} = M\omega_o^2\ \underline{r}_p$$

$$\approx M\omega_o^2\ y\underline{j}$$

$$\underline{F}_{\text{coriolis}} = -2M\underline{\omega}_o \times \underline{v}$$

$\underline{r}_p$ is a vector perpendicular to the z-axis, directed toward the particle.

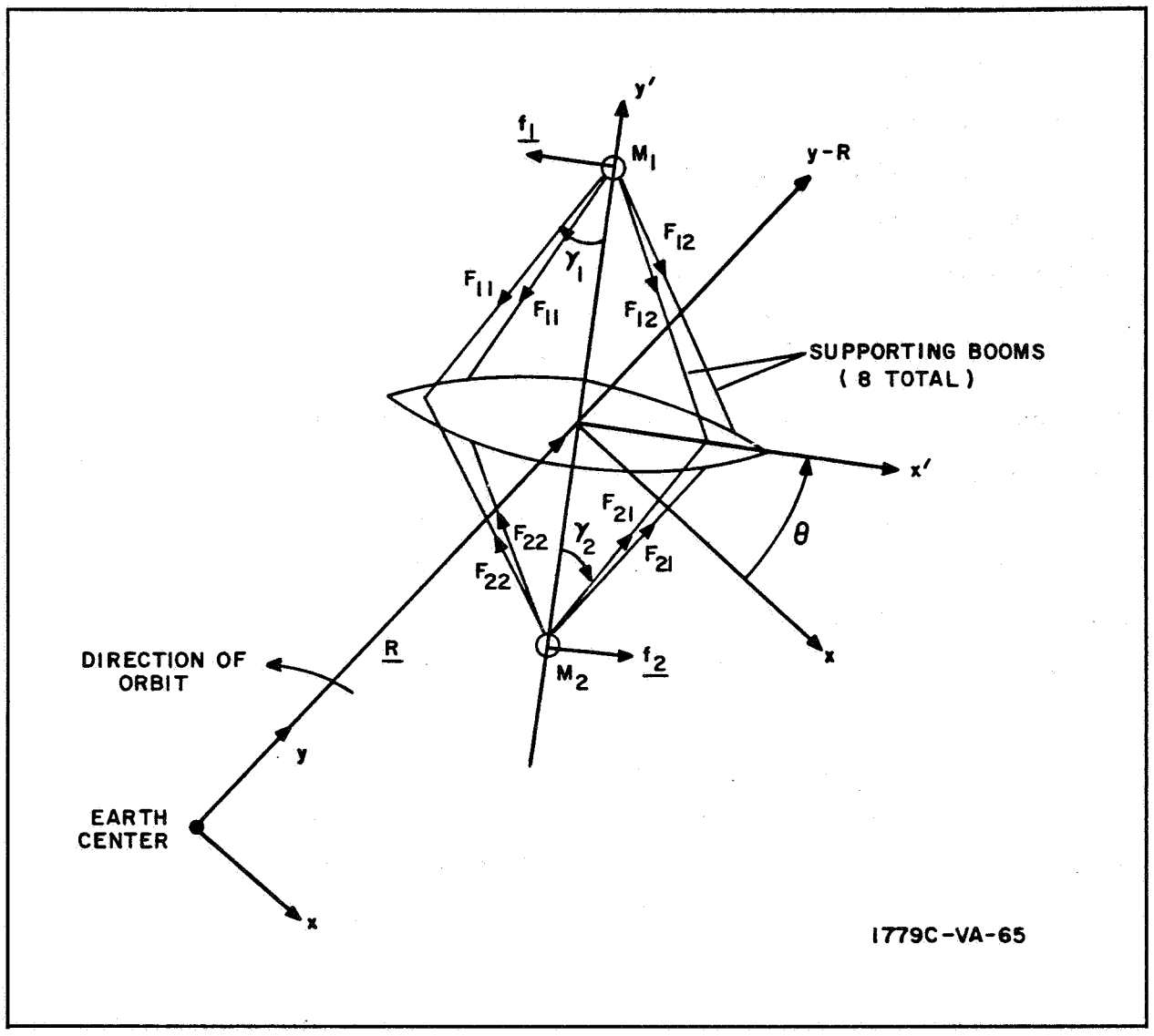

Figure XII-16. Tension Forces in Supporting Booms During Inversion

If the body rotates in pitch (about an axis parallel to the z-axis), then $\underline{v}$ (the velocity of the particle in x, y, z coordinates) is given by $\underline{\omega} \times \underline{r}$, where $\underline{\omega}$ is the angular velocity of the satellite in x, y, z, and $\underline{r}$ is a vector from the rotation axis to the particle. Thus,

$$\underline{v} = \underline{\omega} \times \underline{r}$$
$$= -\underline{i}' \, \theta \, y'$$

and the coriolis forces on M_1 and M_2, respectively, are

$$\underline{j}' \, 2M_1 \, \omega_o \, \dot{\theta} \, y'_1 \; ; \quad \underline{j}' \, 2M_2 \, \omega_o \, \dot{\theta} \, y'_2$$

where

i', $\underline{j}'$, $\underline{k}'$ are unit vectors along x', y', z',

$\dot{\theta} = \omega$ is the satellite pitch rate

y'_1, y'_2 are the y' coordinates of the masses M_1, M_2

(x', y', z' is a body-fixed coordinate system, centered on the rotation axis, as illustrated.)

The centrifugal forces on M_1, M_2 are

$$\underline{j} \; M_1 \, \omega_o^{\,2} \; (R + y'_1 \cos \theta); \; \underline{j} \; M_2 \, \omega_o^{\,2} \; (R + y'_2 \cos \theta)$$

The gravitational forces are approximately

$$-\underline{j} \; M_1 \; \omega_o^{\,2} \; (R - 2y'_1 \cos \theta); \; -\underline{j} \, M_2 \, \omega_o^{\,2} \, (R - 2y'_2 \cos \theta)$$

Resolving these forces into x' y' z' axes,

$$M_1 \underline{a_1} = \underline{F_1} + \underline{i}' \; (M_1 \, \omega_o^{\,2} \, \tfrac{3}{2} \, y'_1 \sin 2\theta)$$

$$+ \underline{j}' \; (2M_1 \, \omega_o \, \dot{\theta} y'_1 + M_1 \, \omega_o^{\,2} \, 3y'_1 \cos^2 \theta)$$

$$M_2 \underline{a_2} = \underline{F_2} + \underline{i}' \; (M_2 \, \omega_o^{\,2} \, \tfrac{3}{2} \; y'_2 \sin 2\theta)$$

$$+ \underline{j}' \; (2M_2 \, \omega_o \, \dot{\theta} y_2' + M_2 \, \omega_o^{\,2} \, 3y'_2 \cos^2 \theta)$$

where $\underline{F_1}$, $\underline{F_2}$ are given by

$$\underline{F_1} = \underline{i}' \; (-f_1 - 2F_{11} \sin \gamma_1 \cos 45° + 2 \, F_{12} \sin \gamma_1 \cos 45°)$$

$$+ \underline{j}' \; (-2 \, F_{11} \cos \gamma_1 - 2 \, F_{12} \cos \gamma_1)$$

$$= -\underline{i}' \left[f_1 + \sqrt{2} \sin \gamma_1 \, (F_{11} - F_{12}) \right] - \underline{j}' \; 2 \cos \gamma_1 \, (F_{11} + F_{12})$$

$$\underline{F_2} = \underline{i}' \left[f_2 + \sqrt{2} \sin \gamma_2 \, (F_{21} - F_{22}) \right] + \underline{j}' \; 2 \cos \gamma_2 \, (F_{21} + F_{22})$$

(The supporting booms have been assumed spaced at 90-degree intervals, on the diagonals of the x' z' plane.)

The particle accelerations are

$$\underline{a}_1 = -\underline{j}' \dot{\theta}^2 y'_1 - \underline{i}' \ddot{\theta} y'_1 \; ; \; \underline{a}_2 = -\underline{j}' \dot{\theta}^2 y'_2 - \underline{i}' \ddot{\theta} y'_2$$

equating $\underline{i}'$ and $\underline{j}'$ components, we obtain for M_1

$$\begin{cases} -\left[f_1 + \sqrt{2} \sin \gamma_1 (F_{11} - F_{12})\right] + M_1 \omega_o^2 \frac{3}{2} y'_1 \sin 2\theta + M_1 \ddot{\theta} y'_1 = 0 \\ -M_1 \dot{\theta}^2 y'_1 = -2 \cos \gamma_1 (F_{11} + F_{12}) + 2M_1 \omega_o \dot{\theta} y'_1 + M_1 \omega_o^2 3y'_1 \cos^2 \theta \end{cases}$$

Solving for $(F_{11} - F_{12})$ and $(F_{11} + F_{12})$

$$\begin{cases} (F_{11} - F_{12}) = (\sqrt{2} \sin \gamma_1)^{-1} (\frac{3}{2} M_1 \omega_o^2 y'_1 \sin 2\theta - f_1 + M_1 y'_1 \ddot{\theta}) \\ \qquad\qquad = C_{11} \\ (F_{11} + F_{12}) = (2 \cos \gamma_1)^{-1} (2M_1 \omega_o \dot{\theta} y'_1 + 3M_1 \omega_o^2 y'_1 \cos^2 \theta + M_1 \dot{\theta}^2 y'_1 \\ \qquad\qquad = C_{12} \end{cases}$$

These yield

$$F_{11} = \frac{C_{11} + C_{12}}{2}$$

$$F_{12} = \frac{C_{12} - C_{11}}{2}$$

Similarly, for M_2,

$$C_{21} = -(\sqrt{2}\sin\gamma_2)^{-1}\left(\frac{3}{2}M_2\,\omega_o^2\,y_2'\sin 2\theta + f_2 + M_2\,\ddot{\theta}\,y_2'\right)$$

$$C_{22} = -(2\cos\gamma_2)^{-1}\left(2M_2\,\omega_o\,\dot{\theta}\,\gamma_2' + 3M_2\,\omega_o^2\,\gamma_2'\cos^2\theta + M_2\,\dot{\theta}^2\,\gamma_2'\right)$$

$$F_{21} = \frac{C_{21} + C_{22}}{2}$$

$$F_{22} = \frac{C_{22} - C_{21}}{2}$$

The gravity gradient tension is smallest at $\theta = \frac{\pi}{2}$. Calculating the total tension at this point,

$\cos\theta = 0$, $\sin 2\theta = 0$, $\dot{\theta} = 0.735 \times 10^{-3}$, $\ddot{\theta} = 0.467 \times 10^{-6}$

$$C_{11} = \left(-\frac{f_1 + M_1\,y_1''\,\ddot{\theta}}{\sqrt{2}\sin\gamma_1}\right), \quad C_{12} = \frac{M_1\,y_1'\,(\dot{\theta}^2 + \omega_o\,\dot{\theta})}{2\cos\gamma_1}$$

$$C_{21} = \left(-\frac{f_2 + M_2\,y_2'\,\ddot{\theta}}{\sqrt{2}\sin\gamma_2}\right), \quad C_{22} = -\frac{M_2\,y_2'\,(2\omega_o\,\dot{\theta} + \dot{\theta}^2)}{2\cos\gamma_2}$$

Assuming $y_1' = 400$ feet, $y_2' = -307$ feet, then

$\gamma_1 = 18.5°$, $\gamma_2 = 25.8°$

for a lens diameter of 267 ft. Then if the torque is provided by thrust jets as M_1, $f_2 = 0$ and

$$f_1 = \frac{0.853\ \text{lb/ft}}{400\ \text{ft}}$$

$$= 2.13 \times 10^{-3}\ \text{lb}$$

$M_1 = 4.56$ slug

$M_2 = 8.39$ slug

$C_{11} = -0.00285$ $\qquad$ $C_{12} = 0.001414$

$C_{21} = 0.001952$ $\qquad$ $C_{22} = 0.00207$

F_{11} = -0.00071 lb; F_{12} = 0.00213 lb

F_{21} = 0.00402 lb; F_{22} = 0.00002 lb

(Note: These results are only approximate, since for an unbalanced torquing force, the satellite orbit is slightly perturbed and the assumption of a circular orbit is not quite correct. However, for M, much less than the total satellite mass, the error will be small.)

These figures indicate that, to avoid compression in the booms, an additional thrust along the y-axis should be applied, sufficient in magnitude to make F_{11} positive. The magnitude of this additional force would be given approximately by

$$\frac{f'}{4} \cos \gamma' > 0.00071 \text{ lb}$$

$$f' > 0.003 \text{ lb}$$

The total thrust required would then be approximately

$$\underline{F_T} = -\underline{i}'(0.00213) + \underline{j}'(0.003)$$

which would be equivalent to a thrust magnitude of 0.0037 lb, at an angle of 35.4 degrees from the y' axis.

Alternatively, torque could be provided by equal, oppositely directed thrusts at M_1 and M_2.

Then $f_1 = f_2 = 0.00121$ lb and

C_{11} = -0.000785 C_{12} = 0.001414

$C_{21} \simeq 0$ C_{22} = 0.00207

F_{11} = 0.000315 lb F_{12} = 0.0011 lb

$F_{21} = F_{22}$

= 0.00103 lb

In this case, no additional thrust along y' is required.